Entanglement Dynamics and Exotic Phases of Matter

NISQ Era Simulations

Jovan Dragoljub Jovanović

Merton College

Rudolf Peierls Centre for Theoretical Physics
University of Oxford

A thesis submitted for the degree of
Doctor of Philosophy

Trinity Term 2024

Abstract

Quantum many-body physics is often outside the scope of what we can model using classical computers. Using variational algorithms, one can sometimes sidestep this issue; however, the choice of the variational space always presumes certain phenomenology, e.g. matrix product states cannot efficiently model certain long-range correlations, etc. This is the reason why, in our search towards new physics, we should consider programmable quantum devices in the study of complex quantum systems. Coupled with the promised real-world application of quantum computers, this has led to a series of rapid technological developments in this field in recent years. In this thesis, I explore the capabilities of (current) noisy intermediate-scale quantum (NISQ) simulators applied to problems in many-body quantum physics. To that end, I provide three studies: one that deals with scrambling and transport of quantum information in dynamical quantum systems, providing a method for time-evolution channel tomography; one that presents a practical experimental proposal to probe non-Abelian anyon physics, with concrete circuits compiled and optimised; and, lastly, one that explores a phase diagram of steady states of a certain monitored circuit based on the toric code and its resilience to errors. In order to demonstrate the practicality of our proposals, in the first two studies, we have run our proposed experiments either on actual quantum devices or on noisy classical simulators, achieving acceptable signal-to-noise ratios. I comment on the connecting thread between the three studies, establishing non-local correlations and engagement in NISQ devices; and offer near term extensions to all three avenues of research.

Entanglement Dynamics and Exotic Phases of Matter

NISQ Era Simulations

Jovan Dragoljub Jovanović

Merton College

Rudolf Peierls Centre for Theoretical Physics

University of Oxford

A thesis submitted for the degree of

Doctor of Philosophy

Trinity Term 2024

To my brother,
who has been tirelessly caring for
our family in these difficult times:
I would not be able to focus
on finishing this work without you.

Acknowledgements

Institutional

I would like to thank my funding bodies: Merton College Charitable Corporation, the family of the late John J Kirby[1] and Oxford-ShanghaiTech collaboration agreement.

Personal

> No one has yet drunk a cup of honey without mixing it with a cup of gall, a cup of gall needs a cup of honey, they are swallowed the easiest when mixed. (*The Mountain Wreath* — Petar II Petrović-Njegoš)

This piece of work ties up what has been a truly amazing chapter of my life. The bitterness that came with the sweetness of finishing this degree and moving on to a new and exciting stage was the news that I received on 21stof March; those being about my dear mother's illness. I pray she has many good days ahead, enough for me to explain my thesis to her a hundred times over.

I would not have been able to focus on finishing this work without knowing that my brother and father (with other family members and friends) are taking great care of her. I have been on the receiving end of my family's support countless times before, and for that I am beyond grateful.

> I thank my dear brother Luka; Your inspiring brotherly love and care is the wind in my sail. I thank my wonderful parents, Vesna and Dragoljub; I have only ever known selflessness from you two, I am grateful for every day that I have the opportunity to show how much that means to me.

I came to Oxford during COVID lockdowns and remote working. It was not an easy time for taking a new student on board. I thank my supervisor, Steve Simon, for his guidance and tutelage; We have navigated this degree well. His instinct for when to allow me to wonder and when to ground me down is what made these four years of my professional life the most conducive to my development than any prior period, a mark of a great mentor.

I restate that the beginning was very rough and that I would not have made the best of my first couple of years without the help of my first collaborators, Max

[1]The lawyer who defended Nintendo from Warner Brothers and in whose honour Nintendo named one of their character after.

McGinley and Sam Garratt; You are not aware of the lockdown induced hole you have pulled me out of. Of course, as time went on, I have had the pleasure of working with a lot more fantastic people: Sebastian Leontica, Carolin Wille, Daan Timers, Benedikt Placke, and Sid Parameswaran.

While we are metaphorically in the department, I also extend my gratitude to my phenomenal colleagues and friend: Minghao, Jacob, Jonathan, Domagoj, Luisa, Riccardo, Thomas, Giulio, Saraswat, James, Ioannis, Fabian, Paul, Alex, (CMT) John, (HEP) John, Abhi, Sounak, Nick, Greg, Yves, Matt, David, Nivedita, Michelle, Russell, and many more.

Another reason why there was never a dull moment, not even in COVID, is the amazing support offered by the community and staff at Merton College. The meals in the hall during the first year were some of the very few opportunities I had to socialise. There I have met a great bunch of characters: Samuel, Pavle, Cesare, Hiroto, Kabir, Vikram, Jay, and more; our lockdown group, our trip to Cotswolds will be a story retold many times.

Of course, over the years Mertonians came and went, each leaving a dear mark on my time here: Taisiia, James, Gabriel, Chris and Heloise, Maggie, Zoé, Zoey, Rene, Jaime, Dmitri, Aryaman, Ulziel, Jeremy and Georgie, Buzz, Leonard, Pablo, Alma, Petra, James and Elena, Elizabeth, Leonidas, George, Philippos, Marcell, Mathis, Gabrielle, Alexandra, Tess, Vijay, Richard, Hadleigh, Naga and Nelima, Monica, Anna, David, Charles, Francesca, Diana, Alexander, and many more. Not to skip out on my students: Nikolai, Aggie, Theo, Param, Megan, and many more.

From time to time it is nice to talk in your mother's tongue; the parties, brunches, and road trips with the exYu community I will fondly remember. Thank you: Milan and Sofija, Lav and Anja, Jovana and Igor, Ognjen, Marko, Irma, Katarina, Milena, Đorđe, Kristijan, Eva, Olja, Sara, Matija and Maša, Oliver, Aleksa, Stefan, and more.

Also, to the people outside these categories: Martin, Jiři, Andrei, Gevorg, Chris, Lazar, Ivan, Luka and Sandy, Luka and Maja, Anđela, Dimitrije, Vasilije, Marijana, Aleksandra, Hana, Jovana and Jovana, Saša, Dušan, Charlotte, Vicky, Lara, Olivia, and more.

Lastly; Thank You, to all the mentors who led me along this path: Slaviša, Romana, Đorđe, Ljubica, Stefan, Zoran, Claudio, Malte, David, Vladan, Ronald, and more.

In loving memory of: Vida, my dear grandmother, and Mihajlo, my kind friend and brilliant colleague.

Abstract

Quantum many-body physics is often outside the scope of what we can model using classical computers. Using variational algorithms, one can sometimes sidestep this issue; however, the choice of the variational space always presumes certain phenomenology, e.g. matrix product states cannot efficiently model certain long-range correlations, etc. This is the reason why, in our search towards new physics, we should consider programmable quantum devices in the study of complex quantum systems. Coupled with the promised real-world application of quantum computers, this has led to a series of rapid technological developments in this field in recent years. In this thesis, I explore the capabilities of (current) noisy intermediate-scale quantum (NISQ) simulators applied to problems in many-body quantum physics. To that end, I provide three studies: one that deals with scrambling and transport of quantum information in dynamical quantum systems, providing a method for time-evolution channel tomography; one that presents a practical experimental proposal to probe non-Abelian anyon physics, with concrete circuits compiled and optimised; and, lastly, one that explores a phase diagram of steady states of a certain monitored circuit based on the toric code and its resilience to errors. In order to demonstrate the practicality of our proposals, in the first two studies, we have run our proposed experiments either on actual quantum devices or on noisy classical simulators, achieving acceptable signal-to-noise ratios. I comment on the connecting thread between the three studies, establishing non-local correlations and engagement in NISQ devices; and offer near term extensions to all three avenues of research.

Statement of Authorship

Chapters 2-4 of the thesis are based on the following works[1–3]:

[1] McGinley, M., Leontica, S., Garratt, S.J., Jovanovic, J. and Simon, S.H., 2022. *Quantifying information scrambling via classical shadow tomography on programmable quantum simulators.* Physical Review A, 106(1), p.012441.

[2] Jovanović, J., Wille, C., Timmers, D., and Simon, S. H., 2024. *A proposal to demonstrate non-abelian anyons on a NISQ device.* Quantum, 8, 1408.

[3] Jovanović, J., Placke, B., Parameswaran, S. and Simon, S.H., 2024. *Fermionic String-Glass Order in a Monitored Toric Code.* To Be Submitted.

The thesis also contains my unpublished original material; see public Repositories [4–8]. The research presented was conducted by a number of different collaborative teams, and the results have been (or will be) published. The work presented, when not my own, contains crucial inputs from all members of the collaboration, myself included. The thesis itself is my original text, barring internal editing, or external editing in the case of published text; note that we have the copyright on the content of all published articles.

Chapter 2 — Dr McGinley, Mr Leontica, Dr Garratt, JJ and Prof Simon:
Parts of this chapter are based on our paper[1]. I have contributed to the development of the measurement protocol and in deciding what to measure, alongside Dr McGinley and Dr Garratt. I have assisted in the execution of the experiment, although in a minor way, with the main effort coming from Mr Leontica and Dr McGinley. The main analytical results were proven by Dr McGinley. I have not contributed significantly to the write-up; hence, no text is taken from Ref. [1]. I have provided my own account of the experiment in Section 2.3; everything preceding it discusses the measurement protocol and the physical significance of properties we have measured (parts where I have contributed significantly) and everything following it is my unpublished work, except Appendix 2.A, which contains a calculation done by Dr McGinley and me.

Chapter 3 — JJ, Dr Wille, Mr Timmers and Prof Simon:
The entire chapter is based on our paper[2] for which I was the main contributor in devising the elements of the experimental proposal, running numerical experiments,

and writing the paper. This does not in any way diminish the contributions of my co-authors, without whom this project would not have been done to the high standard that it is. Personally, I am very grateful to Dr Wille and Prof Simon for their internal editing of the parts of the text I have written, and for Dr Wille's handling of the submission process and the implementation of the journal's notes. With this in mind, I have taken only parts of the paper that I have written, with minimal adjustments. The chapter is supplemented by my original text, with the last appendix presenting some unpublished original calculations.

Chapter 4 — JJ, Dr Placke, Prof Parameswaran and Prof Simon:
The results of this collaboration[3] has not yet been published. The work arrangement is similar to the previous project[2]. The chapter consists of my original text and results.

Contents

List of Figures

List of Abbreviations

NISQ . . . . . Noisy Intermediate-Scale Quantum devices, current generation of quantum computers and simulators.

dof/dofs . . . . A degree of freedom or degrees of freedom.

OpEE/OE . . Operator-space Entanglement Entropy, any entanglement entropy measure on a state dual to an operator.

bOpEE . . . . Bipartite operator-space mutual information, $I_2(A:B)$, between regions A and B.

tOpEE . . . . . Tripartite operator-space mutual information, $I_3(A:B:C)$, between regions A, B and C.

HP . . . . . Hayden-Preskill of Hayden-Preskill teleportation protocol.

LOCC . . . . . Local Operation and Classical Communication, a set of operations assumed accessible to quantum devices.

MPS . . . . . Matrix Product States, a low entanglement variational subspace of the Hilbert space.

TEBD . . . . . Time-Evolving Block Decimation, an approximate time evolution within the MPS variational space.

TFIM . . . . . Transverse Field Ising model, an exactly solvable model on a qubit chain.

MFIM . . . . . Mixed Field Ising Model, a non-solvable generalisation of TFIM.

QEC . . . . . Quantum Error Correction or Quantum Error Correcting.

TC . . . . . Toric Code model, a simple model of topological QEC code.

So once you do know what the question actually is,
you'll know what the answer means.

— from *"The Hitchhiker's Guide to the Galaxy"* by Douglas Adams

1 Introduction

It is without a doubt that analytical solutions to the equations of motion derived from the laws of physics provide an unparallel insight into the inner workings of our world. In fact, analytical solutions are, as I would argue, more important than the laws themselves when it comes to understanding our observations. They often predate the equations they are solving; for example, Kepler's laws predate Newtonian gravity by almost a century.

However, it is almost always extremely difficult to construct exact solutions by starting from equations alone. The earliest exact solutions, in any field, are usually highly symmetrical; think of Schwarzchild's or cosmological solutions to Einstein's gravity. The problem with assuming high symmetry is that it constrains the kinds of phenomena one can obtain from solving the equations; hence, one is not really exploring the full scope of the problem.

From the inception of computers in the middle of the last century, physicists have been using them to numerically solve various problems in classical dynamics, an endeavour that has proved to be most useful. These machines provide a controllable experimental platform on which we can execute numerical experiments and by examining the results (like Kepler observing the night sky) infer possible phenomenologies allowed by the equations without presumptions.

From the motion of the celestial bodies to the thermodynamics of interacting gasses, there is no field of classical physics that has not been revolutionised by the development of classical computing. However, much of quantum many-body physics is profoundly out of the reach of classical machines.

The reason for this is the mismatch of the spaces of possible states between quantum systems and classical memory. Classical memory, just as any classical system, has its states labelled by definite configurations of local degrees of freedom (dofs), classical bit strings; with classical algorithms taking us between these configurations in a predefined way. However, the states of a quantum system, the wavefunctions, exist in a vector space, the Hilbert space $\mathcal{H}_S$ of the system, in which the states of the corresponding classical system merely label one of many choices of basis.

If the classical system has q^L possible states (where L measures the size of the system and q the complexity of the local constituents), a pure state of the quantum system is defined with $(2q^L - 1)$ real numbers. On a classical computer, in which we can only represent some finitely many real numbers, say N of them; this now results in

$$"|\mathcal{H}|" \sim \mathcal{O}(N^{2q^L-1})$$

states that we need to represent to perform a simulation of a quantum system of size L at some precision $\epsilon \sim 1/N$.

This scaling is prohibitive[1] for studying quantum many-body systems via classical simulations, and as Feymann famously said[9], we need quantum computers to simulate quantum systems.

In addition to the exponentially larger state space, quantum systems evolve via an expanded set of operations; unitary rotations within the state-space and projective measurements. With the expanded state-space and operation set, quantum systems themselves have more computational power than classical systems [10]. This means that they can perform certain computations in exponentially fewer steps and require

[1]Unless we employ variational methods, but the choice of the variational space itself, just as imposed symmetries, limits the phenomenology that can be manifested by our solutions.

exponentially fewer memory units, quantum bits, or qubits; as well as opening up new communication protocols[2].

This promise is the reason behind the push to develop quantum devices that can perform useful algorithms. This thesis is a love letter to great technological advancements in programmable quantum devices. Although in the current *Noisy Intermediate Scale Quantum (NISQ)* era, these processors cannot be readily used in algorithmic applications[3], they are shaping to be a powerful tool in the study of many-body quantum physics. A true *Quantum Simulator* will allow us to infer new phenomenologies in quantum many-body systems, in the same manner that classical simulators have done already.

Noise and decoherence in these current machines force us to make concessions. Noise sets an upper limit on the complexity of operations we can perform and states we can prepare directly. However, this adversity is a source of inspiration, and many methods have been developed to work around it, allowing researchers to investigate various aspects of quantum many-body physics: Hilbert space sampling[13], time-crystalline order[14], protected edge modes[15], measurement-induced entanglement transitions[16], and many more.

Overview of our Contributions. This thesis is a collection of seemingly disparate works that are united by the common question. *What can I use NISQ devices for?* Of course, more connections will become apparent as we go, but the main idea is that the following chapters are concrete proposals that aim to showcase some aspects of quantum many-body phenomenology on NISQ devices.

This is naturally a very broad question, and these examples do not in any way form an exhaustive list. The first chapter deals with quantum information scrambling and transport in quantum systems; the two topics are unified by the

[2]Precisely speaking, a subset of operations that is assumed to be realistically accessible in various studies of quantum computing and communication protocols is called local operations and classical communications (LOCC)[11]. Unitary rotations and projective measurements involve a few dofs in close vicinity, while classical information (the results of measurements) can be transmitted long distance, influencing the choice of local operations on distant patches of the system. The quantum teleportation protocol is an excellent example of this operation set in use[12].

[3]Algorithmic quantum computation requiring, just as its classical counterpart, fault-tolerance and error-correction.

introduction of entanglement measures on the time-evolution operator itself. The second chapter deals with probing the properties of a certain class of topologically ordered phases of matter on quantum devices. The last chapter will briefly report on a new measurement-induced phase of matter that we have discovered in our study of quantum codes.

In the next three sections, I will elaborate the motivation for each study separately.

1.1 Entanglement Development; Scrambling and Transport

The main measure that tells us how non-classical certain quantum states are is the entanglement entropy. In both quantum states and classical ensembles of states, the entanglement entropy captures the correlations between regions in our system. Quantum correlations saturate bounds placed on the classical correlations.

For a toy example, take two spins $s = 1/2$, and take two states

$$\rho = (|\uparrow\uparrow\rangle \langle\uparrow\uparrow| + |\downarrow\downarrow\rangle \langle\downarrow\downarrow|)/2 \text{ and}$$

$$|\Phi^{\pm}\rangle = (|\uparrow\uparrow\rangle \pm |\downarrow\downarrow\rangle)/\sqrt{2}.$$

They are, respectively, a classical ensemble consisting of two classical states, represented by a density matrix, and an *entangled* quantum state[4], a quantum superposition of the same two classical states. In this context, a state is considered classical if it is not a superposition of multiple basis states labelled by the classical configuration of local dofs, a special case of what is more broadly called a product state.

Note that a lone classical state cannot have non-local correlations nor entanglement, but classical statistical ensembles of them can, as we will see in a moment. Although an ensemble of classical states may consist of exponentially many of them, their properties are almost always computable classically by various sampling

[4]A EPR pair, the unit of entanglement in qubit systems.

algorithms[5]; hence, they are often within the realm of classical computability, unlike highly entangled quantum states.

Both the ensemble and the entangled quantum state have the same correlations in the z-component of the spin, $\langle\sigma_1^z\sigma_2^z\rangle_\rho^c = \langle\sigma_1^z\sigma_2^z\rangle_\Phi^c = 1$ [6] , while for the other two components only the quantum state has established correlations, $\langle\sigma_1^{x,y}\sigma_2^{x,y}\rangle_\rho^c = 0$ and $\langle\sigma_1^{x,y}\sigma_2^{x,y}\rangle_{\Phi^\pm}^c = \pm 1$. This difference is captured by the entanglement entropy measure called the bipartite mutual information, defined later in the text, which in the two states takes the values of $I_\rho(1:2) = 1 < I_{\Phi^\pm}(1:2) = 2$.

Note that the state ρ is as correlated as the ensemble of classical states can be, and the maximally entangled quantum state $\Phi^\pm$ is more correlated than ρ[7]. Furthermore, no local unitary operator that acts separably on the two spins can increase this entanglement, and measurements can only decrease it irreversibly (or leave it unchanged), making it a precious resource in quantum computing and communication, since it requires effort to build it up over long distances[8].

Given this fact, it may be surprising that closed many-body quantum systems out of equilibrium naturally build up entanglement over time. This is the reason why their dynamics is outside the realm of classical computability. Furthermore, different systems, starting from a product state, develop entanglement at different rates. Most notably, this is a signature that differentiates Anderson-localised systems and many-body-localised systems, which are both insulators throughout the energy spectrum. That is, Anderson-localised systems do not develop entanglement, while many-body-localised systems do so logarithmically slowly[19]. Whereas, generically, in both integrable[20, 21] and thermalising[22, 23] systems, the entanglement develops linearly with time[9].

I will single out two features of quantum many-body time evolution that can be related to entanglement development; scrambling, the loss of the initially local

[5]E.g. Monte-Carlo type algorithms[17, 18]. These sampling algorithms work well because classical ensembles do not have *the sign problem* that generic highly entangled quantum states do.

[6]The statistical correlation between two observables being defined in the usual way $\langle\cdot\cdot\rangle^c = \langle\cdot\cdot\rangle - \langle\cdot\rangle\langle\cdot\rangle$, and $\boldsymbol{\sigma}$s being the usual Pauli matrices.

[7]This additional entanglement is also referred to as *distillable* entanglement, see Section 2.1.1.

[8]Noise and decoherence erode this quantity in the same manner as measurements.

[9]Note that many more non-generic behaviours can be engineered[24, 25]

information to increasingly non-local observables; and transport of conserved densities, a semi-classical portion of the time evolution. In our work, we have proposed a series of experiments, some of which we have also implemented, that utilise entanglement entropy measures to probe these two aspects of quantum time evolution on a NISQ device in a manner that is initial-state independent and efficient in terms of quantum resources (number of qubits required).

The way in which we avoid dependence on the initial state is by considering the entanglement growth properties of the time evolution operator itself. The quantities we consider are related to the operator-space entanglement (OE or OpEE), also known as entanglement in time[26–29]. While, as we saw, the usual state-space entanglement captures quantum correlation at one given time slice, the entanglement in time captures correlations across time, essential for studying scrambling and transport.

Traditionally, to measure entanglement entropies (in contrast to measuring expectation values of observables), the experimentalist needed to prepare multiple (two in the case of the second Rényi entropy) copies of the system in the same state and perform joint-state measurements[30–34]. This challenge was addressed by the introduction of randomised measurement protocols[35, 36], finally formalised by classical shadow tomography[37]. We generalise the classical shadow tomography to be used on characterising quantum channels (e.g. time evolution channel) in order to estimate various OpEE measures that we have related to the two aforementioned properties of quantum many-body time evolution.

Scrambling. From the ultimate faith of the information falling into the black hole[38–41] to the apparent mystery of unitary equilibration[42–45], scrambling plays a central role in our understanding of many-body quantum dynamics. In both cases, the seemingly paradoxical loss of information about the initial state in a closed system is accounted for when considering increasingly non-local observables that are practically inaccessible to an observer[10].

[10]In terms of correlation across time, simple operators (involving a few dofs) at the initial time are correlated almost exclusively with complex (involving many dofs) operators at the final time.

One formal way to phrase the question is via Hayden-Preskill (many-body) teleportation fidelity[38], see Figure 2.1b. This quantity measures how well I can reconstruct a quantum state on a small patch of the system at the initial time, while having access to observables on some other small patch of the system (and additional resources, which I will define later) at some later time. If the fidelity is high for any choice of the final patch, we say that scrambling occurred. Unitary evolution cannot destroy initially local information, so this recoverability is crucial; and the fact that we can recover the quantum information regardless of the choice of the final patch confirms that the information has been as delocalised as it can be. In fact, if this is the case, without the additional resources, one would need access to all observables on the entire system to reconstruct initially local information[28].

This is not the only diagnostic tool; scrambling has been associated with the decay of out-of-time-order correlators (OTOCs)[40, 46–48]. However, the decay of OTOCs can be mimicked by the effects of noise and decoherence, making it ill-suited as a probe of scrambling in NISQ devices; while the effects of noise can only decrease the fidelity of the many-body teleportation, doing the opposite, suppressing the observed effects of scrambling.

We introduce an OpEE measure which we relate to the fidelity of the many-body teleportation, that is, we define a threshold which when exceeded by this quantity the fidelity must be finite. By not measuring fidelity itself, which would require us to decode the scrambled information, we have kept the experimental overhead to a minimum[11], an important factor when dealing with NISQ devices. To demonstrate the practicality of our proposal, we execute it on the `ibm_lagos` quantum processor, thus demonstrating that we have observed scrambling in addition to other phenomena such as operator growth.

Transport. In the case where conservation laws forbid local relaxation via scrambling, the information about the initial distribution of conserved densities is lost via transport. The framework used in the study of transport in quantum many-body systems is the same as in classical systems, that being hydrodynamics[50];

[11] Considerably less than some prior experiments on quantum information scrambling[49].

hence, the relaxation of conserved density imbalances in the initial state represents a semi-classical portion of the full quantum time evolution. The emergence of this hydrodynamical picture in unitary evolution, a question closely related to closed system thermalisation itself, is piquing a good deal of interest recently[51–53].

We introduce another OpEE measure related to the classical information capacity of the channel, which is bounded by the decay of slow hydrodynamical modes. This quantity can be estimated with the same protocols used in our experiment on scrambling, and by doing so we are able to infer transport properties of our system without the exact knowledge of the forms of conserved densities. The experimental overhead in estimating this quantity is linear in system size, making this protocol highly scalable.

However, this quantity decays with noise and decoherence, unless the noise is charge preserving, a fact that one needs to have in mind when implementing it on large qubit arrays. Instead, I present a selection of analytical and numerical results on a set of toy models exhibiting a wide range of transport behaviours to showcase the descriptive power of this measure in the study of transport.

The reader will find further information in *Chapter 2*.

1.2 Realisations of Topological Phases of Matter

Returning to the topic of non-local correlations and entanglement. Intrinsic topological order is a peculiar kind of order that is invisible to local observables while featuring rich phenomenology. From fault-tolerant quantum memories[54] to modelling fundamental interactions (gauge field theories)[55], it is no surprise that studying these models has captivated the community for almost half a century.

The most notable features of such models in (2+1) dimensions are the excitations they host. They lie beyond the fermion-boson dichotomy of $(3+1)$ dimensions. Upon the exchange of these particles, the effects on the state (wavefunction) of the system are highly non-trivial.

The theoretical study of these particles, called *anyons*[56], has mostly reached completion. It was a long road from their first conceptualisation in 1977[57],

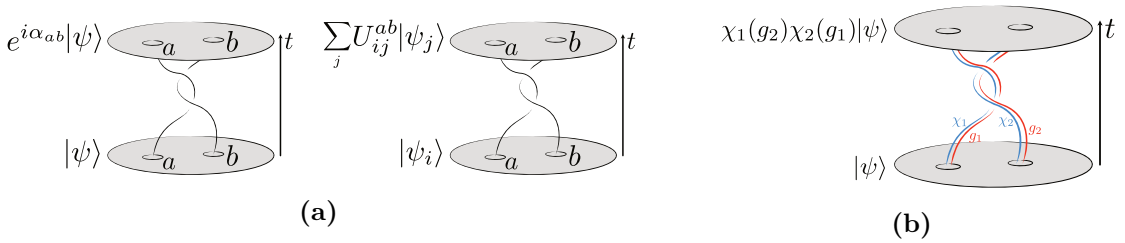

Figure 1.1: (a) The action of the full exchange of Abelian(left) and non-Abelian(right) anyons. The Abelian action induces a phase shift in the wavefunction $|\psi\rangle$, while the non-Abelian action is a unitary rotation is some subspace spanned by $\{|\psi_i\rangle\}$, allowing the braiding of non-Abelian anyons to be non-commuative. (b) The braiding action of anyons in Abelian quantum double model, the anyons are labelled by an irrep of group G χ and a group element g.

through the discovery of the fractional quantum Hall effect[58] in 1982, the first phase to have them as elementary excitation[59, 60], and the formal constructions of various lattice models that realise them[61, 62] in the early 2000s, up until modern category-theoretic approaches[63].

Experimentally, it is a different story. To understand this, we need to look at the two main types of anyons: Abelian and non-Abelian, see Figure 1.1a. The main difference is that exchanging Abelian anyons can only induce a phase shift in the wavefunction[12], $|\psi\rangle \to e^{i\alpha_{ab}}|\psi\rangle$, while exchanging non-Abelian anyon induces a more general unitary transformation on the state, $|\psi_i\rangle \to U^{ab}|\psi_i\rangle$.

Recent experiments have demonstrated Abelian anyon fractional statistics in fractional quantum Hall systems via anyon interferometry[64–66], but convincing signatures of non-Abelian statistics have not been found in quantum Hall systems yet[13].

However, a different avenue for realising topologically ordered states has closed that gap, that is, Quantum Simulators. Since the first demonstration of Abelian anyon braiding on a NISQ device in 2021[68] it did not take long for the same group (Google Quantum AI) to realise projective non-Abelian anyon braiding in 2022[69], the finding being replicated shortly by other groups[70]. Unitary non-Abelian anyon braiding followed soon in 2023[71]. It is in that landscape that our work, contemporary to the last two papers mentioned, finds itself.

[12]Bosons and fermions are special cases of Abelian anyons with $\alpha_{bb} = 0$ and $\alpha_{ff} = 2\pi$, respectively.

[13]Closest probably being Ref. [67], but the data is unclear.

Beyond pure phenomenological interests, anyons do offer a platform for fault-tolerant quantum computation[61, 72], and it is with that in mind that I also highlight the experimental realisation of a topological phase whose excitations form a computationally universal anyon theory[73], Fibonacci string-net model[62]. The topological phase we considered, the quantum double of a finite non-Abelian group, can be made[14] computationally universal with addition of measurement[74].

Ground state preparation. The ground states of topologically ordered systems possess non-local correlations that need to be built up over the entire systems, given that we start off from a product state. These non-local correlations are exactly what encodes the anyon exchange statistics[15]; and since non-Abelian anyons have more complicated exchange statistics, the ground state entanglement structure is more complicated than that of Abelian topological order.

This is a challenge in a noisy device, the depth of a local quantum circuit that would establish these correlations scales linearly with the system size[75]. This limits us to small and simple systems; while noting that there are protocols developed, e.g. Ref. [76], to overcome this challenge by using adaptive circuits, i.e. circuits that adapt based on the results of intermediate measurements, measure-and-feedforward techniques[16].

Group multiplication. Quantum double models have degrees of freedom that take values in a finite group G, hence the action of group multiplication is as natural as bit flips are in the case of qubits (which naturally encode $G = \mathbb{Z}_2$). Once the map from group elements to qubits is performed, the encoding, the group multiplication operator may be compiled in terms of available gates, and it is there that the main difficultly lies. In the case we examine, $G = D_4$[17], we require multiple uses of a three qubit non-Clifford Toffoli gate, that when compiled in the native

[14] In case of non-nilpotent groups, i.e. S_3.

[15] Just like in one-dimensional spin chains, when one wants to write down a fermionic operator on bosonic dofs, the operator needs to be non-local in order to encode the anti-commuting property.

[16] The full power of the LOCC operation set can establish entanglement over a long distance with local adaptive circuits of depths that scale no faster than the logarithm of the system size, in the case of certain topologically ordered ground states, this is possible in constant depth.

[17] Symmetry group of the square, dihedral group of order $8 = 2^3$, encoded on three qubits. See our Paper [2] for analysis of $G = S_3$ case.

gate set of Google's Sycamore chip (our benchmark for the state of the art NISQ device) become depth-6 circuits. Overall, a general group multiplication unitary, $U : |g, h\rangle \to |g, gh\rangle$, in the case of D_4, are depth-50 circuits.

Several of our innovations used to get the overall circuit depth within feasibility rely on the fact that when[18] one of the inputs to the circuit is restricted to be within a particular conjugacy class or a particular normal subgroup, the group multiplication circuits are dramatically simpler. In the case of D_4, the depth is usually 4, with the maximum being 10.

Ribbon operators and charge measurements. These represent our biggest contributions and can be used in conjunction with ground-state preparation protocols described in Ref. [76]. In particular, our charge measurement protocol, if implemented, would offer the first direct detection of topological charge (a needed resource in making these models computationally universal), allowing one to observe non-unique fusion and non-Abelian braiding directly. This is in contrast with indirect (while still unambiguous) observation of non-Abelian signatures, as in Refs. [69–71].

Quantum double models are based on discrete models of gauge field theories, and the anyons they host are a reflection of that fact. The anyons come in three kinds: pure charges (think electric charges in electromagnetism), pure fluxes (local violations of the Gauss' law by a given field configuration) and the combination of the two.

Pure charges, just as in gauge field theory, are associated with irreducible representations (irrep) of the (Gauge) group G, i.e. how does a charged state transform under a local gauge transformation. Pure fluxes are, in turn, labelled by the group elements themselves, conjugacy classes to be specific.

If the group G is Abelian, the classification ends there; all anyons are labelled by an irrep and a group element (χ, g) that we can think of a $\chi-$charge sitting next to a $g-$flux, and the braiding action is determined by the interaction between the charge of one and the flux of another anyon, $e^{i\alpha_{12}} = \chi_1(g_2)\chi_2(g_1)$, see Figure 1.1b. The classification of the anyons in the non-Abelian quantum double models

[18] Group being solvable is a probable necessary prerequisite.

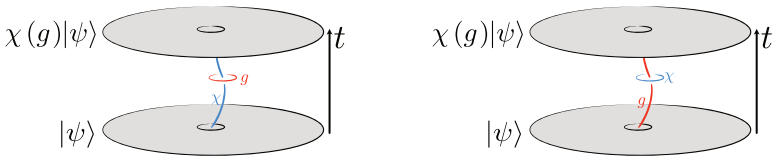

Figure 1.2: (Left) The effects of the local $g-$valued action on the state charged with irrep χ, in the Abelian case. (Left/Right) Charge measurement can be adapted to be a non-destructive flux measurement using this correspondence.

as well as the braiding action is analogous but significantly more complicated; they will be discussed in detail in Chapter 3. The anyon label (χ, C) is referred to as the topological charge.

Ribbon operators are operators supported on a ribbon of finite thickness that leave topological charges at each end of the ribbon while not disturbing the vacuum (ground state) along their path - their endpoints are the elementary excitations of the model, the anyons we discussed. They are labelled by the anyons they create (χ, C). The group multiplication that is needed for their implementation is restricted to the conjugacy class C, which makes its compilation very efficient. We provide a general algorithm for any group G, with exact circuits for the case of $G = D_4$[19]. This is an ancilla-based protocol, with post-selection necessary because of the non-unitary nature of elementary ribbon operators themselves.

To infer the gauge charge part of the full topological charge, one needs to look at how the state transforms under local $G-$action, see Figure 1.2 (Left). To compile a circuit that implement this group action, one needs multiple group multiplication circuits, which is highly non-feasible.

Instead of looking for full charge information, we consider how the state transforms under a subgroup $H-$action, $H \subset G$. This gives us partial charge information, i.e. it does not specify a single irrep, but a set of irreps compatible with the measurement result. By repeating the experiment multiple times with different subgroups, we can infer full charge information with minimal post-processing. This is guaranteed by the partial orthogonality of character tables of the full group and its normal subgroups.

[19] See Ref. [2] for $G = S_3$ case.

The group multiplications used to compile a subgroup action have their domain limited to a subgroup, making them efficient to compile for the cost of having to repeat the experiment multiple times; a usual resource *tradeoff* needed to be considered when compiling an experiment for NISQ devices, circuit depth for repetition with post-processing/post-selection.

We have compiled shallow circuits for the *reduced* charge measurement in the case of $G = D_4$, along with offering a general algorithm for any G.

For the flux content of the full topological charge, we can read out the states of all dofs, getting a classical gauge field configuration and inferring the Gauss' law violations from it to get the flux information, which we do. However, this destroys the quantum superposition of classical gauge field configurations. A non-destructive way of measuring flux can be adapted from the reduced charge measurement by considering the duality shown in Figure 1.2 (Left/Right). The meaning of the local $\chi-$action will become clear at the end of Chapter 3.

Probing non-Abelian signatures. To demonstrate the practicality of our protocols, we numerically simulate a number of experiments demonstrating several elements of the non-Abelian anyon phenomenology. The simulations were performed with Google's own realistic classical simulator, whose noise models were developed based on the `Sycamore` chip[77]. The results are suggestive that current NISQ devices running our protocols can observe: non-unique anyon fusion, non-Abelian anyon braiding, as well as measure most of the topological data (linking and twist matrix elements) in a phase-sensitive manner via our anyon interferometry protocols. The most complicated of our experiments do distinctly go beyond what the current devices are capable of.

The reader will find further information in *Chapter 3*.

1.3 Pauli Subsystem Codes

Another method for establishing long-range entanglement that I will touch upon is local measurements or imposing local constraints on the quantum state. Encoding quantum information into long-range entangled states that satisfy an extensive

number of local constraints[20], is the idea behind quantum error correction (QEC) and QEC codes[78–80]. Local errors present in NISQ may change the state locally (which we can correct), but the relevant information is left untouched. The most well-known example of QEC codes are (topological) stabiliser codes.

They are defined in terms of an Abelian stabiliser group S of operators acting on the Hilbert space $\mathcal{H}$ of some system. States that are left invariant (stabilised) by all elements of the stabiliser group span a logical (or a code) subspace of the full Hilbert space,

$$\mathcal{H}_L(S) = \text{span}\{|\psi\rangle \in \mathcal{H} \mid g\,|\psi\rangle = |\psi\rangle \text{ for all } g \in S\}. \tag{1.1}$$

It is in that subspace that we encode the relevant quantum information, and in good codes, operators that act in this space, the logical operators, cannot have small local support in terms of original dofs. This is because we do not want local errors to mimic the effect of logical operators corrupting the information encoded in the logical subspace. This non-locality condition implies that the states in the logical subspace must have non-local correlations. However, stabiliser states are a class of quantum states that have properties within the realm of efficient classical compatibility[10], a fact that we leverage in our (numerical) study.

A generating set (of operators) for the stabiliser group S, is also called a set of checks, since if a state satisfies all checks, it is necessary in the logical subspace. Furthermore, if the local dofs are qubits and the operators $g \in S$ are Pauli strings, i.e. of the form $g = X_1 \otimes Y_2 \otimes \mathbb{I}_3 \otimes Z_4$ (X, Y and Z being the Pauli matrices), the resulting codes are known as Pauli stabiliser codes[21].

If we relax the Abelian condition on the checks, we get Pauli subsystem codes[81, 82]. These are still codes, with a well-defined code space, defined by the states stabilised by all operators in the maximal Abelian subgroup of the group spanned by all check operators (the Gauge group)[22]. Since the checks do not commute, they

[20] A prominent example of which are precisely the topologically ordered states discussed in the last section.

[21] Since the stabiliser group S is a commuting subgroup of the $n-$qubit Pauli group $\mathcal{P}_2^n$. Note: Logical operators will form a (smaller) Pauli group[10], see Figure 1.3 (bottom) for an example.

[22] If the gauge group is Abelian, we get back a usual stabiliser code.

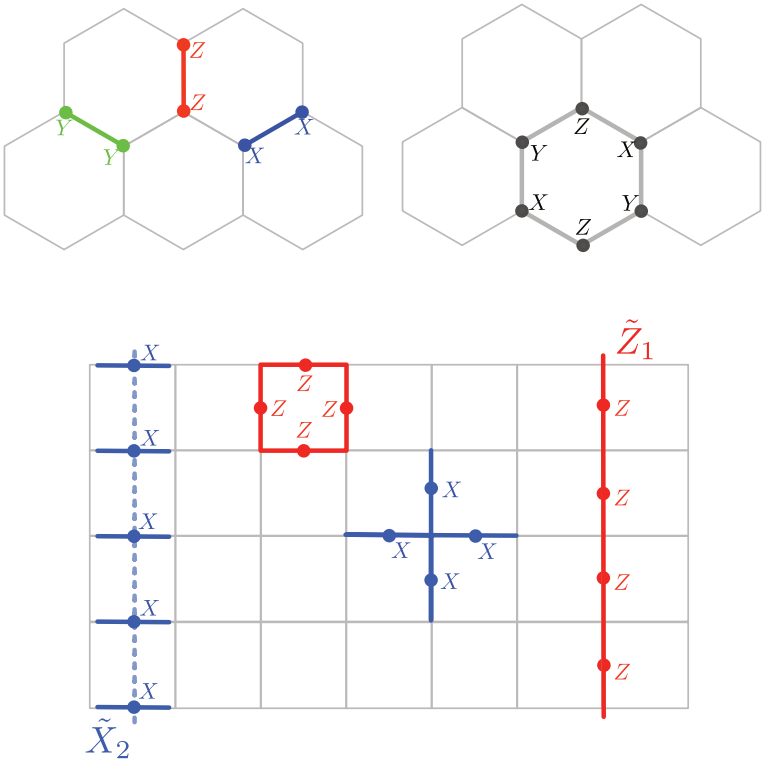

Figure 1.3: Checks versus stabilisers:
(Top) Honeycomb model, the dofs are qubits situated at the vertices of a honeycomb lattice and X, Y and Z are the Pauli matrices. In the subsystem code formulation of the Kitaev honeycomb model, we can choose for our checks to be the *two-qubit* bond operators, but the smallest stabiliser is a *six-qubit* plaquette operator.
(Bottom) Toric code model, the dofs are qubits situated at the edges of the square lattice. The smallest stabiliser generators are *four-qubit* plaquette and vertex operators. A possible choice for two out of four generators of all logical operators $\tilde{X}_2$ and $\tilde{Z}_1$; any deformation of the loops results in the same logical operator with its support always being at least $\mathcal{O}$(linear system size). To get candidates for $\tilde{X}_1$ and $\tilde{Z}_2$ one can rotate the previous $\tilde{X}_2$ and $\tilde{Z}_1$, respectively, by 90^o.

will act on the code space, but in good subsystem codes, their action factors the logical space into two subsystems: the gauge subsystem and the logical subsystem. Gauge operators act trivially within the logical subsystem, and it is there that quantum information is stored. The reason why subsystem codes may be desirable is that, in general, gauge generators can be chosen to be operators of small support, smaller than the generators of the stabiliser group. Hence, the checks are easier to implement as measurements than the stabilisers; see Figure 1.3 (top) for an example.

In recent years, there has been good effort in classifying topological Pauli stabiliser and subsystem codes in terms of Abelian anyon theories[83, 84]. This

categorisation was later used in the characterisation of intrinsically mixed-state topological order (imTO)[85–88], density matrices with loop operator (1−form) symmetries satisfying an algebra that is impossible to realise in pure states. These mixed states arise when we decoherently proliferate locally correlated (i.e. not mutually commuting) errors. Our approach is orthogonal to this line of work; we ask: what if you measure these competing errors instead?

The (Pauli stabiliser) code we focus on is the toric code[23], shown in Figure 1.3 (bottom) and covered in detail in Chapter 4; and the errors we proliferate by measurements are the short strings that leave different kinds of defects at their endpoints, the ribbon operators of the last section.

We have studied this problem numerically, in the stabiliser state or Clifford formalism[10], an efficient tool for classically computing properties of states definable by eq. (1.1). We report a number of different behaviours (phases, if we may) in the steady-state ensembles of these random measurement protocols. We characterise these different steady-state ensembles not only by their entanglement properties, where many studies of this kind conclude, but by also constructing an Edwards-Anderson-like order parameter that quantifies how likely you are to find a correlated defect-defect (anyon-anyon) pair separated by a long distance in the steady-state ensemble, which we relate to anyon condensation.

The reader will find further information in *Chapter 4*.

[23]The $G = \mathbb{Z}_2$ quantum double model.

I raised to my lips a spoonful of the tea in which I had soaked a morsel of the cake ... suddenly the memory returns. The taste was of the little crumb of madeleine which on Sunday mornings at Combray ... my aunt Léonie used to give me, dipping it first in her own cup of real or of lime-flower tea.

— from *"In Search of Lost Time"* by Marcel Proust

2

Entanglement Dynamics in Qubit Arrays

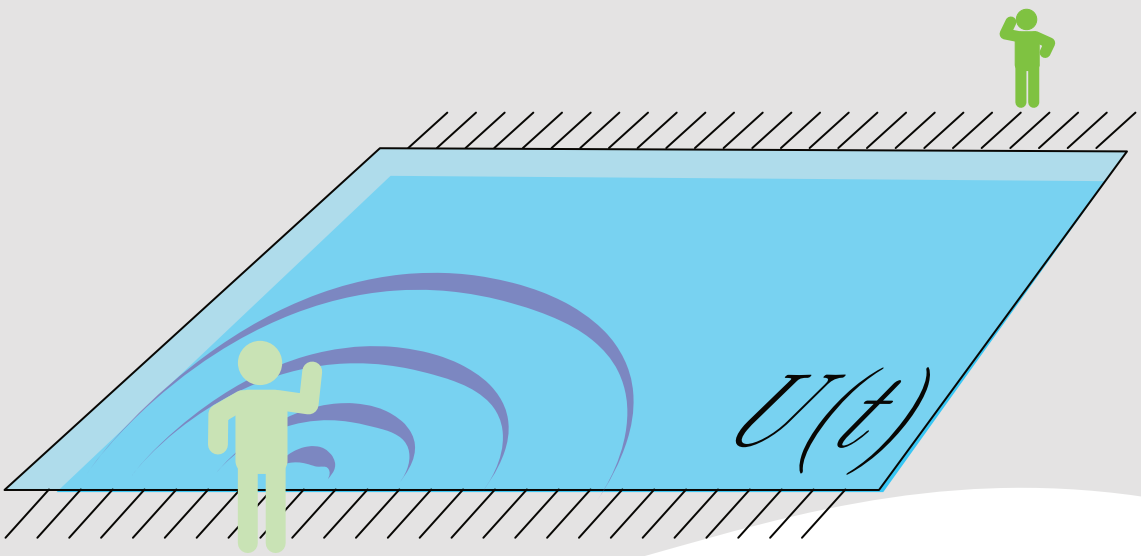

Building on the motivation laid out in the first part of the *Thesis Introduction*, I will now present our work on Operator Entanglement Entropies and Mutual Information, often referred to as just OpEE in this chapter. The main idea is to relate the OpEE measures to the power of a quantum channel (a circuit or a time evolution operator) to scramble or transfer initially local classical and quantum information. In addition to this, we also present how to obtain such measures in a NISQ device with single-qubit control in a way that is quantum resource-efficient (uses as few qubits as possible). This probing is based on the now well-known technique of classical shadow tomography [37], but modified for the use of quantum channel tomography, i.e. estimating OpEE measures.

Parts of this chapter are based on our published work:

> McGinley, M., Leontica, S., Garratt, S.J., Jovanovic, J. and Simon, S.H., 2022. *Quantifying information scrambling via classical shadow tomography on programmable quantum simulators.* Physical Review A, 106(1), p.012441.

In this work, we have demonstrated that a given circuit has achieved quantum information scrambling on a NISQ device by measuring various OpEE measures. We show that if some OpEE measures, defined later, exceed a threshold value, then the circuit has achieved quantum information scrambling in a manner defined in the literature, most notably Ref. [38]. Put simply, the local information is lost to local measurements, but is still accessible[1] if we have access to the entire output of the circuit.

I also supplement this chapter with unpublished work that relates an OpEE measure similar to the ones we considered in our paper to the transport properties of quantum systems. Having demonstrated that we can estimate the OpEE measures on a NISQ device, I argued that we ought to utilise the relationships between classical information transfer of a time evolution (captured by one of the OpEE measures) and the transport properties of a quantum system. This would allow us to measure the transport of local charges more exotic than the often-studied spin transport, we can

[1] Assumings a unitary evolution.

access heat diffusion in chaotic Hamiltonian systems, observe quasiparticle modes, or anything that has a potential to carry classical information around a system.

The chapter is structured as follows. In the next section, I will define all the relevant OpEE measures and their relationships to quantum information scrambling and transport properties of quantum systems. Following that, I will present our variant of the classical shadows tomography that we use to characterise quantum channels. Next, I will present the main results of our published work, before moving on to a set of analytical and numerical results that provide the motivation for why one ought to look at OpEE measures to characterise quantum transport experimentally. I will conclude with a brief chapter summary, leaving the reader with a set of appendices that provide some detailed calculations referred to in the main text.

2.1 Operator Entanglement Entropy

The question arises: Is there a way to quantify the entanglement development during the evolution of a quantum system that is independent of the initial state?

A natural way to address this question is to define an entanglement entropy measure for the time-evolution operator itself. A good candidate for this measure is the Operator Entanglement Entropy (OpEE) [28]. In order to define this measure, we can simply look at an appropriate state dual to an operator:

$$O = \sum_{ij} O_{ij} \left|i\right\rangle \left\langle j\right| \quad \rightarrow \quad \left|O\right\rangle = \sum_{ij} O_{ij} \left|i\right\rangle \otimes \left|j\right\rangle . \tag{2.1}$$

If the operator, O, is acting on states in a Hilbert space, $\mathcal{H}_S$, of some system S; then the dual state, $|O\rangle$, lives in the tensor product of two copies of $\mathcal{H}_S$, $\mathcal{H}_S \otimes \mathcal{H}_{S'}$, or in a Hilbert space of a doubled system, $S \cup S'$. See Figure 2.1a for an illustration. We can then simply use the usual entanglement measures (for a state) applied to this state dual of an operator. The ones we chose to focus on are the Rényi entanglement entropies and mutual information across various multipartitions of the two copies of the system. From now on, I will focus on the case of OpEE of time evolution unitaries, $O = U(t)$.

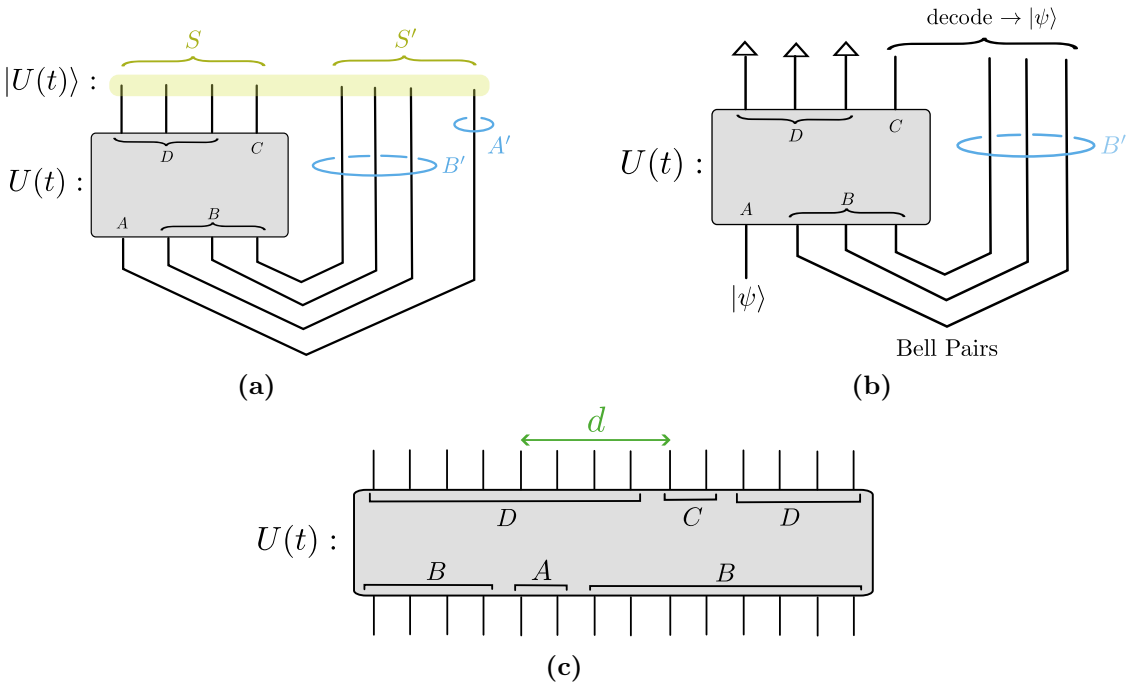

Figure 2.1: (a) Illustration of the operator-state duality on the example of a time evolution unitary, $U(t)$. The state, $|U(t)\rangle$, is defined on the doubled system, $S \cup S'$, which are further divided into regions, $A^{(\prime)}$, $B^{(\prime)}$, C and D. (b) The Hayden-Preskill protocol [38]. The relevant quantum information, state $|\psi\rangle$, to be scrambled is encoded in subsystem A, while the rest of the system, subsystem B, is entangled with its copy, B'. If $U(t)$ is a perfect scrambler, the state $|\psi\rangle$ can be distilled just from the copy, B', and any subsystem C of the same size as A. (c) The subdivision of the doubled system, $S \cup S'$, into four regions, A, B, C and D, used in defining various OpEE measures. We always take that $|A| = \mathcal{O}(1) = |C|$ and $|B| = \mathcal{O}(N) = |D|$.

The state dual to the time evolution unitary can be directly prepared on the doubled system by applying the unitary to one half of a maximally entangled state

$$|U(t)\rangle = U_I(t)\,|\Phi^+\rangle_{I,II} = \sum_i U_I(t)\,|i\rangle_I \otimes |i\rangle_{II}\,, \tag{2.2}$$

where i goes over some basis of the Hilbert space of the system, S.

The main multipartition we will use is shown in Figure 2.1c, $S = A \cup B$ and $S' = C \cup D$. With this partitioning of the two copies of the system, we can define the Operator Entanglement Entropy (OpEE) as:

$$S^{(n)}_{OpEE}(X) = \frac{1}{1-n} \log_q \mathrm{Tr}\rho_X^n \ , \text{ for } \rho_X = \mathrm{Tr}_{\bar{X}}\,|U(t)\rangle\,\langle U(t)|\,, \tag{2.3}$$

with X being any union of the subsystems A, B, C and D and $\bar{X}$ is the complement, $X \cup \bar{X} = S \cup S'$. Here n is the Rényi index and the base of the logarithm is always the on-site Hilbert space dimension, $q = 2$ in the case of qubit arrays.

Using different combinations of multipartitions we can define mutual Rényi information:

$$I_2^{(n)}(A:C) = S_{OpEE}^{(n)}(A) + S_{OpEE}^{(n)}(C) - S_{OpEE}^{(n)}(A \cup C), \tag{2.4}$$

and

$$\begin{aligned} I_3^{(n)}(A:B:C) = I_2^{(n)}(A:B) + I_2^{(n)}(A:C) - I_2^{(n)}(A:B \cup C) = \\ S_{OpEE}^{(n)}(A) + S_{OpEE}^{(n)}(B) + S_{OpEE}^{(n)}(C) - S_{OpEE}^{(n)}(A \cup B) \\ - S_{OpEE}^{(n)}(A \cup C) - S_{OpEE}^{(n)}(B \cup C) + S_{OpEE}^{(n)}(A \cup B \cup C). \end{aligned} \tag{2.5}$$

The first is the bipartite mutual information between A and C, and the second is the tripartite mutual information between A, B and C. The first quantity we will employ in our study of transport properties of quantum systems, while the second quantity we have used in our study of scrambling properties of quantum channels. Both of these quantities can be estimated using our variation [1] of the classical shadows method [37]. However, the number of shots required to estimate the two quantities via classical post-processing is vastly different.

The number of shots required scales exponentially with the size of all partitions involved. In the case of tripartite mutual information, this is $\mathcal{O}(c^{|A|+|B|+|C|})$, while in the case of bipartite mutual information it is $\mathcal{O}(c^{|A|+|B|})$[2], with $|X|$ being the size of (the number of sites in) the region $X \in \{A, B, C\}$. The constant c ($c > 1$), is a $\mathcal{O}(1)$ constant that depends on the desired precision of the estimate.

Note that $S = A \cup B$ ($\cup$ will be omitted in further text, so I write AB), so the number of shots required to estimate the tripartite mutual information is at least exponentially large with respect to the size of the original system S. However, the number of shots required to estimate the bipartite mutual information does not scale with the size of the original system if regions A and C are not extensive. This allows us to vary the position of the region C, which we will do in our study of transport properties of quantum systems, totalling in a linear scaling for the entire experiment.

[2] See the discussion following eq. (2.22) in Section 2.2.

Note that, in the case of a state dual to a unitary (time-evolution) operator, we can further simplify equations (2.4) and (2.5) by using:

$$S^{(n)}_{OpEE}(X) = |X|, \tag{2.6}$$

for X supported solely on either input, S', or output, S, spaces. This is due to the fact that the reduced density matrix, ρ_X, is maximally mixed, $\rho_X = \mathbb{I}/q^{|X|}$.

Also for pure states, we have:

$$S^{(n)}_{OpEE}(X) = S^{(n)}_{OpEE}(\bar{X}), \tag{2.7}$$

but given the actual time evolution is noisy, $\mathcal{N}_t(\rho) \neq U(t)\rho U^\dagger(t)$, I will not use eq. (2.7).

Equations (2.4) and (2.5) now read:

$$I^{(n)}_2(A:C) = |A| + |C| - S^{(n)}_{OpEE}(AC), \tag{2.8}$$

and,

$$I^{(n)}_3(A:B:C) = N + |C| - S^{(n)}_{OpEE}(AB) \\ - S^{(n)}_{OpEE}(AC) - S^{(n)}_{OpEE}(BC) + S^{(n)}_{OpEE}(ABC), \tag{2.9}$$

with the last term being equal to $|D| = N - |C|$, when the evolution is unitary.

2.1.1 Tripartite OpEE and Scrambling

The tripartite OpEE (tOpEE), Rényi mutual information between regions A, B and C connected by the time evolution operator, is one of the two quantities we have looked at in our work on verifiable scrambling in quantum simulators[1]. The main point of the paper is to demonstrate that we have achieved quantum information scrambling on a programmable quantum simulator. We have implemented a circuit corresponding to our time evolution (ideally) unitary $U(t)$, more generally a noisy channel $\mathcal{N}_t[X] \approx U(t)XU^\dagger(t)$, which *we show* has the property of scrambling the initially local quantum information.

This is not the first[49] nor the last[89, 90] study of this kind. What sets our work apart is that it is not as direct, the scrambled information is not directly recovered, but rather we looked at the relevant OpEE measure to determine if the information has been recoverably scrambled. To this end, I will dedicate this section to explain the relation between verifiable scrambling and the tripartite mutual information for a given unitary operator.

Hayden-Preskill Protocol. Scrambling in a quantum mechanical system aims to capture the notion that initially localised information spreads to incredibly complex and growing observables. The information is not lost, but becomes practically inaccessible to an observer. This has been related to the black hole information paradox, resulting in one formal way of defining quantum information scrambling; the Hayden-Preskill (HP) protocol (thought experiment)[38]. The hypothetical proposal deals with retrieving quantum information lost to the black hole, assuming that the black hole event horizon is a fast scrambling unitary. The protocol is illustrated in Figure 2.1b, to be precise, what is shown is an encoding channel $\mathcal{N}_t^{A\to B'C}$. The main idea is to decode the information lost to the black hole, state on the subsystem A, by collecting some Hawking radiation, represented by the subsystem C, from the evaporating black hole. The main resource to which an observer has access is a system B', which is entangled with the black hole, system B.

If a decoder channel is provided, one can ask about the fidelity of the combined encoder-decoder process; this is known as the HP or many-body teleportation fidelity. The quantum information capacity of the encoding channel is defined as this fidelity; and in the case of perfect scramblers, this channel is perfect for any choice of subsystem C as long as $|C| \geq |A|$. More generally, if the capacity of the encoding channel is non-zero, we can distil the state $|\psi\rangle_A$ from $B'C$ (to be defined soon); and if that is the case for any choice of C ($|C| \geq |A|$) the quantum information localised in A is (verifiably) scrambled by definition. It is to this quantum information capacity of an encoding channel that we have related the tOpEE.

In Ref. [28] it was also shown, in a manner similar to what I am about to argue, that the lost information can only be distilled from the entirety of the output, the

whole CD, if the information is perfectly scrambled, which echoes the fact that all the Hawking radiation is needed to decode the information lost to the black hole.

The two approaches are related by the fact that in the case of unitary evolution $I(A : B : C) = I(A : D : C)$.

Distillable Entanglement. In the context of states, e.g. ρ^{XY}, if the bipartite mutual information, $I(X : Y)$, is greater than the dimension of the smaller subsystem, say $I(X : Y) = |X| + \epsilon_{X:Y}$ with $\epsilon_{X:Y} > 0$, and the reduced density matrix, ρ^X, is maximally mixed, we can distill the entanglement[3] from the state ρ^{XY}. This is an example of a *distillation criterion*.

The Bell pair state between identical subsystems, $|X| = |Y|$, maximises the bipartite mutual information between the two subsystems, $\epsilon_{X:Y} = |X|$, and can be regarded as a proper unit of quantum entanglement. With this in mind, we can define the entanglement distillation procedure. Given a state, ρ^{XY}, with distillable entanglement between subsystems X and Y, we can cast a product state $\rho = \bigotimes_{i=1}^{N} \rho_i^{XY}$ into a product state of a number (smaller than N) of Bell pairs between subsystems[4] $X_1X_2 \dots X_N$ and $Y_1Y_2 \dots Y_N$. See Appendix A of our paper[1] for the full discussion and Refs. [91, 92] for concrete examples of distillation procedures.

The casting/distillation procedure is local on subsystems $X_1X_2 \dots X_N$ and $Y_1Y_2 \dots Y_N$. Local in this context means LOCC (Local operations and classical communication)[11], measurements and unitaries act separably on subsystems $X_1X_2 \dots X_N$ and $Y_1Y_2 \dots Y_N$, but the unitaries applied to one subsystem may depend on the outcome of the measurements performed on the other subsystem.

OpEE and HP Protocol. If we now recall the leg folding procedure in defining the state dual to the time evolution operator, Figure 2.1a, we see that unfolding the legs on a Bell pair state gives us the Identity channel. This means that the distillation procedure, if it can be performed based on some distillation criterion, is exactly the

[3]Distillable entanglement is the (additional) entanglement characterising correlations beyond those possible in classical ensembles!

[4]Each Bell pair carrier a quantised amount of distillable entanglement, $\epsilon_{\text{Bell}} = 1$, hence the distillable entanglement of the product state ρ, $\epsilon_{\text{total}} = N\epsilon_{X:Y}$, needs to be close to an integer for that product state to be castable to the reduced Bell pair form.

decoder of the encoding channel $\mathcal{N}_t^{A\to B'C}$. In this way, we have a sufficient criterion in terms of OpEE which we have related to the HP definition of scrambling. That is

> If $I_2^{(n)}(A:BC) > |A|$ for any choice of subsystem C in the output with $|C| = |A|$, we can infer that the information localised in A is verifiably scrambled according to the HP definition.

Why I insist on relating the tripartite OpEE, to the distillation of entanglement, even though the criterion used the bipartite mutual information, $I_2^{(n)}(A:BC) > |A|$, is that this bipartite mutual information is the only nontrivial contribution to the full tripartite mutual information, eq. (2.5), since $I_2^{(n)}(A:B) = 0$ and $I_2^{(n)}(A:C)$ (what I refer to as bipartite OpEE) is generally small for scrambling unitaries.

Later I will present our results, where we have used our variant of the Classical Shadows Method to estimate the tripartite OpEE and show that for the circuits we have implemented the criterion is met, for (almost) all choices of C, demonstrating that the information is verifiably scrambled on our device.

2.1.2 Bipartite OpEE and Transport

In this section, I will argue for the physical significance of the bipartite OpEE (bOpEE), Rényi mutual information between regions A and C connected by the time evolution operator, by relating it to the transport properties of quantum systems. In general, if we look at the second Rényi entropy:

$$2^{-S^{(2)}} = \mathrm{Tr}\rho^2 \tag{2.10}$$

and look at it in the superstate formalism, where we treat operators as states in a doubled Hilbert space, we can write it as:

$$2^{-S^{(2)}} = \langle\langle\rho|\rho\rangle\rangle = \sum_O \langle\langle\rho|O\rangle\rangle\langle\langle O|\rho\rangle\rangle, \tag{2.11}$$

where the norm of this operator vector state is just the Schmid trace norm, $\langle\langle P|Q\rangle\rangle = \mathrm{Tr}P^\dagger Q$. The sum goes over any orthonormal basis of the operator vector space, $\{|O\rangle\rangle\}$.

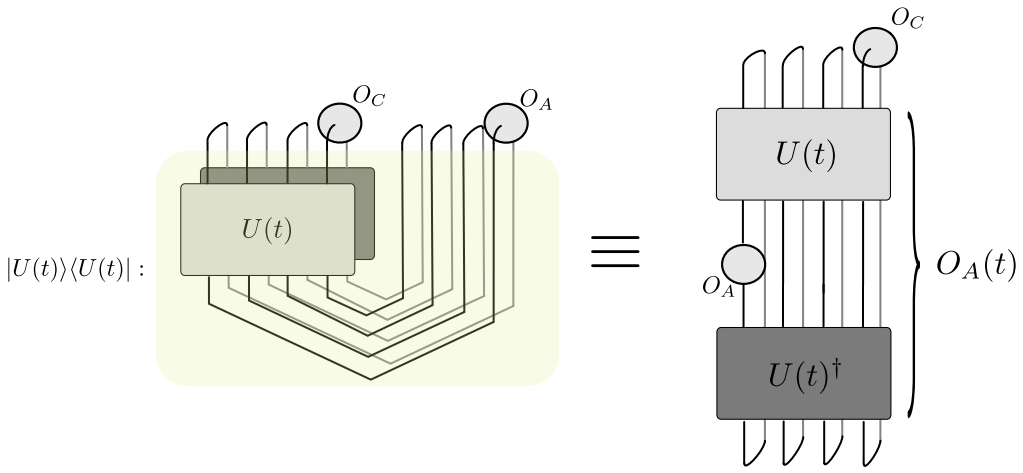

Figure 2.2: Graphical derivation of the equality used in equation (2.13), $\mathrm{Tr}\rho_t O_A O_C = \mathrm{Tr}O_A(t)O_C$.

In this expanded form, the second Rényi entropy can be written as:

$$2^{-S^{(2)}} = \sum_O |\mathrm{Tr}\rho O|^2. \tag{2.12}$$

Focusing more specifically at the case at hand, the second Rényi mutual information between regions A and C connected by the time evolution operator, $\rho = \rho(t) \equiv |U(t)\rangle \langle U(t)|$, and choosing a basis of operators that is factorisable in regions A and C, i.e. $O = O_A \otimes O_C$ for all Os, we can rewrite the equation above as:

$$2^{-S^{(2)}(AC)} = \sum_{O_A, O_C} |\mathrm{Tr}O_A(t)O_C|^2. \tag{2.13}$$

Refer to Figure 2.2 for a graphical derivation of this equation. Note that the sum contains a number of terms exponentially large in the sizes of the subsystems A and C. Both because of the experimental considerations and for the theoretical usefulness of this quantity, the intention is to keep these regions small allowing for the small number of relevant terms, described below, not to be obscured by the vast majority of irrelevant terms.

From equation (2.13) we can already anticipate the relationship between this OpEE measure and the presence of long-lived modes in our system, i.e. the transport properties of the time evolution operator.

Namely, looking at the sum in equation (2.13), we can see that if there is a slow mode in the system, that is, a local density conserved by the time evolution operator,

and there is some operator O_A, supported in the region A that has some operator overlap with the local conserved density operator, the term $|\mathrm{Tr}O_A(t)O_A|^2$ will dominate at late times after all other operators overlaps have exponentially decayed due to local relaxation. This is because that term can only decay algebraically, as fast as the slow mode with which it overlaps.

A picture that excellently captures this point can be found in recent works [93, 94] on the classical computation of transport in quantum systems. The main point of these works was to find a good variational space in which to evaluate a term like $\mathrm{Tr}O_A(t)O_A$ in. The reason for bringing it up is the hydrodynamical picture of said operator overlap, $\mathrm{Tr}O_A(t)O_A$, which can be found in Ref. [93]'s equation (10):

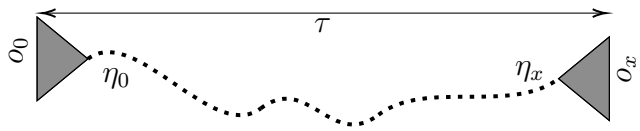

(2.14)

schematically representing the overlap of time-evolved local operator o_0 with the local operator o_x via the dominant slow mode, η_x. The dynamics of this slow mode may fall into a number of different universality classes (diffusive, ballistic, etc.), but in all cases the decay of this quantity in time will be at most algebraic due to symmetry constraints on the time evolution.

The late-time behaviour of this OpEE measure will be determined by the slow modes and, hence, measuring it can give us insight into the transport properties of the time evolution operator.

2.2 Classical Shadows and OpEE

In the previous sections, I have argued for the physical significance of tripartite and bipartite OpEE measures, Rényi mutual information. In this section, I will focus on how to measure these quantities in digital quantum simulators with single-qubit control.

Classical Shadows. *Given a quantum state described by its density matrix, ρ, how can we estimate a large number of functions of ρ with a "small" number of measurement shots?*

The classical shadows protocol addresses this question and is a more systematic version of randomised measurement protocols that came before, e.g. Ref. [36]. All randomised measurement protocols leverage the correlation between the random measurement bases via classical post-processing.

To illustrate this fact, it is best to explain the actual protocol:

Classical Shadows

1. Apply a random unitary to a state, ρ, of interest.
2. Read out the state in an available basis, i.e. computational basis in the case of qubit arrays, and record the outcome, **the quantum measurement**.
3. Repeat the process N times, resulting in a set of random unitaries $\{U_i\}$ and the corresponding measurement results $\{m_i\}$.
4. Given these two sets, classical shadows, construct the appropriate estimators for our target functions, **the classical post-processing**.

The last step of the protocol is the most involved, because it depends greatly on the ensemble of random unitaries used in the first step and on the observable of interest.

The expectation values of usual observable are linear functions in density matrix, $\langle O \rangle = \mathrm{Tr}\rho O$, and hence their estimators will be different from Rényi entropies which are non-linear functions in the density matrix, $S^{(n)} = \frac{1}{1-n}\log\mathrm{Tr}\rho^n$.

Linear functions. Let us focus on the case of estimating expectation values of quantum observables.

Given a set of N random unitaries and corresponding measurement outcomes, $\{U_i\}$ and $\{m_i\}$, we construct a following estimator for the density matrix, ρ:

$$\hat{\rho}_i = \mathcal{N}(U_i \left|m_i\right\rangle \left\langle m_i\right| U_i^\dagger), \tag{2.15}$$

$$\hat{\rho} = \frac{1}{N}\sum_i \hat{\rho}_i. \tag{2.16}$$

It is important to note that the estimator $\hat{\rho}$, can only be used in linear functions $\overline{\mathrm{Tr}\hat{\rho}O} = \mathrm{Tr}\rho O$, where the averaging was done over different realisations of the experiment. [5]

The channel $\mathcal{N}$, depends on the ensemble of random unitaries used in the experiment. In the case where U_i are drawn from the uniform (Haar) measure of random $d \times d$ unitary matrices, U_d, the correct channel producing an unbiased estimator will be:

$$\mathcal{N}(U_i \left|m_i\right\rangle \left\langle m_i\right| U_i^\dagger) = (d+1)U_i \left|m_i\right\rangle \left\langle m_i\right| U_i^\dagger - 1, \tag{2.17}$$

where d is the Hilbert space dimension of the system.

This is different from the common guess of $\mathcal{N}(X) = X$, giving us the density matrix of the state after the measurement, $U_i \left|m_i\right\rangle \left\langle m_i\right| U_i^\dagger$. Each shadow, $\hat{\rho}_i$, is not a valid density matrix (not positive definite), but the average is.

To see why this is correct, we look at what $\hat{\rho}$ estimates:

$$\overline{\hat{\rho}_i} = \int_{U_d} dU \sum_{\{m_\alpha\}} \left\langle m_\alpha\right| U\rho U^\dagger \left|m_\alpha\right\rangle \Big((d+1)U \left|m_\alpha\right\rangle \left\langle m_\alpha\right| U^\dagger - 1\Big) = \rho, \tag{2.18}$$

where m_α is the set of all possible measurement outcomes [37]. The term in front of the parentheses is the probability of observing an outcome m_α.

To get the last equality in the equation (2.18) one can use the well-documented moments of the Haar measure, e.g. Ref. [95]. To get the average, $\overline{\hat{\rho}_i}$, one needs the second moment and to get the variance, $\mathrm{var}\hat{\rho}_i$, determining the number of shots needed to achieve the desired precision, one needs the fourth moment of the Haar measure.

In most practical cases, realising the Haar measure is not feasible with local unitary circuits. Although local random unitary circuits in one or two dimensions can approximate the Haar measure up to a given moment [96][6], the depth of these circuits needs to be extensive in the system size, although there has been great progress in this field [97].

[5] Repeating the experiment is not necessary because the estimator is a self-averaging quantity.

[6] Second moment (a Haar two-design) to give us the correct estimator and forth to give us the favourable low variance in our estimator.

This is why we focus on the on-site Haar ensemble, $U(2)^{\otimes n}$, where n is the number of qubits in the system.

This ensemble now requires a new estimator which is just a tensor product of the previous full Haar estimator on each qubit:

$$\hat{\rho}_i = \mathcal{N}(U_i |m_i\rangle \langle m_i| U_i^\dagger) = \bigotimes_a \left(3U_i^a |m_i^a\rangle \langle m_i^a| (U_i^a)^\dagger - 1\right), \tag{2.19}$$

index a is going over the qubits, unitaries U_i decompose into their local parts $U_i = \prod_a U_i^a$ and the measurement outcomes are labels by the computational basis states, $m_i = \{m_i^a\} \in \{0,1\}^n$.[7]

The on-site Haar ensemble can be realised exactly given that many quantum simulators have individually accessible qubits, i.e. trapped ions platforms[98–101], superconducting qubit arrays[14, 102–105] and Rydberg atom arrays[106–111].

Nonlinear functions. Polynomial functions of the density matrix, e.g. exponentials of Rényi entropies, can also be estimated straightforwardly. The main idea is to cast the degree m function of the density matrix as a linear function of the density matrix of a repeated system, $\rho^{\otimes m}$. This is similar to the usual replica trick used when studying entanglement in quantum systems [20, 112]. More relevantly to experimentalists, this is the trick used in the first direct measurement of the second Rényi entropy in a trapped ion quantum simulator [113].

However, that protocol required a second copy of a state, which requires double the quantum resources (i.e. qubits). Randomised measurement protocols solve precisely this problem via classical post-processing and correlation between random measurement bases.

In the case of second Rényi entropy, the observable on the doubled system is the SWAP operator $\text{SWAP} = \sum_{ij} |i\rangle_1 |j\rangle_2 \langle j|_1 \langle i|_2$, as expected. The expected value of the SWAP operator is the state purity of the original non-doubled system,

$$\text{Tr}\left[(\rho \otimes \rho)\text{SWAP}\right] = \text{Tr}\rho^2, \tag{2.20}$$

[7]Furthermore, in this setting, partial traces are done simply by neglecting the qubits that are traced out from the above tensor product.

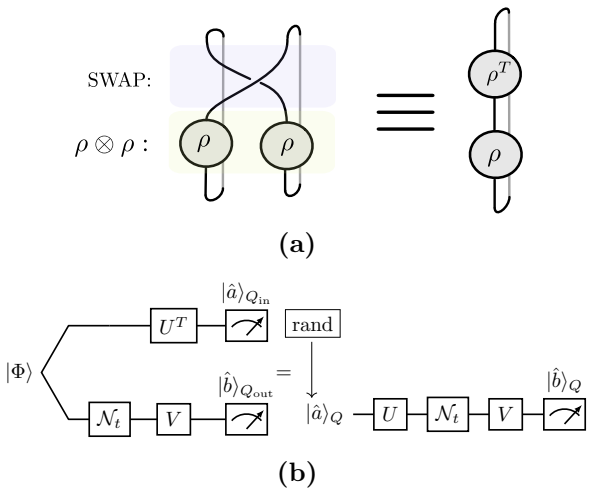

Figure 2.3: (a) Graphical proof of the following equality, $\text{Tr}(\rho \otimes \rho)\text{SWAP} = \text{Tr}\rho^2$. (b) Figure taken from our Paper [1]: Graphical representation of the OpEE variant of the classical shadows protocol. The time evolution channel is labelled by $\mathcal{N}_t$, which in the unitary case reads as: $\mathcal{N}_t(\rho) = U(t)\rho U^\dagger(t)$.

see Figure 2.3a for a graphical representation of this fact.

So in order to estimate the state purity, we just need to estimate the expectation value of the SWAP operator on the doubled system, which is a linear function of $\rho_2 = \rho \otimes \rho$.

The estimator of ρ_2 is suggestively [37]:

$$\hat{\rho}_2 = \frac{1}{N(N-1)} \sum_{i \neq j} \hat{\rho}_i \otimes \hat{\rho}_j, \tag{2.21}$$

with $\hat{\rho}_i$ having the same definition as in the linear case.

The average of the tensor product in eq. (2.21) is the tensor product of averages, since we have removed the diagonal terms in the sum, hence the two shots are independent, giving us the correct average value $\overline{\hat{\rho}_2} = \rho \otimes \rho$.

Shadow Norm and Shot Variance. Theorem 1 in Ref. [37] determines the performance of the classical shadows protocol and is also directly applicable to our variant:

Theorem 1: *The sample size of N shots allows us to estimate M linear functions $(\{\text{Tr}\rho O_i\})$ up to an additive error ϵ given*

$$N > \mathcal{O}(\log(M) \max_i ||O_i||^2_{\text{shadow}}/\epsilon^2), \tag{2.22}$$

where $||O_i||_{\text{shadow}}$ *is an operator norm determined by the ensemble of randomising unitaries.*

For example, if the ensemble is Haar random on the entire Hilbert space, the shadow norm is $||O_i||^2_{\text{shadow}} \propto \text{Tr}O_i^2$[37]. However, more applicable to us is the on-site Haar ensemble, where the shadow norm is $||O_i||^2_{\text{shadow}} \propto 4^k||O_i||_\infty$, where k is the number of qubits O_i acts on and $||O_i||_\infty$[37] is the operator norm of O_i. This gives us exponential scaling in the number of shots needed to estimate various OpEE. In practice, in our paper [1], we have directly estimated the effect of this shot noise by running an ideal simulation in addition to running the protocol on a quantum device.

Classical Post-Processing. Another important aspect of the classical shadows protocol is the way classical post-processing is done. That is, constructing estimators $\hat{\rho}_i$ and storing them in memory is usually not efficient, given the exponential scaling of the dimension of the Hilbert space.

In the case of separable ensembles, where U_is and V_is are tensor products of small matrices (lowest bond-dimension in MPO language), and when the observable is also a simple object, e.g. a local observable or the SWAP operator, it is more efficient to construct the estimator for the functions and store them

$$\frac{1}{N(N-1)}\sum_{i\neq j}\{\hat{\text{Tr}\rho^2}\}_{i,j} = \frac{1}{N(N-1)}\sum_{i\neq j}\text{Tr}\hat{\rho}_i\hat{\rho}_j, \tag{2.23}$$

where the estimator $\{\hat{\ldots}\}_{i,j}$ of a quadratic function in ρ is formed by taking the $i^{\text{th}}$and the j^{th}sample, see eq. (2.21).

OpEE Variant of the Classical Shadows. Having reviewed the traditional version of the classical shadows protocol, I can now explain our variation of the protocol that is tailored for estimating the OpEE measures.

The OpEE are usual entanglement measures when viewed on the doubled system, the tensor product of the input and output Hilbert spaces. However, unlike related experimental works [49, 89], we did not need to double the system to study the state dual to an operator directly, but instead employed the power of randomised protocols (one more time) to remove the need for doubling the system.

Hence, our protocol is a randomised initial state and measurement protocol:

Classical Shadows (OpEE Variant)

1. Initialise the system in a random state, say labelled by $|m_i\rangle$.
2. Apply a random unitary, U_i, to this state.
3. Evolve the system with the time evolution operator $U(t)$, or a unitary circuit.
4. Apply the second layer of random unitaries, V_i, to the state at the output of the time evolution operator.
5. Readout the state in an available basis, say the result is labelled by $|n_i\rangle$.
6. Repeat the process N times, resulting in a set of random unitaries $\{U_i\}$ and $\{V_i\}$, and a set of random initial and final states $\{m_i\}$ and $\{n_i\}$.
7. Given these sets, classical shadows construct the appropriate estimators.

The logic follows in the same way as it did in traditional classical shadow tomography. We construct our estimator for the density matrix of the state dual to the time evolution operator, $\rho(t) \equiv |U(t)\rangle\langle U(t)|$, as:

$$\hat{\rho}_i(t) = \bigotimes_a \left(3(U_i^a)^T |m_i^a\rangle\langle m_i^a| (U_i^a)^* - 1\right) \otimes \bigotimes_b \left(3V_i^b |n_i^b\rangle\langle n_i^b| (V_i^b)^\dagger - 1\right), \tag{2.24}$$

assuming the readout is in the computational basis as well as the random unitaries are on-site Haar random, $U_i = \prod_a U_i^a$ and $V_i = \prod_b V_i^b$. See Figure 2.3b for a graphical representation of the OpEE variant of the classical shadows protocol. Partial traces are done simply by neglecting the qubits that are traced out from the above tensor product. Note that similar protocols appeared in the literature as we were finishing our work [114, 115].

2.3 Verifiable Scrambling

In this section, I will present the results we obtained in our study of scrambling in programmable quantum simulators, demonstrated by measuring the OpEE

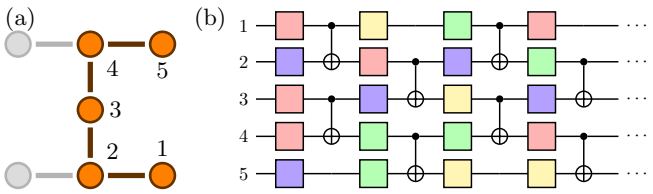

Figure 2.4: Figure and caption taken from our Paper [1]: (a) Qubit layout and connectivity of `ibm_lagos`. Dark purple circles represent the 5 qubits used for the experiments detailed in the main text. (b) Circuit design for the chaotic unitary $\mathcal{N}_t$, with $t = 4$ timesteps shown. Each single qubit gate (coloured boxes) is independently sampled from the four gates $W_{1,\ldots,4}$, see main text.

measures via our variant of Classical Shadows protocol, realised on an IBM Cloud quantum device [1].

Setup. The experiment was run on IBM's `ibm_lagos` 7−qubit device [116], see Figure 2.4 for qubit layout. The figure also shows the brickwork circuit that we used as the scrambler. The circuit was designed to use the native gates of the device, hence the coupler is always a CNOT gate, while the random one-qubit unitaries are taken from a discrete set of four gates $W_{1,\ldots,4}$. They are, in terms of native one qubit gates[8], $W_1 = R_{\pi/4}\sqrt{X}R_{-\pi/4}$, $W_2 = R_{\pi/4}XR_{-\pi/4}$, $W_3 = \sqrt{X}R_{\pi/4}\sqrt{X}$, and $W_4 = \sqrt{X}R_{-\pi/4}\sqrt{X}$, with $R_\theta = e^{-i\theta Z/2}$. Each timestep, $t = 1, 2, \ldots$, each qubit is subjected to one of the four gates, chosen independently and uniformly, then a layer of CNOT gates is applied, $(2j-1, 2j)$ at odd timesteps and $(2j, 2j+1)$ at even timesteps. The random unitaries indexed by timestep t and position j, $W_{c_{j,t}}$, are drawn once and used throughout the study, the only unitaries "averaged over" are the ones used in our version of Classical Shadow Tomography of OpEE. Hence, for a given total time/depth, t, we have a definite (ideally unitary) channel, $\mathcal{N}_t$.

Sampling. The sampling procedure we employed in this paper differs slightly from the one described in the previous section because of the nature IBM's Quantum Cloud queuing. It is fast to run multiple instances of the same circuit. Our one instance consists of a following setup:

[8] X and Z are the usual Pauli gates, and $\sqrt{X}$ is any of the two gates that square to X.

Classical Shadow Tomography modified for IBM's Quantum Cloud

1. The full circuit consists of M_S layers of our variant of Classical Shadows tomography for quantum channels:
   (a) Randomisation of bits: Apply Hadamard gates to all qubits and read out the results, $\{m_i\}$ as per the notation in the previous section,
   (b) Apply a layer of random unitaries, $\{U_i\}$,
   (c) Apply the brickwork circuit to be examined, $\mathcal{N}_t$,
   (d) Apply second layer of random unitaries, $\{V_i\}$,
   (e) Measure the bits in the computational basis, $\{n_i\}$.
2. Repeat the whole circuit M_U times.

For each layer in a single run, randomising unitaries and measurement outcomes are independently sampled, the ideal classic shadow tomography. In addition to the number of shots coming from M_S different layers, we also repeat the whole circuit M_U-times, in which case only the measurement outcomes are independently sampled, since the same random unitaries are used for tomography.

Tomography. This allows us to generate more shots, in total $M_S M_U$. However, care is needed when constructing the estimators for the doubled density matrix needed to calculate the second Rényi entropy. To avoid bias induced by repeating the unitaries, we simply expand the equivalence:

$$\hat{\rho}_2 = \frac{1}{M_S M_U M_U (M_S - 1)} \sum_{i \not\equiv j} \hat{\rho}_i \otimes \hat{\rho}_j, \tag{2.25}$$

where the new equivalence, $i \equiv j$, associates shots in different runs that are at the same depth within the run; i.e. those that use the same randomising unitaries, $\{U_i\}$ and $\{V_i\}$.

Randomising Unitaries. The randomising unitaries are also uniformly sampled from a discrete set, $U_i, V_i \in \{\mathbb{I}, H_X, H_Y, X, H_X X, H_Y X\}$, where H_X and H_Y are the Z to X and Y basis change (Hadamard) gates, respectively. Given that the input and output states are also generically uniformly sampled upon randomisation and final measurement, one can also just use the first half of the aforementioned

discrete set, $\{\mathbb{I}, H_X, H_Y\}$. This ensemble is sufficiently random to result in the same unbiased estimator as the full Haar radnom ensemble.

Number of Runs. The full shadow tomography protocol was executed on `ibm_lagos` with $M_S = 8192$ and $M_U = 900$, for times varying from $t = 0$ to $t = 15$. The values obtained from this dataset are affected by both the noise of the device and the sampling error (statistical fluctuations). To isolate the effect of statistical fluctuations, the ideal version of the circuit was also simulated. The two datasets are labelled as 'simulation' and '`ibm_lagos`' in the following figures. The readout error of the device was mitigated by the methods described in Ref. [117], the error in the single qubit randomising gates, U_i and V_i, was not mitigated, even though it is possible [118], since the error is not expected to be significant, `ibm_lagos` can perform single qubit gates with an error of the order of 10^{-4}.

Quantities Measured: *Tripartite OpEE.* The main OpEE measure that we used in this study is the second Rényi mutual information $I^{(2)}(A : BC)$. As explained in Section 2.1.1, when this quantity is greater than $|A|$ we are able, in the Hayden-Preskill manner, to recover the quantum information in the subregion A, and if that is the case for any choice of region C, as long as $|C| \geq |A|$, we can say that the information is scrambled by the channel $\mathcal{N}_t$[38]. This criterion was used to determine that the scrambling happened in our circuit. This condition is robust to noise, since the inequality is a sufficient condition, while, e.g. the decay of the bipartite mutual information, $I(A : C)$ for any choice of small $|C|$, is a necessary condition (easily mimicked by noise) that the information was scrambled.

Entanglement Negativity. Another measure we will use is the entanglement negativity, a proper entanglement monotone that is a usual measure of entanglement in a mixed state[119]. We consider it because if $\mathcal{N}_t$ is non-unitary the state dual will be mixed. It is necessary to introduce this measure because the usual entanglement entropy cannot distinguish between the *mixedness* of the reduced density matrix due to entanglement or due to the inherent *mixedness* of the full density matrix. The entanglement negativity is, in fact, a measure of separability of the full density

matrix. Our particular negativity is defined in terms of the moments of the partially transposed density matrix

$$p_{m,X:Y} := \mathrm{Tr}\left[\left(\rho^{XY}(t)^{T_X}\right)^m\right] \tag{2.26}$$

where T_X denotes the partial transpose with respect to dofs in the region X, and $\rho^{XY}(t)$ is the reduced density matrix of the region XY, time t reminds us that we are dealing with the state dual to the time evolution unitary. If the state is separable, the partial transpose will result in another proper density matrix $(\sum_i p_i \rho_i^X \otimes \rho_i^Y)^{T_X} = \sum_i p_i (\rho_i^X)^T \otimes \rho_i^Y$, it will remain positive definite[9]. However, if we see that partial transpose has some negative eigenvalues (sufficient but not necessary condition) the state has entanglement between the regions X and Y . The regions considered in this part remained the same, A and BC.

The quantity we tomographed was

$$R_{A:BC} := \frac{p_{2,A:BC}^2}{p_{3,A:BC}} \tag{2.27}$$

which can only exceed unity if the partial transpose has some negative eigenvalues[120]. Furthermore, we have argued, along the same line as presented in Section 2.1.1 , that this condition is a sufficient condition for the quantum communication capacity of the channel $\mathcal{N}_t^{A\to B'C}$ (see Figure 2.1b) to be non-zero, for $|A| = 1$; since the positivity (lack thereof) of the partial transpose is also a *distillation criterion*[92], the Peres criterion[121].

Operator spreading. Lastly, we also looked at the operator spreading coefficients. We may define a Pauli transfer matrix as follows:

$$c^{\mu\nu}(t) = \mathrm{Tr}\left(\boldsymbol{\sigma}^\nu \mathcal{N}_t^\dagger[\boldsymbol{\sigma}^\mu]\right), \tag{2.28}$$

where $\boldsymbol{\sigma}^\alpha$ is a Pauli string, an operator that is a tensor product of Pauli operators (identity included) over the qubits of the system, it is labelled by $\alpha \in \{I, x, y, z\}^{\times N}$. These coefficients, $c^{\mu\nu}(t)$ are just the expansion coefficients of the time evolved

[9] T is the usual matrix transpose.

Pauli string, $\boldsymbol{\sigma}^{\mu}(t)$ in the basis of Pauli strings. Trivially, we see that our (bipartite) operator state purity, eq. (2.13), becomes:

$$2^{-S^{(2)}(AC)} = \frac{1}{2^{|A|+|C|}} \sum_{\nu \in A, \mu \in C} |c^{\mu\nu}(t)|^2, \tag{2.29}$$

where $\alpha \in X$ means the strings acts trivially on all sites outside of region X. We can now define a measure of k-locality of $\boldsymbol{\sigma}^{\mu}(t)$ as

$$D_k^{\mu}(t) := \sum_{\nu:|\nu|=k} |c^{\mu\nu}(t)|^2, \tag{2.30}$$

where $|\nu|$ counts the number of non-identity operators in the string. Upon averaging over all non-zero strings, in say region C,

$$D_k^{C}(t) := \frac{1}{4^{|C|}-1} \sum_{\mu \in C} D_k^{\mu}(t), \tag{2.31}$$

we get the last quantity we measured in our experiment, $D_k^C(t)$, which measures how operators localised in region C grow in complexity.

All of the above quantities are functions of an integer power of the operator state density matrix $I^{(2)}(A:BC) = \mathcal{O}(\rho(t)^2)$, $p_{2,A:BC}^2 = \mathcal{O}(\rho(t)^4)$, $p_{3,A:BC} = \mathcal{O}(\rho(t)^3)$, and $|c^{\mu\nu}(t)|^2 = \mathcal{O}(\rho(t)^2)$, hence they can be straightforwardly estimated via our variant of the Classical Shadow Tomography of quantum channels.

Summary of Results. The Rényi mutual information, $I^{(2)}(A:BC)$, is shown in Figure 2.5a. The regions A and C are both single qubits indexed by j_A and j_C, with $j_A = 1$ fixed and j_C varying, see Figure 2.4(a) for the full qubit layout. At early times, the OpEE measure is above the distillation criterion only for $j_C = 1$, at late times the simulated value for all j_C approach $I^* \approx 1.1945$, which is the average value if we take our circuit to be a Haar random unitary on 5-qubits, the information is successfully scrambled (for $j_C = 5$ this value is reached for times just a bit later than the plotted range). The approach to this value is governed by the causal light cone, for a lower j_C the value is reached earlier. The device data is consistent with the simulation at early times. At late times, $I^{(2)}(A:BC)$ for all j_C decays due to device noise (which lowers the fidelity of the information transmission). For $j_C \leq 3$ the measured OpEE reached above the distillation (recoverability) criterion. Even

though not all j_C reach the threshold due to noise, the rise in the OpEE is a clear indicator of information spreading to all qubits of the system.

The ratio of negativities, $R_{A:BC}$, is shown in Figure 2.5b. The behaviour is similar to the OpEE, initially it is only large for $j_C = 1$, and at late times the value for all j_C approaches the same limiting value, obeying the same causal light-cone behaviour. In the simulation, the threshold is reached sooner than in the OpEE case, suggesting that this value offers a more sensitive criterion (remembering that these are all sufficient conditions) for the information scrambling. However, the device data show a larger suppression of the signal due to noise, suggesting a higher sensitivity to noise.

Lastly, the operator spreading, captured by the cumulative sum $\sum_{l=0}^{k} D_l^C$, is shown in Figure 2.5c. Here we have fixed $j_C = 3$, C is in the middle of the chain. Unitarity requires that the cumulative sum is equal to 1, which the simulated data is consistent with. At early times, the operator weight is concentrated in the low-weight, low k, sector, and as time progresses, the weight increased as the local operator develops larger support (causal structure is still visible in the data). After the full scrambling time, the weight is well approximated by

$$D_k^C = \frac{3^k \binom{N}{k}}{4^N - 1},$$

which is consistent with the uniform spread of the operator throughout the operator space. The device data shows a decrease in all the weights, due to noise, as can be interpreted as the operator spreading to inaccessible environment degrees of freedom.

Conclusions. Without doubling the number of qubits, we have estimated many relevant scrambling measures (most notably the tripartite OpEE) that verify the fact that the initially local quantum information was indeed delocalised and scrambled by our circuits.

2.4 Transport in Long Qubit Arrays

As mentioned in previous sections, the value of bipartite mutual information can decay as not only the consequence of unitary evolution, but also due to the presence of noise. That is, it does not differentiate between the two. However, the low

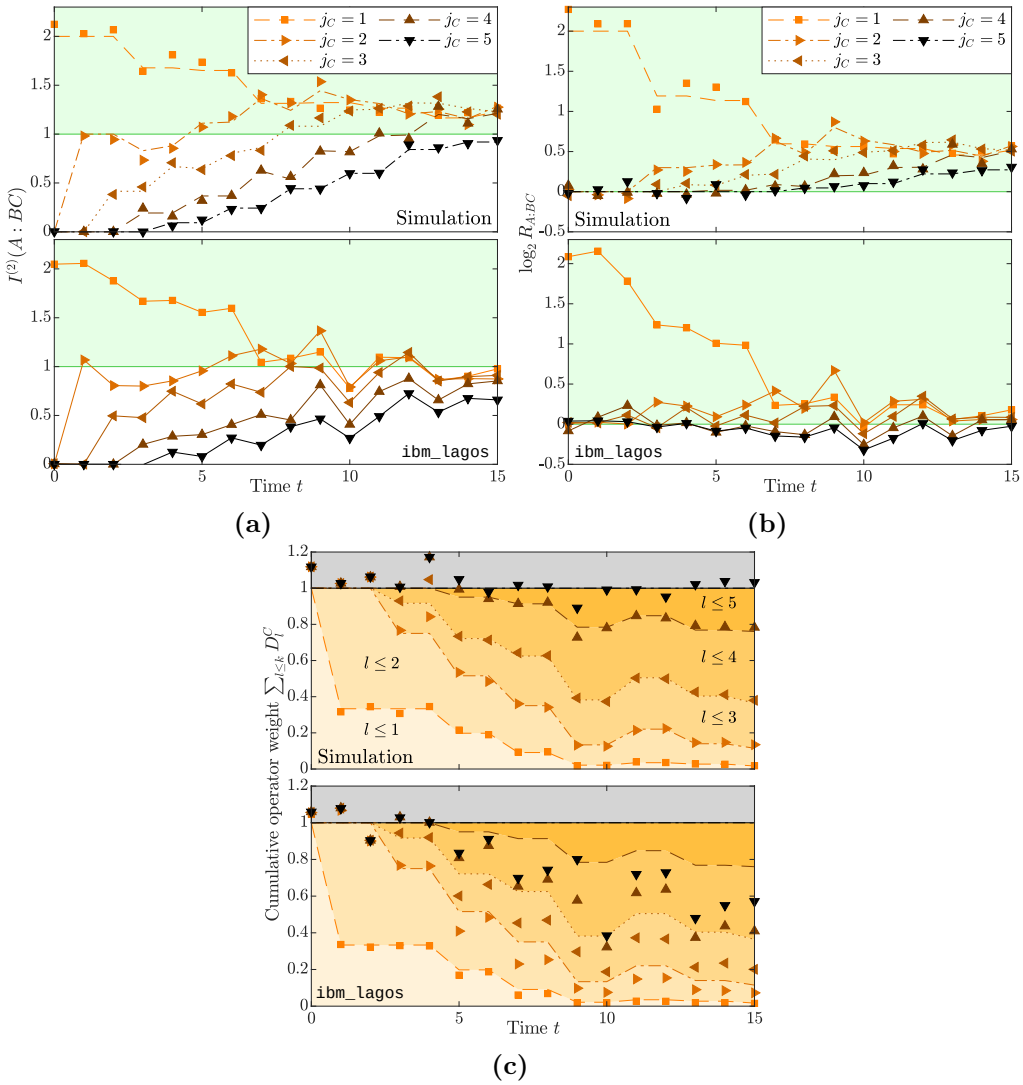

Figure 2.5: Figures taken and captions adapted from our Paper, Ref. [1]. (a) Rényi mutual information [Eq. (2.4) with $I^{(2)}(A:BC)$], with $A = \{1\}$, $C = \{j_C\}$. Top panel: Dashed lines indicate the exact value without noise or sampling error, points are estimations obtained using shadow post-processing methods on data from numerical simulations of the full circuit (Fig. 2.4) without noise. The deviations between these two values can be used to estimate the typical size of the sampling errors that arise from the shadow tomography protocol. Bottom panel: results obtained from `ibm_lagos`; solid lines are to guide the eye. The region above the threshold $I^{(2)}(A:BC) > 1$, is shaded green (see Section 2.1.1). (b) Logarithm of the ratio $R_{A:BC} = p^2_{2,A:BC}/p_{3,A:BC}$, where $A = \{1\}$, $C = \{j_C\}$. Data presented as in Fig. 2.5a. The region above the threshold $\log R_{A:BC} > 0$ is shaded green (see the main text and Section 2.1.1). (c) Evolution of the k-locality of time-evolved operators, as quantified by D_k^C [Eq. (2.31)]. Specifically, we plot the cumulative weight $\sum_{l\leq k} D_l^C$ which measures the total weight of the time-evolved operator acting non-trivially on at most k qubits, averaged over all non-trivial initial operators with support on C. We fix $C = \{3\}$, the central qubit in Fig. 2.4(a). The shaded areas and dashed lines indicate the exact values without sampling error or noise. Markers indicate shadow tomographic estimates calculated from the datasets obtained from noise-free simulations (top) and from the quantum device (bottom). The former are affected by sampling error only, while the latter are affected by both sampling error and noise.

number of shots required to estimate it via the modified classical shadows protocol still makes it a good quantity to probe in quantum simulators.

If we assume that the noise is negligible up to the times we are evolving, we can estimate the bipartite mutual information, hence study the transport properties of the time evolution operator, i.e. uncovering the long-lived modes. Note that this quantity, $I(A:C)$ as we define it, is related to the classical information carried by a channel from region A to region C [122, 123]. This classical information transport picture is suggestive of the fact that hydrodynamical transport of certain local densities in a quantum system is a semiclassical portion of the full quantum mechanical time evolution. Later, I will show some examples on a range of systems, some integrable and some chaotic, to illustrate this fact.

This approach is, as mentioned, initial-state agnostic, but it is also agnostic to the exact local density. It only reveals the presence of local conserved densities and their late-time dynamics, leading order by leading order.

The usual way to study transport in both experimental [124] and numerical studies [125] is to look at the melting of a domain wall. The initial state is one of imbalance; the left half has a large positive uniform density of the local conserved charge, while the right half has the opposite. As the system evolves, the domain wall between the halves relaxes via the transport of said density, with the derivative of the density profile in space being related to the density-density autocorrelation function.

To understand the reason for this approach in numerics, we need to look at the domain wall state:

$$\rho(t=0) \propto \bigotimes_{i<0}(\mathbb{I}+\lambda q_i) \otimes \bigotimes_{i\geq 0}(\mathbb{I}-\lambda q_i), \tag{2.32}$$

the small parameter, λ, is tunable and q_i's are the local conserved charge operators.

The density matrix of the initial state is of low bond dimension, a product state. The final state is also a product state, an infinite-temperature state. The two states are close in an operator norm sense, hence it is a good intuition that the path the time evolved state takes between the two endpoints will not take it outside the low-bond-dimension subspace of density matrices. This is the reason why numerical

studies take this approach. It is a bit less obvious why the experimentalists use this approach, given that they can directly access the infinite-temperature autocorrelation function [126]. Note that in the experiment, the domain wall was highly polarised, i.e., close to a pure state, with λ being close to 1.

It is not clear how to proceed with this setup if, for example, the local density is not that local or is not accessible to the experimentalists, in terms of both initial domain-wall state preparation or measurements of said local density profile in time. What I argue is that by measuring the bipartite mutual information with our variant of the classical shadows protocol, we can infer the transport class (diffusive, ballistic etc.) and transport parameters without the need to access the local density itself. In systems whose dynamics is not known, this measurement can also reveal the presence of local conservation laws, long-lived modes, and whether the system admits a hydrodynamical or a quasi-particle description.

The Model. The model I will study to showcase the descriptive power of bipartite operator mutual information is a well known nearest-neighbour Heisenberg model on a one-dimensional spin-1/2 chain with open boundary conditions in presence of an external field. The Hamiltonian is:

$$H = \sum_{i=1}^{N} \sum_{\alpha=\{x,y,z\}} \left(J_{\alpha\alpha} \sigma_i^\alpha \sigma_{i+1}^\alpha + h_\alpha \sigma_i^\alpha \right), \tag{2.33}$$

where σ_i^α are the Pauli matrices, $J_{\alpha\alpha}$ are the nearest neighbour coupling constants and h_α are the external field strengths. By varying these parameters, we can access a plethora of different phenomenologies, from free fermions to Bethe ansatz solvable models to chaotic systems.

Exact Results and Quasiparticle Picture. In the next section I will start with the solvable limit of our model, the Transverse Field Ising Model (TFIM):

$$H = -J_{xx} \sum_{i=1}^{N} \sigma_i^x \sigma_{i+1}^x - h_z \sum_{i=1}^{N} \sigma_i^z, \tag{2.34}$$

since in addition to the numerics we can also extract exact results for the bipartite mutual information.

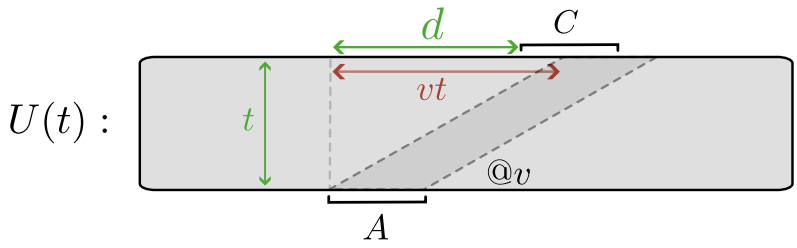

Figure 2.6: Graphical representation of the quasiparticle picture for calculating the bipartite mutual information. Each quasiparticle mode moving at a velocity v contributes to the bipartite mutual information by a quantity proportional to the overlap of the region C with the region A_t which is the region A translated by the said velocity.

This model is free fermion solvable and extracting the OpEE measures analytically is straightforward, see Appendix 2.A for the full calculation, accompanied by a phenomenological picture in terms of elementary quasiparticles carrying the bipartite information between the regions A and C, a la Calabrese-Cardy [20], see Figure 2.6.

I will not present the main result of the free-fermion calculation here, but I will use it as a benchmark for the numerics in the next section.

2.4.1 Matrix Product State (MPS) Numerics

To go beyond our exact and phenomenological results, I employed a variation of a Time-Evolving Block Decimation (TEBD) algorithm [127] to numerically evaluate the bipartite mutual information. This variation was previously used to numerically evaluate Out-of-Time-Ordered Correlators (OTOCs) in Ref. [128]. The definition of the OTOC is:

$$\mathrm{OTOC}_{A:C}(t) = \frac{1}{4^{|A|+|C|}} \sum_{O_A, O_C} \mathrm{Tr} O_A(t) O_B O_A(t) O_B. \tag{2.35}$$

The main idea of the algorithm, and how it avoids the late time entanglement barrier, is that it focusses on evaluating the time evolved local operators (working in Heisenberg picture), e.g. $O_A(t)$, rather than evolving quantum states.

The algorithm is simple:

Modified TEBD Algorithm for calculating OpEE I

1. Start with the state dual to O_A, $|O_A\rangle$.
2. Evolve the state with $U(t) \otimes U^*(t)$ via the usual TEBD algorithm.
3. Evaluate the overlap with the state dual to O_C, $\langle O_C| U(t) \otimes U^*(t) |O_A\rangle$.
4. Average the modulus square of the overlap over O_A and O_C to get the logarithm of operator state purity, the exponential of the bipartite mutual information.

For a given bond dimension, χ[10], the relevant overlap, $\langle O_C| U(t) \otimes U^*(t) |O_A\rangle$, can be evaluated without worrying about the truncation error for a specific set of qubits supporting O_C with respect to the position of O_A, see Figure 2.7b for a graphical representation of this fact. That is, if O_C is supported near the edge of the Lieb-Robinson cone of O_A, the effects of the truncation error will be small [128].

This is because the bond dimension of the state dual to $O(t)$ for a given cut will grow exponentially slowly if that cut is outside the Lieb-Robinson light cone, a consequence of the Lieb-Robinson bound[129]. Increasing the bond-dimension cutoff will allow us to peer deeper into the region's A light cone, but the absolute time of the evolution is not a relevant factor in the correctness of my numerics.

Interestingly enough, what Xu and Swingle found in Ref. [128] is that for OTOCs one can peer deep into the light cone while still getting what they claim are sensible results. For my measure, which is closely related to the OTOC, see Figure 2.7c, this is not what I observe.

One technical note, I have done the average of the operators in region C explicitly, to avoid some unnecessary numerical computations:

$$\sum_{O_A,O_C} \langle O_A| U^\dagger(t) \otimes U^T(t) |O_C\rangle \langle O_C| U(t) \otimes U^*(t) |O_A\rangle = \sum_{O_A} \langle O_A| U^\dagger(t) \otimes U^T(t) P_{\bar{C}} U(t) \otimes U^*(t) |O_A\rangle = \sum_{O_A} \langle O_A(t)| P_{\bar{C}} |O_A(t)\rangle , \quad (2.36)$$

[10]The main parameter governing the precision of all (variational) MPS based numerics; higher the bond dimension higher the precision (variational states are closer to real states), but also the time and memory requirements of a simulation. See Ref. [127] for a detailed review of MPS methods.

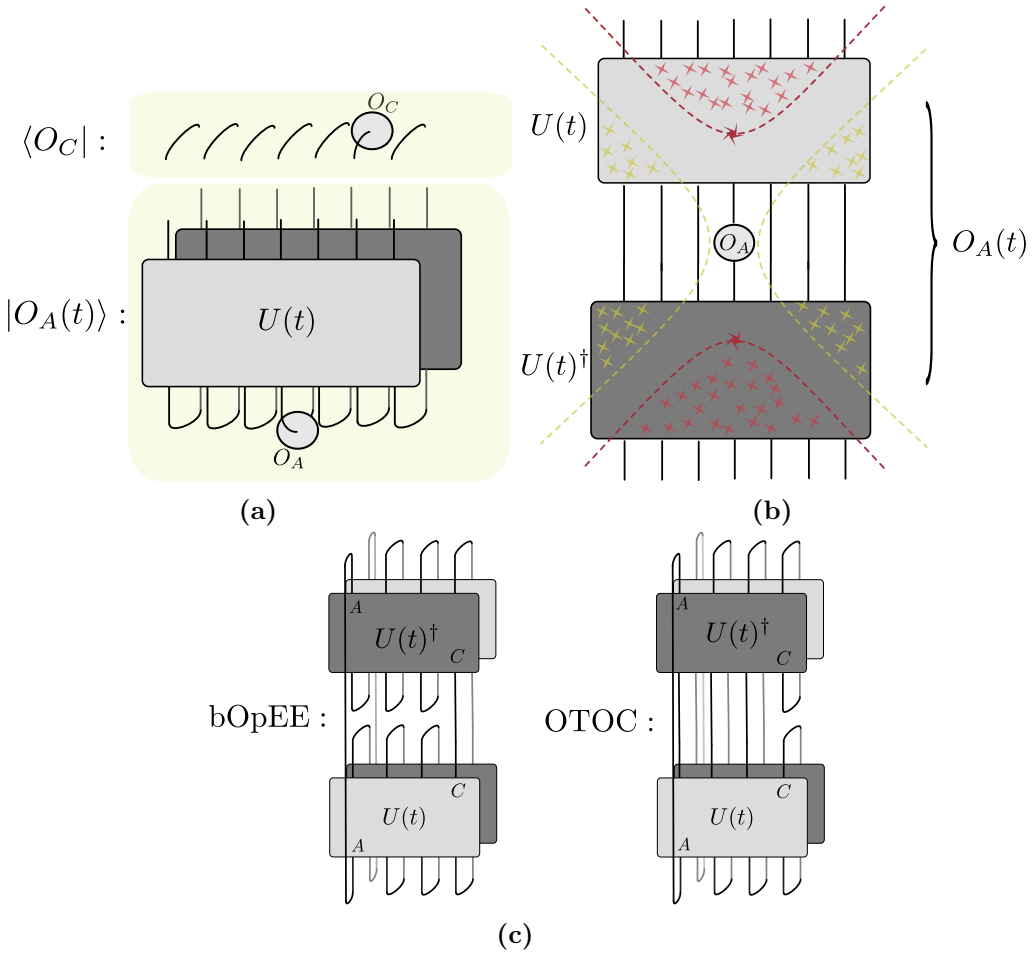

Figure 2.7: Tensor diagrams related to the modified TEBD algorithm used to calculate bipartite operator mutual information.
(a) Diagram of the overlap $\langle O_C|O_A(t)\rangle = \langle O_C|\, U(t) \otimes U^*(t)\, |O_A\rangle$.
(b) Unpacked tensor network diagram for the state $|O_A(t)\rangle$. Leveraging the unitarity of $U(t)$ we see that the state outside the Lieb-Robinson cone (yellow region) is still close to a product state of Bell pairs (due to cancelling effects of the forwards and backwards time evolutions), as well as the fact that the initial truncation error (red event) is also bound to spread as fast as the Lieb-Robinson velocity (only the red region is corrupted). The way TEBD is performed preserves the unitarity of the time evolution operator, even after truncation error is induced; hence the truncation error from the forward time evolution must cancel with the error from the backwards time evolution, $U^\dagger_{\text{error}}(t)U_{\text{error}}(t) = \mathbb{I}$. This will not happen in the case of evaluating $\langle O_C|O_A(t)\rangle$ if O_C is inserted inside the red region, because the O_C will interfere with the cancellation. Hence, between the yellow and red regions we can expect a non-zero bipartite OpEE that is well estimated by a low-bond dimension MPS numerics, and the size of this region increases with bond dimension by pushing the red region further into the future/past.
(c) A tensor contraction diagram representing our operator state purity (exp of bOpEE) compared to the tensor contraction diagram representing the average OTOC.

where the terms in the last sum, the expectation value of a certain projector $P_{\bar{C}}$, are evaluated via TEBD and then averaged over. The projector $P_{\bar{C}}$ projects the qubit pairs (remember that the system is doubled in this simulation) in the complement of region C (i.e. region D) to the Bell pair states, while doing nothing to the qubit pairs in region C, see the leg contractions in the middle of the diagram in Figure 2.7c.

Modified TEBD Algorithm for calculating OpEE II

1. Start with the state dual to O_A, $|O_A\rangle$.
2. Evolve the state with $U(t) \otimes U^*(t)$ via the usual TEBD algorithm.
3. Evaluate the expectation value of projector $P_{\bar{C}}$ in the state, $\langle O_A(t)| P_{\bar{C}} |O_A(t)\rangle$.
4. Average over O_A to get the exponential of the bipartite mutual information.

The OTOC has the same definition as the second half equation (2.36) just with $P_{\bar{C}}$ replaced by P_C, analogously defined.

A third variant of the algorithm can be worked out by also performing the explicit average over the operators in the region A, however, I have seen that that version requires a larger bond dimension to achieve the same level of convergence, due to another doubling of the on-site bond dimension.

2.4.2 Results of the Numerics

In this section, I will present the results of the numerics described in the previous section.

First, I will present the results of the MPS numerics compared to the free-fermion solution, see Figure 2.8a. As we can see, the MPS numerics of low bond dimension capture bOpEE perfectly everywhere, in addition to this, the convergence with respect to bond dimension is remarkable, $\chi = 4$, see Figure 2.8b for the convergence plots.

Mixed Field Ising Model (MFIM). Having ensured that our MPS numerics agrees with the exact free-fermion solution, I will move on to main results for this

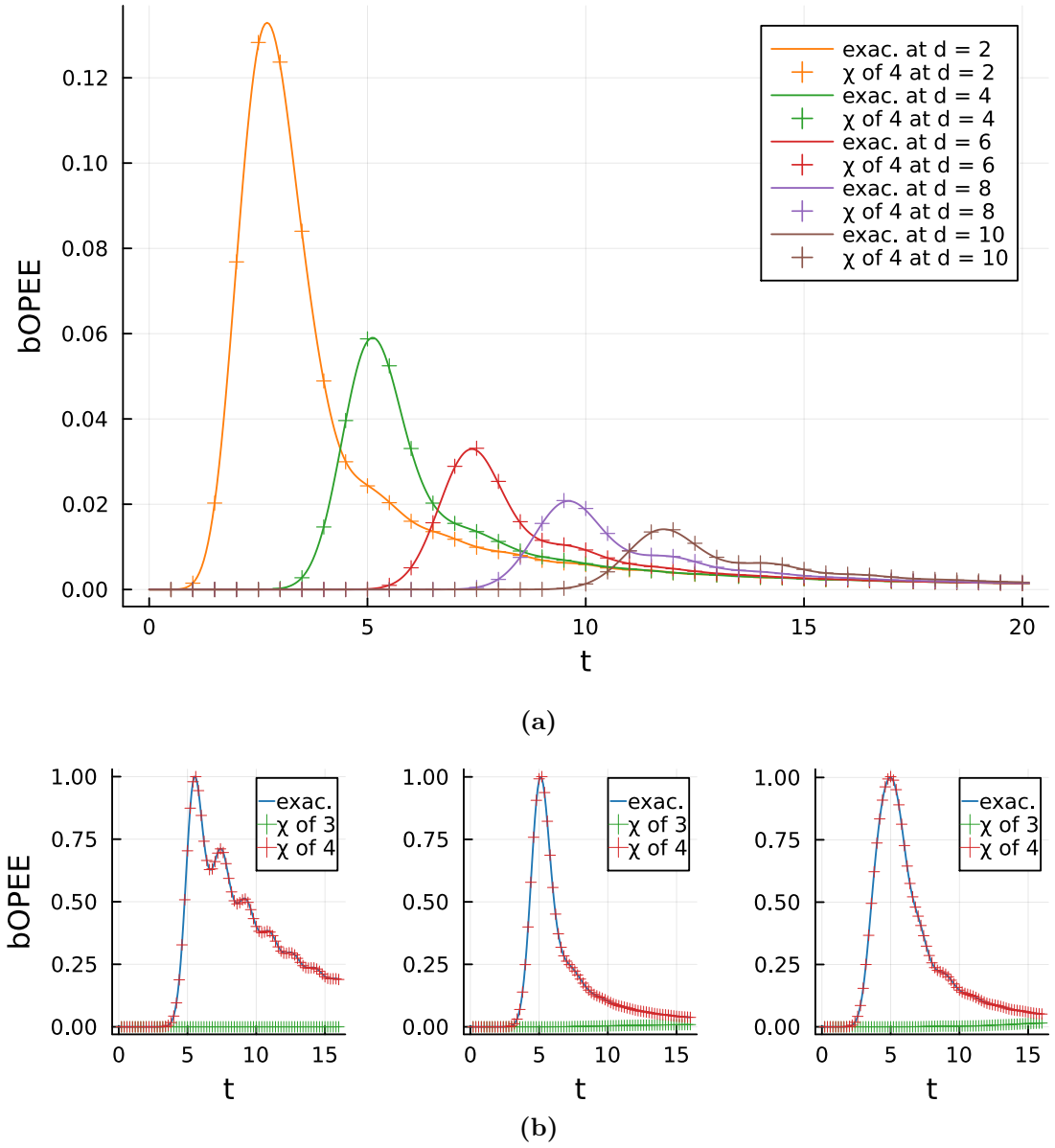

Figure 2.8: The MPS numerics versus the free-fermion solution in the case of TFIM. The numerical results are plotted with crosses over the exact solution in solid line:
(a) Comparison of the exact free fermion solution for the bipartite mutual information with the MPS numerics. The geometric parameters are $|A| = |C| = 2$, with TFIM at the critical point, $h_z = J_{xx} = 1$. The MPS numerics of low bond dimension, $\chi = 4$, captures OpEE perfectly everywhere. The bOpEE is normalised by the largest possible value bOpEE can take, $|A| + |C| = 4$. Time is measured in the units of the inverse of the coupling J_{xx}.
(b) Remarkable convergence of the MPS-based estimate of bOpEE. The geometric parameters are $|A| = |C| \in \{1, 2, 3\}$ from left to right, with TFIM at the critical point, $h_z = J_{xx} = 1$. The convergence is remarkable, with the bond dimension $\chi = 4$ capturing the bOpEE perfectly. The bOpEE is normalised by the largest value reached. Time is measured in the units of the inverse of the coupling J_{xx} and $d = 4$.

model, tuning away from integrability to the MFIM.

Figure 2.9a shows the results of the MPS numerics for the MFIM, the geometric parameters are $|A| = |C| = 2$, with the nearest-neighbour coupling $J_{xx} = 1$ and the external fields $(h_z, h_x) \in \{(1.0, 0.0), (0.9, 0.1), (0.9, 0.8)\}$. The main takeaway is that as we tune away from integrability, we see that there is a crossover time when the classical information (bOpEE, $I_2^{(2)}(A:C)$) stops being transmitted via quasiparticle modes and starts being carried by the diffusion of the local energy density.

We can infer that the diffusing charge is the local energy density because the system has no other symmetries other than time-translation. From such a measurement one can infer the heat diffusion constant of the system.

The convergence in the most chaotic case is showcased in Figure 2.9b.

XXZ Model. In the case of zero magnetic field and by turning on the other two nearest-neighbour couplings we get a Bethe-solvable model, the XXZ model,

$$H = -J \sum_j \left[\sigma_j^x \sigma_{j+1}^x + \sigma_j^y \sigma_{j+1}^y + (1+\Delta) \sigma_j^z \sigma_{j+1}^z \right], \tag{2.37}$$

where Δ is the anisotropy parameter. The results of the MPS numerics for this model in three different transport regimes, depending on the anisotropy parameter, are shown in Figure 2.9c.

The results are for three values of the anisotropy parameter, $\Delta \in \{-0.25, 0.0, 0.25\}$, corresponding to the three different spin transport regimes: ballistic, superdiffusive and diffusive, respectively. All three results are qualitatively indicative of two components contributing to bOpEE: a ballistic component coming from the energy density transport, since the system is integrable, with the added spin transport component changing from ballistic to diffusive as we increase the anisotropy parameter.

Even though, one could now look at the contours of equal bOpEE in order to extract the dynamical scaling exponents, I stress that this is not a computational tool; in order to access non-ballistic transport we need to look deep into the light cone, where my MPS numerics are not reliable. This is an approach tailored for programmable quantum simulators.

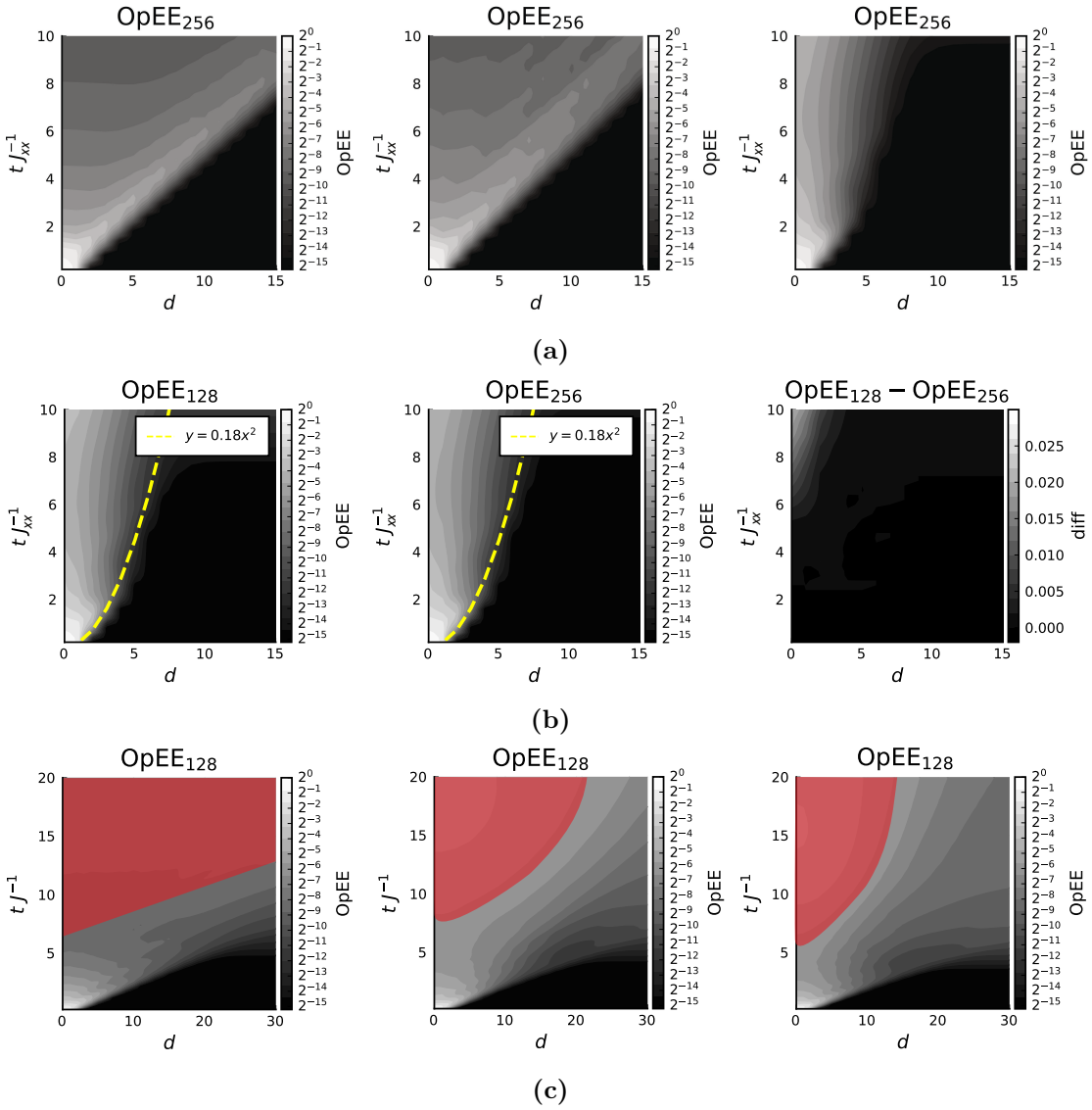

Figure 2.9: The results of the MPS numerics. The subscripts OpEE_χ, refer to bond dimensions $\chi \in \{128, 256\}$ of the simulation:
(a) MFIM: the geometric parameters are $|A| = |C| = 2$, with the nearest-neighbour coupling $J_{xx} = 1$ and the external fields $(h_z, h_x) \in \{(1.0, 0.0), (0.9, 0.1), (0.9, 0.8)\}$ from left to right.
(b) Convergence: the bond-dimensions are $\chi = 128$ and $\chi = 256$. External field is $(h_z, h_x) = (0.9, 0.8)$, i.e. the most chaotic case. Note the diffusive nature of the spread of bOpEE. To determine this fact quantitatively, one needs access to bOpEE deep in the light cone, where the numerics breaks down; hence the diffusive spread of the bOpEE is only a qualitative statement. The convergence properties are what we expect from Ref. [128], the error begins to develop at the origin and spreads no faster than the light cone.
(c) XXZ model: the geometrical parameters are $|A| = |C| = 2$, with the anisotropy parameter $\Delta \in \{-0.25, 0.0, 0.25\}$ from left to right. All three results are qualitatively indicative of two components contributing to bOpEE: a ballistic component coming from the energy density transport, since the system is integrable, with the added spin transport component changing from ballistic to diffusive as we increase the anisotropy parameter. The red areas represent regions where significant truncation error occured.

XX Model. Although there is no remarkable convergence in the case of the XXZ model in general, its free-fermion limit, $\Delta = -1$, the XX Model, does have that property. Hence, I would conjecture that the remarkable convergence of the low-bond-dimension MPS estimate of bOpEE is the property of free (fermion) theories.

Summary. Even though the question of remarkable convergence is still open and is of great interest, I would like to reiterate that the main point of the numerics was to showcase the physical significance of the bipartite operator mutual information, as the measure of the classical information transfer between regions in the input system and the output system, having already presented a protocol for measuring it in programmable quantum simulators with single-qubit control.

The measure is sensitive to the presence of quasiparticle modes and to hydrodynamical transport more generally, and it can be used to infer the presence of local conservation laws, and classes of transport, etc.

We also saw that this measure displays certain expected features in the integrable case, such as the peaks in the mutual information at the light cone, indicating when the fastest quasiparticles are arriving at the region C from the region A. This is visualised in Figure 2.6. The peaks also algebraically decay in time/distance which is also to be expected from the quasiparticle dispersion relation. The wave packets will disperse over time, making them less and less contained in the region C of fixed size.

Of course, we need to be careful at early times, due to the contributions from the non-conserved operator overlaps to the mutual information, eq. (2.13). One can follow up this work with a study of bOpEE in a Haar Random Unitary Circuit (i.e. with no conservation laws) to see what determines the decay of the mutual information in the fully chaotic case, see the Appendix 2.B for an example of this.

In our non-integrable cases, we said that the mutual information holds information about the diffusion of the local energy density, which would allow us to infer the heat diffusion constant of the system. Unlike the cases of spin transport measurements, this local density is not easily accessible to the experimentalists, i.e. one could not prepare a domain wall state and then directly observe the domain wall melting in an obvious manner.

Comment on Finite Temperature and Local Quenches. Given the Hamiltonian, H, that generates the time evolution operator, we can look at the following quantity:

$$2^{S^{(2)}_{OpEE}(AC,\,\beta)} = \sum_{O_A, O_C} |\mathrm{Tr} U(t)\sqrt{O_A}e^{-\beta H}\sqrt{O_A}U^\dagger(t)O_C|^2, \tag{2.38}$$

β is the inverse temperature. This is a finite-temperature generalisation of our bipartite OpEE; if we take $\beta \to 0$ limit, we retrieve our previous bipartite OpEE. Note, if we work in the Pauli string basis of O_As, operator $\sqrt{O_A}$, a local operator squaring to O_A, can be chosen to be simply a string of square roots of Pauli operators, e.g. $\sqrt{X_1 \otimes Z_2} = H_1 S_1 H_1 \otimes S_2$, where S is the Pauli phase gate, $S = \mathrm{diag}(1, i)$, and H is the Haddamard gate.

However, if we take the other limit, $\beta \to \infty$, we can regard the problem as a local quench above a (almost) ground state. In this regime, the object

$$U(t)\sqrt{O_A}e^{-\beta H}\sqrt{O_A}U^\dagger(t)$$

is a density matrix of a state at some time t after a local quench above a proper vacuum. Local quenches are perturbations that inject a small (non-extensive) energy into the system, and hence the state after such a quench is a simple object characterised by few elementary quasiparticles. This density matrix is a low-bond-dimension object[130].

At high temperatures, as in the case of bOpEE, this is no longer true, because the few injected quasiparticles interact with the high-temperature bath, a myriad of other quasiparticles if the system is integrable.

However, the description is still simple if the theory is free, as in the TFIM case where we saw remarkable convergence. The relevant quasiparticles that carry information from region A to region C do not interact with the bath, and the overlaps we care about are still captured by low-bond-dimension numerics; in contrast to the interacting case.

2.5 Chapter Summary

In this chapter, I have presented the work I have done on the topic of operator entanglement entropy measures. In particular, I have singled out two OpEE measures, $I_2^{(2)}(A:C)$ and $I_3^{(2)}(A:B:C)$, where the subsystems A and B are in the input of the quantum channel we want to characterise (a unitary circuit or a time evolution operator) and C is in the output. I have shown how we related the second measure to verifiable quantum information scrambling, and how the first related to the transport properties of a quantum system. I have also presented our variant of a classical shadow tomography modified to be used to characterise quantum channels.

This new method allows us to measure the entanglement properties of a state dual to a quantum channel without the need to double the quantum resources to represent it directly. These types of techniques also remove the need to prepare simultaneous copies of a state in order to measure nonlinear functions in the density matrix, such as the aforementioned entanglement entropies.

The method requires a number of shots that is exponential in the number of qubits in the system, in the case of tripartite OpEE, and exponential in the number of qubits in subsystems A and C, in the case of bipartite OpEE ($\mathcal{O}(1)$ in system size). Hence, when considering large qubit arrays, we can only access the bipartite OpEE measure, which has been shown to relate to the classical information transport properties of a quantum system, most notably the bounds it imposes on the transport of local conserved charges, which we can use to experimentally access the transport properties of quantum systems.

Our published work deals with verifying whether a given circuit run on an actual NISQ device has managed to verifyingly scramble local quantum information. To that end, we have used the methods we developed to, among other things, measure the tripartite OpEE and see if it exceeds thresholds that we relate to already existing criteria for quantum information scrambling. In addition to that, we have also measured a relevant entanglement negativity as well as operator spreading coefficients. Although noise in the device suppressed the signal below the threshold, meaning that we cannot reconstruct the full information initially

present in region A from just any region C in the output (a definition of verifiable scrambling), the overall increase in OpEE measures, as well as the negativity through the entire system, definitively suggests that the circuit has managed to scramble the information initially localised in A.

On the side of bipartite OpEE and transport, I have presented a set of analytical and numerical results in the case of the Heisenberg model in the external field in various regimes in order to argue for the relevance of this OpEE measure (which can also be estimated as per the methods we have presented). In particular, the data suggest a clear signal when the system is integrable, with bipartite mutual information between regions A and C peaking as the fastest quasiparticles reach between the two regions, with these peaks displaying algebraic (in time) broadening due to dispersion. In the thermalising case, we see that at late times bipartite OpEE measures show a diffusive behaviour, with the conserved transfer of the local energy density preventing its full decay. These methods allow experimentalists to probe this behaviour even though they have no direct access to the local energy density operator.

2.A Jordan-Wigner Solution

The model in eq (2.34) is free fermion solvable via the Jordan-Wigner transformation:

$$\sigma_j^z = i\gamma_j^{(1)}\gamma_j^{(2)}, \quad \sigma_j^x = \left(\prod_{k<j}(i\gamma_k^{(1)}\gamma_k^{(2)})\right)\gamma_j^{(1)}, \tag{2.39}$$

where $\gamma_j^{(1)}$ and $\gamma_j^{(2)}$ are the (real) Majorana fermion operators, two per site:

$$\{\gamma_j^{(\alpha)}, \gamma_j^{(\beta)}\} = 2\delta_{\alpha\beta}\delta_{jk}. \tag{2.40}$$

The Hamiltonian in the Majorana fermion basis is:

$$H = -\frac{i}{2}\sum_{j=1}^{N}\left(h_z\gamma_j^{(1)}\gamma_j^{(2)} + J_{xx}\gamma_j^{(2)}\gamma_{j+1}^{(1)}\right) = -\frac{i}{2}\Upsilon^T h\Upsilon, \tag{2.41}$$

where $\Upsilon = (\gamma_1^{(1)}, \ldots, \gamma_N^{(2)})^T$ is a vector of Majorana operators and h is a real antisymmetric matrix, representing the first quantised Hamiltonian.

The time evolution, given by this (free) quadratic (in Majorana fermions) Hamiltonian, maps single Majorana fermion operators into linear combination of single Majorana fermion operators, the "n-bodyness" of an operator is preserved:

$$\Upsilon(t) = \hat{U}(t)^\dagger \Upsilon \hat{U}(t) = L(t)\left[\Upsilon\right], \tag{2.42}$$

where the linear map, $2N$ by $2N$ complex matrix, $L(t)$, is defined by the first quantised Hamiltonian h, $L(t) = e^{-ht}$.

This also implies that the time evolution operator maps Gaussian states into Gaussian states:

$$\rho = \frac{e^{\Upsilon^T W \Upsilon/4}}{Z(W)} \xrightarrow{U(t)} \rho(t) = \frac{e^{\Upsilon^T W(t) \Upsilon/4}}{Z(W(t))}, \tag{2.43}$$

where W and $W(t) = L(t)^T W L(t)$ are some antisymmetric matrices that define the state and $Z(W) = e^{\Upsilon^T W \Upsilon/4}$ is the normalisation factor, partition function.

Our maximally entangled initial state between the system and its copy is a Gaussian state, hence we can solve for the bipartite mutual information via this machinery.

Namely, our initial state can be written as:

$$|\Psi(0)\rangle = \bigotimes_i \frac{1}{\sqrt{2}} \left(|0\rangle_i |1\rangle_{i'} + |1\rangle_i |0\rangle_{i'}\right) = \prod_i \frac{1}{\sqrt{2}} (\sigma_i^x + \sigma_{i'}^x) |0 \ldots 0\rangle , \tag{2.44}$$

where i goes over the sites of the system and i' over corresponding sites of the copy. This is not a unique choice for a maximally entangled state, but it is one that makes further calculations easier.

In order to continue with the JW transformation, we need to decide on the ordering of the sites of the system and its copy; we chose the following ordering:

$$(j_r^A, j_r^A - 1, \ldots, 1)_{S'}, (1, 2, \ldots, N)_S, (N, N-1, \ldots, j_r^A + 1), \tag{2.45}$$

where j_r^A is the rightmost site of the region A, see Figure 2.10 for a graphical representation of this ordering. The regions A and C include the sites between j_l^A and j_r^A inclusive and between j_l^C and j_r^C inclusive, respectively. In this language, the separation is $d = j_l^C - j_r^A$, region C is to the right of region A and is not overlapping, i.e. $j_l^A \leq j_r^A < j_l^C \leq j_r^C$.

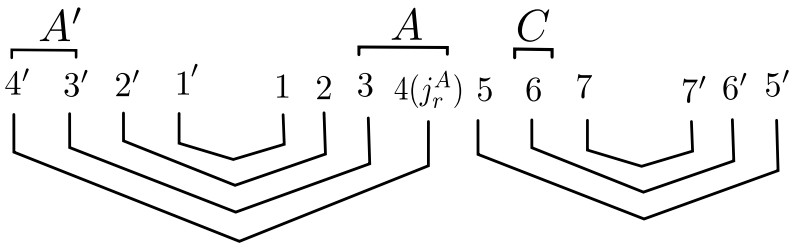

Figure 2.10: Graphical representation of the ordering of the sites of the system and its copy used in the JW transformation. In this example, the total number of sites in the system is $N = 7$, $|A| = 2$, $|C| = 1$, $d = 3$ and the region A ends with the site $j_r^A = 4$ ($j_l^A = 3$ and $j_l^C = j_r^C = 6$). I also show the entanglement structure of initial the state, i.e. what sites are in Bell pair states.

In terms of Majorana fermions, the initial state becomes:

$$|\Psi(0)\rangle = \frac{1}{2^{N/2}} \left[\prod_{k\leq j_r^A} [\gamma_{k'}^{(1)} + (-1)^{k+1}\gamma_k^{(1)}]\right] \left[\prod_{k>j_r^A} [\gamma_{k'}^{(1)} + (-1)^{N-k}\gamma_k^{(1)}]\right] |\text{VAC}\rangle$$
$$= \frac{1}{2^{N/2}} \prod_k [\gamma_{k'}^{(1)} + \nu_k \gamma_k^{(1)}] \, |\text{VAC}\rangle \,, \quad (2.46)$$

again, the primed and non-primed indices refer to corresponding sites of the copy and the original system. The ν_k coefficients come from commuting the parity strings, $\prod_{k<j}(i\gamma_k^{(1)}\gamma_k^{(2)})$, through the Majorana fermions further to the right in the product and annihilating the vacuum state defined as

$$i\gamma_k^{(1)}\gamma_k^{(2)} \, |\text{VAC}\rangle = |\text{VAC}\rangle \,,$$

for all sites k or k', i.e. just the z-polarised state $|0 \ldots 0\rangle$.

Only the original system is subject to the time evolution:

$$\gamma_k^\alpha \xrightarrow{U(t)} \sum_{l,\beta} L_{kl}^{\alpha\beta}(t)\gamma_l^\beta, \quad (2.47)$$

$$\gamma_{k'}^\alpha \xrightarrow{U(t)} \gamma_{k'}^\alpha, \quad (2.48)$$

which allows us to simply evolve the state with by evolving the Majorana fermion operators with unprimed indices.

Reduced Density Matrix. In order to calculate the bipartite mutual information, we need to calculate the reduced density matrix of the region $A'C$:

$$\rho_{A'C} = \text{Tr}_{B'D} \, |\Psi(t)\rangle \langle\Psi(t)| \,. \quad (2.49)$$

Now, we need to be careful; what was local in spins is no longer local in fermions. This is an issue because the region $A'C$ is not a contiguous region, however, Ref. [131] showed that the reduced spin density matrix is unitarily equivalent to a certain fermionic density matrix:

$$\rho_{A'C} = \frac{1}{2^{|A|+|C|}} \left[\sum_{O_{A'}, O_C \text{ even}} \langle O_{A'} O_C \rangle_t O_{A'}^\dagger O_C + \sum_{O_{A'}, O_C \text{ odd}} \langle O_{A'} P_M O_C \rangle_t O_{A'}^\dagger O_C \right], \tag{2.50}$$

where P_M is the Majorana parity operator on the region M between A' and C,

$$P_M = \prod_{j_r^{A'} < k < j_l^C} i \gamma_k^{(1)} \gamma_k^{(2)}.$$

The expectation value is taken in the state $|\Psi(t)\rangle$, the Hilbert Schmidt scalar product is a trace over the region $A'C$ which combined with the trace in the definition of the reduced density matrix gives the full expectation value. Noting again that the operators $O_{A'}$ and O_C are fermion local.

We can lift the time dependence from the state to the operators, $O_C \to O_C(t)$, work in the Heisenberg picture.

This is desirable given the simple structure of the initial state, i.e. if we trace out the copy completely, we get the maximally mixed state of the system. With that aim, we leverage another useful property of the initial state,

$$\gamma_{k'}^{(1,2)} |\Psi(0)\rangle = \pm i \nu_k \gamma_k^{(2,1)} |\Psi(0)\rangle ,$$

in order to cast operators supported on the copy into the operators supported on the original,

$$O_{A'} |\Psi(0)\rangle = \tilde{O}_A |\Psi(0)\rangle ,$$

tilde denoting the Majorana fermion swap defined at the top of the paragraph.

The coefficients in the operator basis expansion paired up with the odd parity terms, i.e. the appropriate expectation values, now read:

$$\begin{aligned} \langle O_{A'} P_M O_C \rangle_t &= \mathrm{Tr} \left(|\Psi(0)\rangle \langle \Psi(0)| O_{A'}(0) P_{L'}(0) P_R(t) O_C(t) \right) \\ &= \frac{1}{2^N} \mathrm{Tr} \left(\tilde{O}_A(0) \tilde{P}_L(0) P_R(t) O_C(t) \right) = 0, \end{aligned} \tag{2.51}$$

where we have used the fact that upon tracing the copy out, we are left with the maximally mixed state. In addition, the region M is split into regions L' supported on the copy and R supported on the original.

This is the infinite-temperature dynamical correlation function, between operators $O_A P_L$ and $P_R O_C$, the free fermion integrability of the model implies that the number of Majorana fermions in each operator is fixed by the time evolution and given the fact that if the regions do not overlap, the second operator will have strictly more Majorana fermions than the first, the correlation function will be zero.

Finally, the reduced density matrix in spins is equivalent to a fermionic density matrix of this form:

$$\rho_{A'C} = \frac{1}{2^{|A|+|C|}} \sum_{\substack{O_{A'} O_C \\ \text{even}}} \langle O_{A'}, O_C \rangle_t O^\dagger_{A'} O_C. \tag{2.52}$$

Operators in this sum, the Majorana parity even operators, are precisely those that are local in both spins and Majorana fermions.

Lastly, we need to cast this in terms of proper fermionic reduced density matrices,

$$\rho^f_{A'C} = \frac{1}{2^{|A|+|C|}} \sum_{\substack{O_{A'}, O_C \\ \text{even or odd}}} \langle O_{A'} O_C \rangle_t O^\dagger_{A'} O_C = \frac{e^{\Upsilon^T W_{A'C}(t) \Upsilon/4}}{Z(W_{A'C}(t))},$$

which will be that of Gaussian states. The subscript $A'C$ denotes the truncation of the full defining matrix, $W(t)$, to the $(2|A'| + 2|C|)$ by $(2|A'| + 2|C|)$ block corresponding to the Majorana fermions in the region $A'C$, another useful property of Gaussian states[131].

We can remove the odd term by summing two density matrices,

$$\rho_{A'C} = \frac{\rho^f_{A'C} + p_{A'} \rho^f_{A'C} p_{A'}}{2} = \frac{\rho^f_{A'C} + \bar{\rho}^f_{A'C}}{2}, \tag{2.53}$$

where $p_{A'}$ is the fermion parity operator on the region A'. In this sum the odd terms cancel out, thus, the reduced density matrix for the spins in region $A'C$ is given in terms of the sum of two fermionic Gaussian density matrices, defined by $W_{A'C}(t)$ and $\bar{W}_{A'C}(t) = p_A W_{A'C}(t) p_A$.

Gaussian Correlation Matrix. To finish off this calculation, we need to introduce one more object, the Gaussian correlation matrix

$$\Gamma_{mn}^{\alpha\beta} = i\left[\langle\gamma_m^\alpha\gamma_n^\beta\rangle - \delta_{mn}\delta^{\alpha\beta}\right], \tag{2.54}$$

here m and n go over all the sites in the two copies of the system, while α and β go over the two Majorana flavours. The matrix is evidently antisymmetric and is related to the defining antisymmetric matrix of the Gaussian state, W, via the relation [131]:

$$\Gamma = i\tanh(\frac{W}{2}). \tag{2.55}$$

For the initial Bell pair state, we directly verify that the only non-zero elements of the correlation matrix are:

$$\Gamma_{k'k}^{(1)(2)} = -\Gamma_{k'k}^{(2)(1)} = \Gamma_{kk'}^{(1)(2)} = -\Gamma_{kk'}^{(2)(1)} = -\nu_k, \tag{2.56}$$

for k only going over the original system sites.

The time evolution of these elements is given by the linear map $L(t)$ as

$$\Gamma_{k'j}^{(1,2),\beta}(t) = \pm\nu_k[L(t)^T]_{kj}^{(2,1),\beta}, \text{ for } \beta = \{(1),(2)\}. \tag{2.57}$$

Reduction to the subsystem $A'C$, getting $\Gamma_{A'C}$, is done by taking the $(2|A'|+2|C|)$ by $(2|A'|+2|C|)$ block of the correlation matrix, same as for the Gaussian state's defining matrix W.

The action of the parity operation on the copy of the system on the initial correlation matrix is simple, given the only non-zero terms pair one Majorana from the copy with one from the original, $\Gamma(0)$ is odd under this operation. Moreover, since $U(t)$ is trivial on Majorana fermions in the copy of the system, it commutes with the parity operator. These two facts imply $p_{S'}\Gamma(t)p_{S'} = -\Gamma(t)$ and, via eq.(2.55), $\bar{W}(t) = p_{S'}W(t)p_{S'} = -W(t)$, for all times t. The same holds, naturally, for the blocks after truncation.

The reduced density matrix of the spins in the region $A'C$ is then given by:

$$\rho_{A'C} = \frac{e^{\Upsilon^T W_{A'C}(t)\Upsilon/4} + e^{-\Upsilon^T W_{A'C}(t)\Upsilon/4}}{2Z(W_{A'C}(t))}, \tag{2.58}$$

using $Z(W) = Z(-W)$. The purity now reads:

$$\mathrm{Tr}\rho^2_{A'C} = \frac{1}{2}\frac{2^{|A|+|C|} + Z(2W_{A'C}(t))}{Z(W_{A'C}(t))^2}, \tag{2.59}$$

Finishing off this calculation is the standard results [131] for the partition function of a Gaussian state in terms of its defining (and also correlation) matrix:

$$Z(W) = \prod_{\lambda>0} 2\cosh(\lambda/2), \tag{2.60}$$

noting that eigenvalues of W appear in pairs, $\pm\lambda$. Square rooting the determinate of the squared matrix takes care of this bookkeeping.

The correlation matrix, Γ, according to eq.(2.55), has eigenvalues $\pm i\tanh(\lambda/2)$, which alongside some hyperbolic trigonometry identities, gives us the final result for the purity:

$$\mathrm{Tr}\rho^2_{A'C} = \frac{1}{2}\left[\frac{2^{|A|+|C|}}{Z(W_{A'C}(t))^2} + \frac{Z(2W_{A'C}(t))}{Z(W_{A'C}(t))^2}\right] = \frac{1}{2}\left[\sqrt{\left|\frac{1+\Gamma^2_{A'C}(t)}{2}\right|} + \sqrt{\left|\frac{1-\Gamma^2_{A'C}(t)}{2}\right|}\right], \tag{2.61}$$

where $|M|$ is the determinant of the matrix M and $\Gamma_{A'C}(t)$ is the truncated time evolved correlation matrix, given by eq.(2.57).

We just need to cast this expression in terms of the time evolution map, $L(t)$, which is done by noting that a similarity transformation $\tilde{\Gamma}_{A'C}(t) = \Lambda\Gamma_{A'C}(t)\Lambda^T$, where

$$\Lambda = \left[\bigoplus_{j\in A'} i\nu_k\sigma_y\right] \oplus I_{2|C|},$$

puts the correlation matrix into a very convenient form

$$\tilde{\Gamma}_{A'C}(t) = \begin{pmatrix} 0 & -L_{AC}(t) \\ L^T_{AC}(t) & 0 \end{pmatrix}, \tag{2.62}$$

where $L_{AC}(t)$ is a $2|A|$ by $2|C|$ matrix obtained by truncation of the time evolution map $L(t)$ to rows corresponding to region A and columns corresponding to region C.

The matrix $\tilde{\Gamma}^2_{A'C}(t)$ is diagonal block, and hence the expression for the purity becomes[11]:

$$\mathrm{Tr}\rho^2_{A'C} = \frac{1}{2^{|A|+|C|}}\frac{|I_{2|A|}+M| + |I_{2|A|}-M|}{2}, \tag{2.63}$$

[11]It is noteworthy how classical this result looks like. Namely, the sign structure of the initial state, ν_k, does not factor in.

where $M = L_{AC}(t)L_{AC}^T(t)$.

Results. One could make further analytical progress by diagonalising the first quantised Hamiltonian, h, but this is not necessary since we can easily exponentiate it to obtain the time evolution map, $L(t)$, and hence the correlation matrix, $\Gamma(t)$.

XX Model The exact solution in the free limit of the XXZ model, $\Delta = -1$, is obtained from eq. (2.63) results just by setting h to be that of the XX model after Jordan Wigner transformation

$$H = -\frac{i}{2}\sum_{j=1}^{N}\left(\gamma_j^{(2)}\gamma_j^{(1)} - \gamma_j^{(1)}\gamma_j^{(2)}\right) = -\frac{i}{2}\Upsilon^T h_{XX}\Upsilon, \tag{2.64}$$

since it is a general result for free fermion models.

2.A.1 Phenomenological Picture

A very simple but powerful phenomenological approach to entanglement dynamics in integrable systems was proposed by Calabrese and Cardy in Ref. [20], the famous quasiparticle picture.

This approach was originally used in the study of entanglement developlment follwoing a quench from a model whose ground state is of low entanglement to an integrable model. In the new model the initial state can be characterised by a finite density of quasiparticle pairs which upon time evolution spread out, always remaining entangled with each other.

In our problem, we are interested in entanglement between two regions separated in time. The appropriate quasiparticle approach looks at the quasiparticles that connect the region A to a future region C. This applies in the scaling limit, $|A|, |C|, d, t \gg 1$, for simplicity I will take $|A| = |C|$.

With that setup in mind, we look at a given quasiparticle mode travelling with some velocity v. That motion translated region A to region A_t whose overlap with region C is $(|C| - \min(|C|, |d - vt|))$ which is proportional to the contribution of that mode to the bipartite mutual information, see Figure 2.6.

Taking into account all the modes we get:

$$S_{A'C} = \int_{v_{min}}^{v_{max}} dv \min(|C|, |d - vt|) \left|\frac{\partial^2 \epsilon}{\partial q^2}\right|^{-1} s(v), \tag{2.65}$$

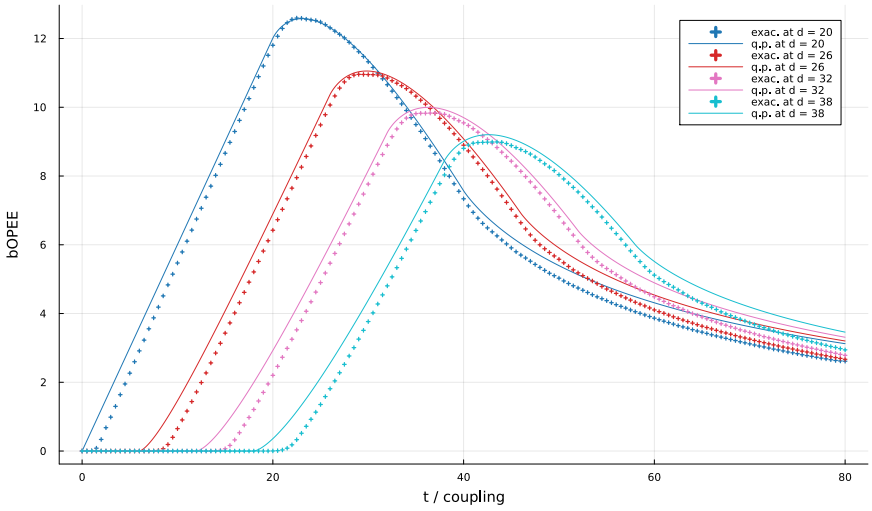

Figure 2.11: Comparison of the exact free fermion solution for the bipartite mutual information with the quasiparticle picture in the scaling limit. The Quasiparticle result is plotted in solid lines and is scaled down by a factor of 1.06, to better match the exact solution plotted in crosses. The layout parameters were, $|A| = |C| = 20$, with TFIM at the critical point, $h_z = J_{xx} = 1$. The Quasiparticle solution captures the early to late time crossover, but fails to capture late time behaivour.

assuming we only have one mode with a dispersion relation $\epsilon(q)$, the partial derivative part is proportional to the density of state at a given group velocity, while $s(v)$ is the entropy density carried by each mode, assumed to be a constant and fixed by the fully mixed condition, $S_{A'C} = |A| + |C|$ if e.g. $t = 0$ and $d > N_C$, no classical communication could have occurred:

$$\int_{v_{min}}^{v_{max}} dv \left| \frac{\partial^2 \epsilon}{\partial q^2} \right|^{-1} s_0 = 2|C|. \tag{2.66}$$

In the case of the critical TFIM, $\epsilon(q) \propto |\sin(q)|$, we get:

$$S_{A'C} = \frac{4}{\pi} \int_0^1 \frac{dv}{\sqrt{1-v^2}} \min(|C|, |d - vt|). \tag{2.67}$$

Results. I will now present the exact free-fermion solution in the scaling limit compared to the quasiparticle picture. See Figure 2.11 for the results. Here we see that the quasiparticle picture captures the early to late time crossover, but fails to capture the late time behaviour. Some universal features that we see is the causal structure of the bipartite mutual information, the quasiparticle modes need time to travel the separation, upon which we see a linear rise followed by an

algebraic decay. At smaller sizes of the regions A and C we see oscillations in the exact solution, which cannot be captured by the quasiparticle picture.

2.B Random Unitary Circuit: Exact Results

In this appendix, I will present a calculation of the bipartite mutual information in the case where the time evolution unitary is a brickwork ciruit where each two qubit gate (brick) is independently sampled from the Haar measure of q^2-dimensional unitary matrices, U_{q^2}, in terms of the onside space dimension, q. The quantity being calculated is the logarithm of the operator state purity averaged over this ensemble of unitaries, $\bar{I}_2^{(2)}(A:B) = \log_q \langle \mathrm{Tr}\rho_{AC}^2(t)\rangle_{U_{q^2}}$. See Figure 2.12 for the visualisation of this setup, including the tensor network contraction diagram for the operator state purity (a), the result for $q = 2$ (b), the stacked time evolution operator to be averaged over (c), and the brickwork structure of the time evolution operator (d). The calculation details continue in Figure 2.13, where I also present the effects of Haar averaging on the single brick in the circuit (a), which results in a classical partition function whose value is equal to the Haar averaged operator state purity, via the rules for the interaction between different contractions (b). The way the partition sum is carried out is in terms of a sum over a random walks of domain walls between different contraction at the initial and final time, see (c) and (d).

The last line in Figure 2.13 (c) shows how to carry out the partition sum systematically. We start at the initial time and advance. The rules suggest treating the domain walls at the initial time slice as random annihilating random walkers, each step costing the term in the partition sum a weight $\lambda = (\frac{2q}{q^2+1})^2$. Given that the weight of the walk is determined by the position of the domain walls only, we can systematically do the partition sum in terms of the (non-normalised) probability density of the domain wall location.

The (non-normalised) probability density for the location of the two domain

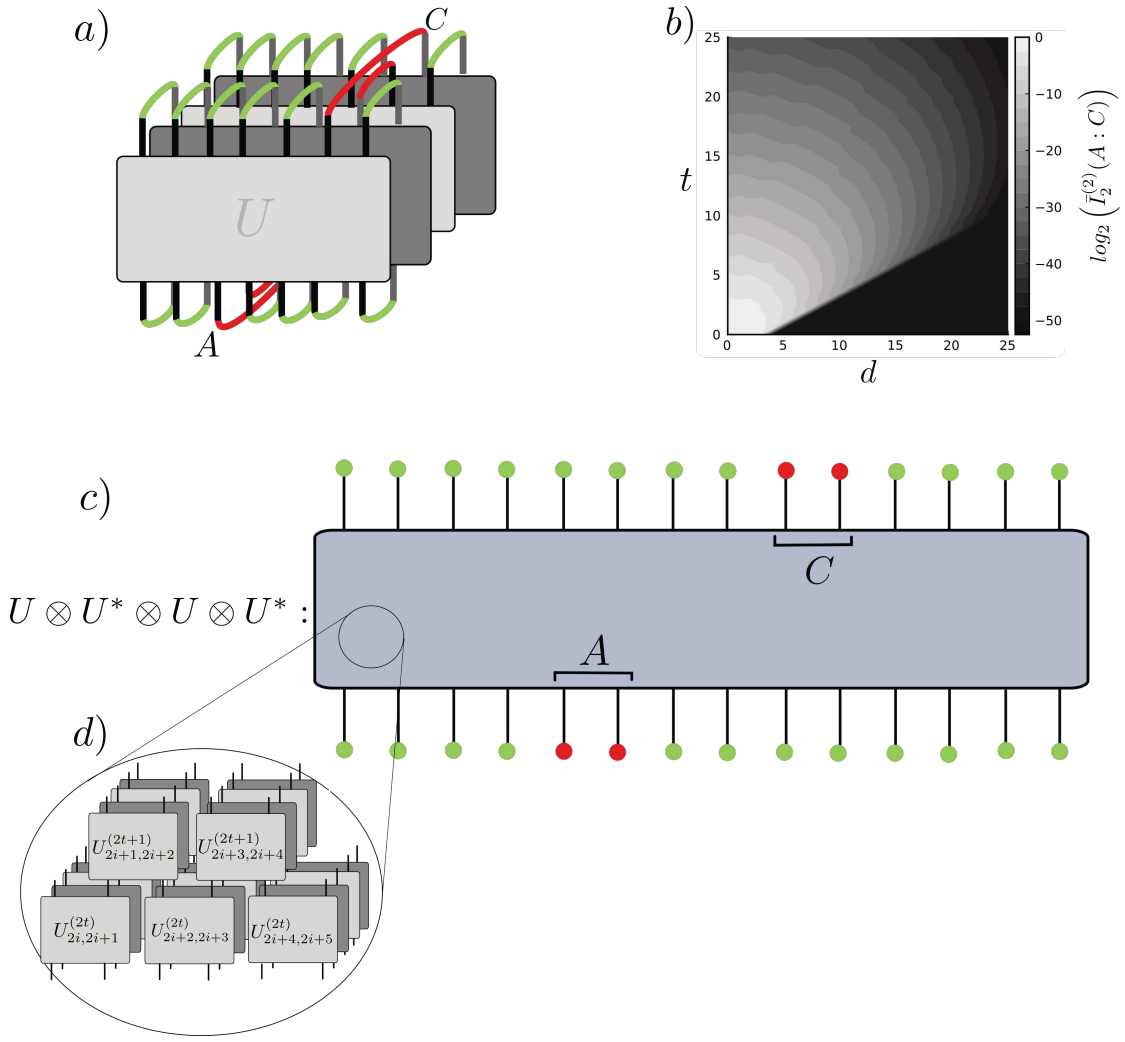

Figure 2.12: a) Tensor contraction diagram for the operator state purity $\mathrm{Tr}\rho^2_{AC}(t)$, same as in Figure 2.7c. Green and red legs, represent two kinds of index contractions. Each line refers to an on-site Hilbert space of dimension q.
b) The result for $q = 2$, $N_A = N_C = 4$. The Haar averaged bipartite mutual information is plotted against time and separation. Causal structure is evident with $v_{LR} = 2$, due to the fact that I chose to set the time unit as two layers of the circuit. Within the light cone, the structure seems to be very suggestive of the form $\bar{I}_2^{(2)}(A:B) \sim 2^{-(t^2 v_{LR}^2 + x^2)^{1/2}}$.
c) The quadrupled, stacked, time evolution operator, $U \otimes U^* \otimes U \otimes U^*$, Figure (a) looked from the front. Each line refers to a tensor product of four on-site Hilbert spaces, and each coloured dot to one of the two contractions on this quadrupled space.
d) Brickwork stricture of the time evolution operator, each unitary gate in the set $\{U^{(\tau)}_{j,j+1}\}$ is a random unitary matrix independently sampled from the Haar measure of q^2-dimensional unitary matrices; correlations only exist between the corresponding gates in the four replicas of the time evolution unitary.

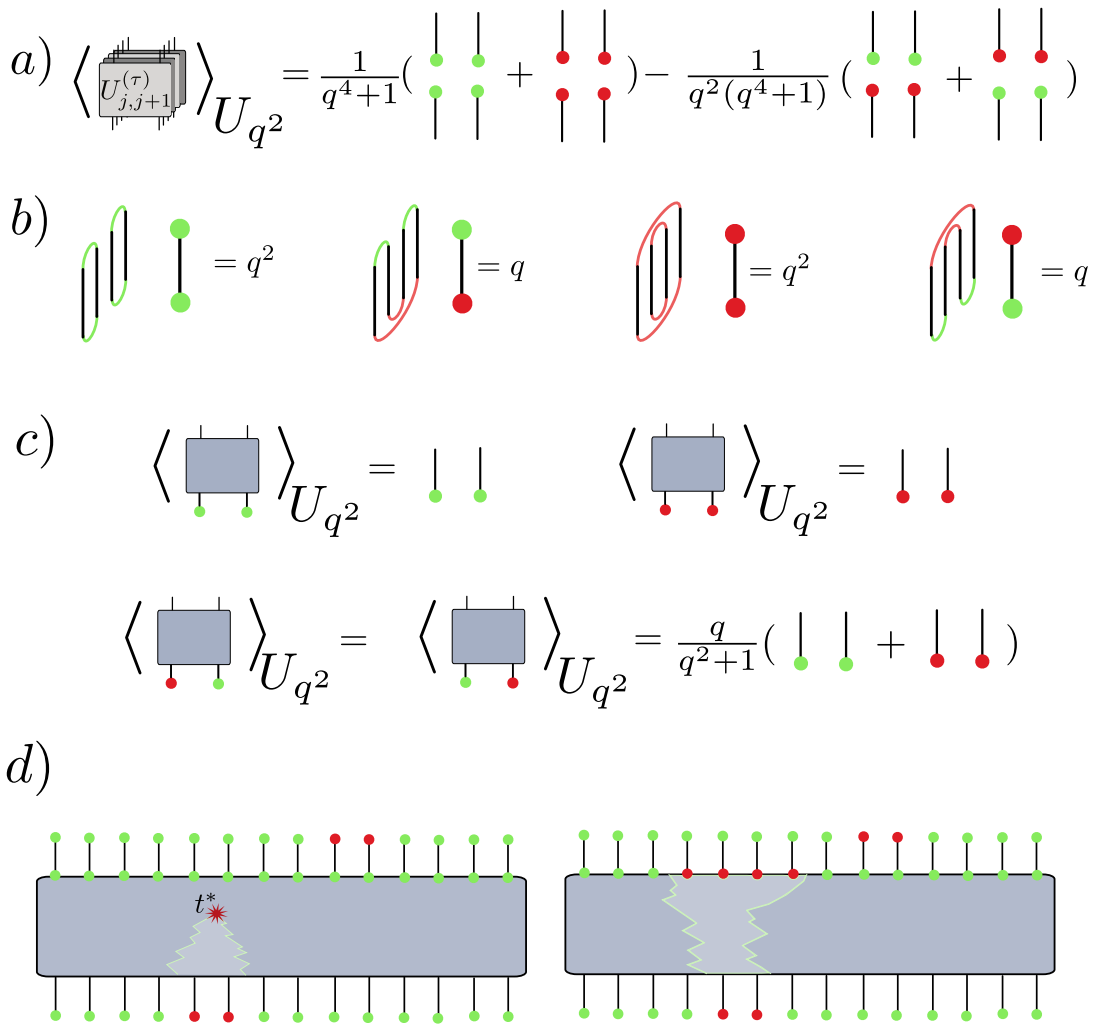

Figure 2.13: a) The effects of the Haar averaging on the single brick in the circuit. With the contraction rules (b), we can define a statistical partition function that gives us the Haar averaged operator state purity. The last line in particular suggest us that we can evaluate the partition function evolving from the initial to the final time with the two domain walls between the two kinds of contractions performing a random walk, with each step of the walk costing the weight by a factor of $\frac{2q}{d+1}$, where the walls may annihilate.
b) Interaction between two contractions on the quadrupled on-site space. If the contraction match the resulting expression is the square of the trace over identity q^2, if they do not match the resulting expression is just one trace over identity q.
c) Systematic way of doing the partition sum: the effects of averaging suggest we should to sum in layers from initial time to final time, resulting in a random walk process of domain walls (last line), with each step of the walkers costing the term in the sum a factor of $(\frac{2q}{d+1})^2$.
d) Two kinds of paths of the random walking domain walls, (c), that are present in the partition function. The first kind is where the walls annihilate at some time t^* which contribute to the partition function with a weight $\sim (\frac{2q}{d+1})^{2t^*} q^{-|N_C|}$, while the second is when the A domain survives up to the final time t_f, contributing $\sim (\frac{2q}{d+1})^{2t_f} q^{-\Delta(A_{t_f},C)}$, where $\Delta(A_{t_f}, C)$ measures number of mismatched sites between final region A_{t_f} and region C (6 in the case illustrated).

walls follow a simple difference equation:

$$p(t,x,y) = \frac{1}{4}(p(t-1,x+1,y+1) + p(t-1,x-1,y-1) + p(t-1,x+1,y-1) + p(t-1,x-1,y+1)), \text{ for } x > y, \quad (2.68)$$

with the absorption condition $p(t,x,y=x) = 0$ and the initial condition $p(0,x,y) = \delta_{x,0}\delta_{y,N_A}$, naturally $t \geq 0$, the position of the left domain wall is x and the right domain wall is y.

The (non-normalised) probability density allows us to define the survival probability of the domain walls, $P_s(t) = \sum_{x,y} p(t,x,y)$, which is the probability that two domain walls will not be annihilated by the time t. This further allows us to define the probability density of the domain wall annihilating at time t, $p_a(t) = P_s(t) - P_s(t+1)$.

See Figure 2.13 (d) for two kinds of contribution to the partition function. The first kind is when the domain walls annihilate at some time t^*, which contribute to the partition function with a weight $\sim (\frac{2q}{q^2+1})^{2t^*} q^{-|N_C|}$, while the second is when the A domain survives until the final time t_f, contributing $\sim (\frac{2q}{q^2+1})^{2t_f} q^{-\Delta(A_{t_f},C)}$, where $\Delta(A_{t_f}, C)$ measures the number of sites mismatched between the final region A_{t_f} and the region C (6 in the case illustrated), see Figure 2.13 (b) for the reason for this dependence on the domain wall mismatch.

The final result can be cast to this from:

$$\langle \mathrm{Tr}\rho_{AC}^2(t)\rangle_{U_{q^2}} = \sum_{t_i=0}^{t-1} p_a(t_i) \left(\frac{2q}{q^2+1}\right)^{2t_i} q^{-|N_C|} + \sum_{x,y} p(t,x,y) \left(\frac{2q}{q^2+1}\right)^{2t} q^{-\Delta(A_{xy},C)}, \quad (2.69)$$

the two contributions coming from the aforementioned two kinds of domain wall

paths[12]. The overlap function $\Delta(A_{xy}, C)$ is straightforwardly defined as:

$$\Delta(A_{xy}, C) = \begin{cases} N_A + N_C & \text{for } y \leq d \\ d - x + d + N_C - y & \text{for } x \leq d \text{ and } y \leq d + N_C \\ N_A - N_C & \text{for } x \leq d \text{ and } y > d + N_C \\ N_C - N_A & \text{for } x > d \text{ and } y \leq d + N_C \\ x - d + y - d - N_C & \text{for } x > d \text{ and } y > d + N_C \\ N_A + N_C & \text{for } x > d + N_C \end{cases} . \tag{2.70}$$

Taking the scaling limit would most likely allow one to exact closed-form expressions. However, I have not done this, opting instead, for this preliminary study, to solve the difference equation up to some final time, as well as evaluating the partition function, eq. (2.69), on a computer. The results for the case of a qubit chain, $q = 2$, are shown in Figure 2.12 (b), with $N_A = N_C = 4$. The results show a clear causal structure naturally enforced by the brickwork structure of the time evolution operator, with the Lieb-Robinson velocity $v_{LR} = 2$, due to the fact that I chose to set the time unit as two layers of the circuit. Within the light cone, the structure seems to be very suggestive of the form: $\bar{I}_2^{(2)}(A : B) \sim 2^{-(t^2 v_{LR}^2 + x^2)^{1/2}}$, a result that may be a generic property of time evolution without conservation laws. This sets the minimal time we need to wait for non-conserved contribution to the mutual information to attenuate before we can see the effects of the conserved quantities.

[12]The $t \to \infty$ limit of this expression implies the following closed form for the annihilation time probability density $p_a^{(N_A)}(t) = \frac{1}{t!} \frac{d^t}{dx^t} \frac{x^{N_A/2}}{(1+\sqrt{1+x})^{N_A}}|_{x=0}$.

When Alexander came to Gordium, he had a very strong desire to go up to the acropolis, where the palace of Gordius and his son Midas was, to see Gordius' wagon and the knot on the yoke of the wagon.

— from *"Anabasis of Alexander"* by Arrian of Nicomedia

3

Non-Abelian Anyons on NISQ Devices

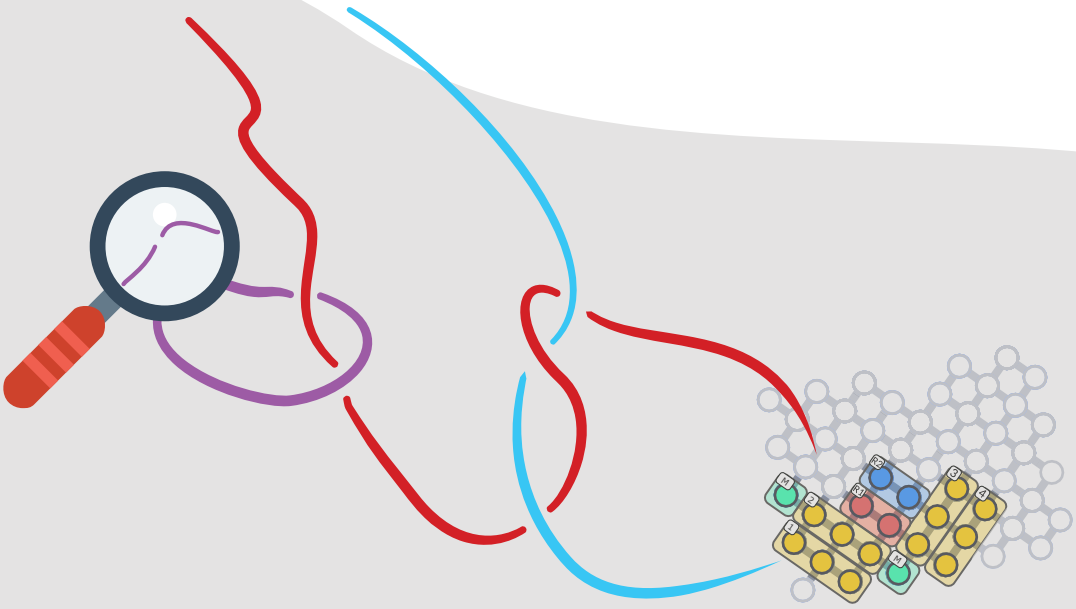

Building on the motivation laid out in the second part of the *Thesis Introduction*, I will now present our published work on the feasibility of observing non-Abelian anyon braiding on a NISQ simulator:

> Jovanović, J., Wille, C., Timmers, D., and Simon, S. H., 2024. *A proposal to demonstrate non-abelian anyons on a NISQ device.* Quantum, 8, 1408.

In particular, the anyons we consider are the excitations of the Kitaev quantum double model[54]. One of the defining inputs to the model is the gauge group G and if that group is non-abelian, then the resulting model hosts non-abelian anyons. Implementation of this model on a NISQ simulator has been argued to be unfeasible at the current level of fidelity[132, 133]. The difficulty lies primarily in the preparation of the ground state, which can be overcome using measurement-feedforward approaches[76]. Measurement-feedforward techniques employ adaptive circuits, where the gates are chosen depending on the outcome of the measurements distributed throughout the circuit; the circuit adapts based on the outcome of intermediate measurements. We did not consider quantum devices with this capability, hence we did not focus on the ground-state preparation, instead developing a number of techniques that drastically reduce the depth of conventional circuits that manipulate anyons and measure the topological charge, without relying on feedforward techniques.

Our protocols are generic for quantum double models, but we have tested the proposed experiments in the case of quantum double of the dihedral group $G = D_4$, since the number of group elements is $|D_4| = 8 = 2^3$ making them easy to encode on 3 qubits[1]. The tests were performed via classical noisy simulation of Google's Sycamore chip[77]. The simulation and noise data are implemented in Google Quantum's own `cirq` and `cirq_google` packages, see our Repository [6]. The results of our numerical studies suggest that many elements of the non-abelian anyon phenomenology; non-unique fusion and non-abelian braiding, can be clearly observed. Furthermore, much of the anyon theory data; linking and twist matrix elements, can also be estimated (amplitude and phase) via our anyon interferometry protocols.

[1]For an additional example of $G = S_3$ I direct the reader to Section 6 of our Paper [2]

The chapter is structured as follows. The next section is a general review of quantum double models, introducing the notation used throughout the chapter and explaining the anyon content of this type of models, by the end of the section I also present the two main protocols; one for anyon manipulation and another for topological charge measurement. Section 3.2 adapts the general protocols presented for the case of $G = D_4$, it lays down the relevant circuits and defines the experiments that we will benchmark with classical noisy simulation. The numerical results are presented, analysed, and discussed in Section 3.3. Finally, the whole chapter is briefly summarised. The appendices mostly complete the data (additional circuits, anyon data, etc.) presented in the main text, except for Appendix 3.D which deals with computation of $F-$ and $R-$matrix elements for quantum double models.

3.1 Quantum double models

In this section, we will discuss Kitaev's quantum double models [54]. While we assume that our readers are largely familiar with quantum double models, we nevertheless include this review to set notations and conventions, which vary throughout the literature. In addition to that, the last two parts of this section include additional material crucial for our implementation. In particular, we discucss the concrete protocol for applying ribbon operators and a non-standard protocol to infer anyonic charge via a so-called *partial* charge measurement.

Kitaev's quantum double models are (2+1d) Hamiltonian formulations of lattice gauge theory for finite gauge groups. Gauss' law is enforced energetically at each vertex by a Hamiltonian term and the model is at the deconfinement fixed point, where there are no electric field terms. The Hamiltonian, therefore, has two sets of terms – the gauge-invariant plaquette terms and the Gauss' law vertex terms [54, 134].

Quantum double models can also be understood as a subclass of the more general string-net models [62], which describe all non-chiral (2+1d) topological phases of matter, or as a generalisation of Kitaev's toric code [54] for which the gauge group $\mathbb{Z}_2$ is generalised to an arbitrary discrete group G. While all quantum

double models have anyonic excitations, the anyons for models with abelian gauge group are themselves abelian. In order to obtain non-abelian anyons, it is necessary to consider non-abelian gauge groups G. While the models for the latter are conceptually still very similar to the toric code, their definitions require slightly more care and notation, which we will introduce in the following.

Hamiltonian. For a given group G we can define its quantum double model on any arbitrary cellulation[2] of a surface without boundary. To consistently define the model, the edges (1-cells) need to be oriented as will be explained in more detail below. The local degrees of freedom are $|G|$-dimensional and assigned to the edges. The basis of their local Hilbert space is labeled by the group elements, i.e., we think of edges as being labeled by elements $g \in G$. The Hamiltonian is given by a sum of mutually commuting terms that act on vertices (0-cells) V and plaquettes (2-cells) P, respectively

$$H = -\sum_{v \in V} \mathbf{B}_v - \sum_{p \in P} \mathbf{A}_p \ . \tag{3.1}$$

Note, that we will here use a formulation of the theory on the *dual* lattice compared to the lattice of the original work in Ref. [54]. We will now discuss these terms in more detail. As mentioned above, the vertex term enforces Gauss' law. To achieve this we first introduce a general vertex operator $B_v(h)$ for every vertex v. This operator projects onto all states for which the group elements assigned to the edges adjacent to the vertex multiply to h. To make the product unambiguous we need to order the edges. This ordering has to fulfil additional constraints to be specified momentarily. In addition, a group element g assigned to an incoming (outgoing) edge enters as g (g^{-1}). E.g., for the trivalent vertex depicted in Fig. 3.1a we have

$$B_v(h)|g_1, g_2, g_3\rangle = \delta_{g_1 g_2 g_3, h}|g_1, g_2, g_3\rangle \ . \tag{3.2}$$

Gauss' law is then enforced by choosing $\mathbf{B}_v = B_v(e)$, where e denotes the identity element of the group. To ensure that the vertex projector commutes with the plaquette projector introduced below, the ordering of the edges needs to be consistent

[2] A planar graph representing a discretisation of the surface, e.g. triangulation.

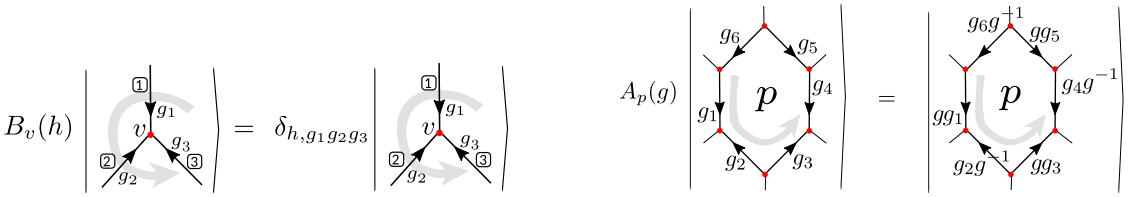

(a) **(b)**

Figure 3.1: (a) Vertex operator. The vertices are oriented in accordance with the plaquettes (counter-clockwise) and have a starting edge to make the group multiplication assignment unambiguous. (b) Plaquette operator. The orientation of the plaquettes determines pre-multiplication or post-multiplication with the inverse and is chosen in agreement with the orientation of the vertices (counter-clockwise).

with the orientation of the latter. This can be done by endowing both with a counter-clockwise orientation. The ordering is then obtained by additionally specifying a starting edge for each vertex.

The plaquette term $\mathbf{A}_p = \frac{1}{|G|}\sum_{g\in G} A_p(g)$ is defined in terms of operators $A_p(g)$ which shift the labels of the edges forming the plaquette by g. As alluded to previously, the plaquettes have an *orientation*. If the edge direction is aligned (anti-aligned) with this orientation, the shift acts as $g_i \to gg_i$ ($g_i \to g_i g^{-1}$). E.g., for the plaquette shown in Fig. 3.1b, we have

$$A_p(g)\,|g_1, g_2, \ldots\rangle = |gg_1, g_2g^{-1}, \ldots\rangle\,. \tag{3.3}$$

Ground state. It is not hard to verify that all terms in the Hamiltonian commute. Hence we can diagonalise it term by term. One can show that the leftover degeneracy depends only on the genus of the surface the graph is embedded in [54, 134]. We will work on a sphere-topology, for which the ground state is unique. For most quantum computing architectures, interactions need to be local, which limits the accessible topologies. However, a disk or sphere topology (a disk closed off by one large plaquette) is accessible.

All terms in the Hamiltonian are also projectors. Hence, one way to construct the ground state is to apply all projectors onto a state that has non-zero overlap with the ground state. In particular, we can start with the state $|\{e\}\rangle$, where every edge is labelled by the identity element. This state trivially obeys all vertex

projectors, so we just need to apply all plaquette projectors

$$|\psi\rangle = \prod_{p\in P} \mathbf{A}_p \, |\{e\}\rangle \, . \tag{3.4}$$

This state is the unique ground state and corresponds to the equal weight superposition of all states respecting Gauss' law.

3.1.1 Anyon content

In the following, we will discuss the anyonic excitations in quantum double models and the algebra describing them.

The algebra $D(G)$. The ground state is stabilised[3] by the projectors in Eq. (3.1). Together with the property $A_p(g_1)A_p(g_2) = A_p(g_1 g_2)$ this implies the stronger condition

$$\begin{aligned} A_p(g)\,|\psi\rangle &= |\psi\rangle \, , \\ B_v(e)\,|\psi\rangle &= |\psi\rangle \, , \end{aligned} \tag{3.5}$$

for all $v \in V$, $p \in P$ and $g \in G$. Therefore, the elementary excitation above the ground state will violate one or more of the equations above and are characterised by how the operators $B_v(h)$ and $A_p(g)$ act on them. More precisely, these operators form an algebra [54, 134] (the quantum double algebra $D(G)$), which contains the full information about the anyonic excitations. In particular its irreducible representations (irreps) label the anyons.

For the toric code model, the A and B operators always commute and their algebras can be investigated independently. One finds the well-known e and m particles associated to vertex and plaquette violations, respectively, and their combination, the fermionic (e, m)-particle. However, for non-abelian gauge-groups the operators $A_p(g)$ and $B_v(g)$ no longer commute, if the vertex v intersects the plaquette p. To discuss their joint algebra, we consider *sites* $s_i = (v_i, p_i)$ of adjacent vertices and plaquettes.

[3] Meaning, it is the +1 eigenstate.

On the same site we have the following algebraic relations

$$\begin{aligned} A_s(g)A_s(h) &= A_s(gh), \\ B_s(g)B_s(h) &= \delta_{g,h}B_s(h), \\ A_s(g)B_s(h) &= B_s(ghg^{-1})A_s(g). \end{aligned} \tag{3.6}$$

This is the on-site representation of the quantum double algebra $D(G)$ [54, 134].

We will now discuss its irreducible representations. However, we will refrain from providing any derivations (see e.g. Ref. [135]) and just state the results.

The irreducible representations are labelled by two objects, a conjugacy class C of the group G and an irreducible representation χ of the centraliser $Z(r)$ of the class representative $r \in C$. The vector space on which (C, χ) acts is spanned by a basis $|\mu\rangle = |c, i\rangle$, where $c \in C$ and $i \in \{1, 2, \ldots, \dim\chi\}$, i.e., the first index goes over the conjugacy class elements while the second goes over the vector indices of the irreducible representation χ.

Note, that in the case of abelian groups, in particular the toric code, the conjugacy classes are trivial and identical to the group elements themselves. Their center is G, which has $|G|$ one-dimensional representations isomorphic to G itself. Hence, the irreducible representations are given by $|G|^2$ tuples (g, ρ_i), where any group element g is paired with any irreducible representation ρ_i, $i = 1, \ldots, |G|$.

In the general, non-abelian case the irreducible representations do not factorise as can be seen from the action of the algebra generators on the vector space spanned by $|\mu\rangle = |c, i\rangle$

$$\begin{aligned} B_{\mu\mu'}(h) &= \langle c, i|\, B(h)\, |c', i'\rangle = \delta_{c,h}\delta_{c,c'}\delta_{i,i'}, \\ A_{\mu\mu'}(g) &= \langle c, i|\, A(g)\, |c', i'\rangle = \delta_{c,gc'g^{-1}}\Gamma^{\chi}_{c,ii'}(g). \end{aligned} \tag{3.7}$$

Here, Γ^{χ}_{c} is a map from the entire group, G, onto the χ-representation matrices defined by composing the representation matrices Γ^{χ} themselves and a map $G \to Z(r)$ defined by $g \mapsto q_c^{-1} g q_{c'}$, where q_c is a group element that satisfies $q_c c q_c^{-1} = r$ and $c' = g^{-1}cg$.

To get a better understanding of the meaning behind these expressions, we consider three simple examples. Let us start with the vacuum (or trivial) representation,

labelled by $(\{e\}, \mathbb{1})$. This representation is one-dimensional and spanned by $|e, 0\rangle$

$$\begin{aligned} B(h)\,|e,0\rangle &= \delta_{h,e}\,|e,0\rangle\,, \\ A(g)\,|e,0\rangle &= |e,0\rangle\,. \end{aligned} \tag{3.8}$$

Hence, Eq. (3.5) implies that for the ground state every site hosts the trivial representation.

Other important examples are pure charges and pure fluxes. A pure flux is labelled by a conjugacy class and the trivial representation of its centre, $(C, \mathbb{1})$. Its basis vectors are $|c, 0\rangle$ for $c \in C$, with

$$\begin{aligned} B_{\mu\mu'}(h) &= \langle c,0|\,B(h)\,|c',0\rangle = \delta_{c,h}\delta_{c,c'}, \\ A_{\mu\mu'}(g) &= \langle c,0|\,A(g)\,|c',0\rangle = \delta_{c,gc'g^{-1}}. \end{aligned} \tag{3.9}$$

Pure flux excitations only violate the vertex term, the B-term.

Pure charge excitations are labelled by the group identity and a representation of the group G itself, $(\{e\}, \chi)$. Its basis vectors are $|e, i\rangle$ for $i \in \{1, 2, \ldots, \dim\chi\}$, with

$$\begin{aligned} B_{\mu\mu'}(h) &= \langle e,i|\,B(h)\,|e,i'\rangle = \delta_{e,h}, \\ A_{\mu\mu'}(g) &= \langle e,i|\,A(g)\,|e,i'\rangle = \Gamma^{\chi}_{ii'}(g). \end{aligned} \tag{3.10}$$

Pure charge excitations only violate the plaquette term, the A-term.

In particular, if we have a gauge field state, $|\chi, p; i\rangle$, where each site hosts a trivial representation except for one, (v, p), which is occupied by a pure charge $(\{e\}, \chi)$[4], this state satisfies all the constraints in Eq. (3.5) except for

$$A_p(g)\,|\chi,p;i\rangle = \sum_{i'} \Gamma^{\chi}_{ii'}(g)\,|\chi,p;i'\rangle\,, \tag{3.11}$$

where i and i' are the internal degrees of freedom of the charge[5]. This is the way a charged state transforms under gauge transformations in gauge field theory. Hence, we say that the plaquette terms generate gauge transformations.

All other excitations which are neither pure charge nor pure flux are called dyons. They violate vertex and plaquette terms simultaneously, meaning they have a flux component associated with a vertex of the site (v, p) and a charge

[4]Note, that such a configuration is impossible on a sphere, but may occur on manifolds of genus $g > 0$.

[5]Note that the charge can be vector valued for non-abelian symmetry groups.

component associated with its plaquette, but unlike the toric code fermion they cannot generally be broken down to a combination of pure charge and pure flux sitting next to one another.

Non-abelian anyons. To understand the distinction between abelian and non-abelian anyons we will focus on the physical meaning of the dimension $d = \dim(C, \chi) = |C|\dim(\chi)$ of the irreducible representations.

If we have a gauge field state with an anyon of type (C, χ) at a site s, the plaquette and vertex terms of that site will transform this state in accordance with that d-dimensional algebra representation. This implies that specifying the type and location of this anyon does not uniquely fix the gauge field state. Instead, there is a d-dimensional subspace $\mathcal{H}_s(C, \chi)$ of the total Hilbert space associated with this anyon occupying this site. This d-fold degeneracy can be interpreted as a spin-like internal degree of freedom of the anyon.

Generalising this, we find that for a state with specified charge content $\{(C_s, \chi_s)\}_s$ on all (non-overlapping) sites s the subspace associated to this configuration is

$$\mathcal{H}_{\{s\}} = \bigotimes_s \mathcal{H}_s(C_s, \chi_s). \tag{3.12}$$

A more powerful alternative to this local description can be derived, if we notice that there is an algebra associated with the tensor product of representations, analogous to the Clebsch-Gordan (CG) decomposition of tensor products of linear representations of a group into the direct sum of irreducible representations.

In particular, if we have two charges a and b the associated Hilbert space can be written as a direct sum of the Hilbert space associated to charges c. We write this as

$$a \otimes b = \bigoplus_c N_{ab}^c c, \tag{3.13}$$

with a, b and c going over a set of anyon labels (C, χ) and N_{ab}^c being integer coefficients.

How this manifests physically is that if we have two anyons a and b in some region and measure the topological charge associated to that region we may get any label c for which $N_{ab}^c \neq 0$. This process is referred to as anyon fusion.

The general expression for N_{ab}^c is cumbersome. For pure charge anyons $(\{e\}, \chi_i)$ it readily reduces to the well-known decomposition of a tensor product of group irreps into the direct sums of irreps $\chi_i \otimes \chi_j = \bigoplus_k n_{ij}^k \chi_k$.

If the gauge group is abelian, all algebra representations are one-dimensional and there is no degeneracy once the charge content of a gauge field is specified. The fusion is unambiguous. We can see this by looking at the dimensions of the LHS and RHS of Eq. (3.13). For every a and b there is only one c for which $N_{ab}^c = 1$ and it is zero for all other c.

The Hilbert space associated with the presence of multiple non-abelian anyons is the stage on which all striking phenomena of non-abelianess are played out. Besides the possibility of multiple fusion outcomes discussed above, also moving anyons around one another (braiding) acts non-trivially on this space and corresponds to a unitary operation. In such a braiding process the order of exchanges matter as in general the unitary matrices associated to the individual exchanges do not commute. The full theory that describes the braiding and fusion of anyons is a so-called unitary modular tensor category (UMTC) [54].

3.1.2 Ribbon operators

In the following, we will explain how to create and move anyons. Anyons can always be created in pairs from the vacuum and for any anyon type, (C, χ), and for any path on the graph between two sites, see Figure 3.2, there is a *ribbon operator* that creates a pair of said anyons at the end sites.

If the ribbons are closed and contractable, the associated ribbon operators leave the ground state unchanged. Moreover, they span the loop operator algebra that leave the ground state invariant. It is in that way that the quantum double ground state knows about the anyon spectrum.

We will not explain the derivation of the ribbon operators themselves, see Ref. [54, 134], just how to apply them to a state. The ribbon operators are not unitary in general. If the anyons have a dimension larger than one, the operators

that create and manipulate them are non-local projectors. To simulate them on a digital quantum computer requires ancillas and measurements [75].

Ref. [69] overcame this issue by means of unitary lattice deformations[6], unitarily transforming from a state with a set of non-abelian defects on one graph to another state with the same defect content but defined on a different graph, hence they were able to move the non-abelian Majorana defects unitarily. However, these are extrinsic and static lattice defects on top of a theory that is an abelian $\mathbb{Z}_2$ gauge theory, hence, the nature of their non-abelian anyons is different from intrinsic gauge field excitations.

As we mentioned, a pair of d-dimensional non-abelian anyons defines a degenerate subspace of the gauge field Hilbert space that encodes the outcomes of their fusion. This encoding is increasingly non-local as we separate the anyons. However, we require accessing this information locally to move the anyons. To this end, we keep one d-dimensional ancilla qudit per end of the ribbon.

Every ribbon (cf. Fig. 3.2) is made up from two types of elementary triangles

I) A triangle consisting of two vertices and one plaquette center of the underlying graph. One side of the triangle coincides with an edge of the graph.

II) a triangle consisting of two plaquette centers and one vertex of the underlying graph. One of the triangle's sides crosses an edge of the graph.

Moving anyons means appending elementary triangles onto a ribbon. Each triangle type corresponds to a specific operator, the details of which also depend on the orientations of the edges and whether the triangle is attached to the back or front end of the ribbon. A detailed list is provided in Fig. 3.15 in Appendix 3.A.

The algorithm that creates two anyons of type (C, χ) along a ribbon path in the internal state $|\alpha; \beta\rangle = |c', i'; c, i\rangle$ is the following

[6]Which are, in principle, possible for quantum double models, but are, in practice, impractical for non-Abelian gauge groups G[134].

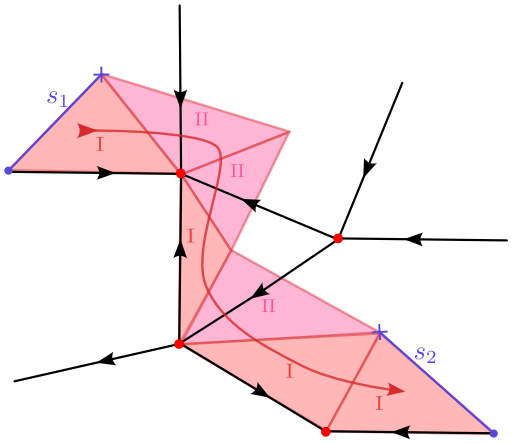

An example of a ribbon, $R = \{t_1, t_2, \ldots, t_7\}$, between site s_1 and s_2. The black lines are the edges of the graph. The ribbon is made up from four type I elementary triangles and three type II elementary triangles.

Figure 3.2

Ribbon Operator Application Protocol

1. Initialise two ($|C| \times \dim \chi$-dimensional) ancilla qudits in the states $|\alpha;\beta\rangle = |c', i'; c, i\rangle$. We will think of the first qudit as the ribbon's back end and the second as its front end.

2. For each triangle in the ribbon path, depending on the triangle *type* (and the edge orientations), sequentially apply one of the following unitaries acting on ancilla qudits $|c, i\rangle$ and qudits encoding the group element g associated to the edge of the lattice $|g\rangle_{\text{phys}}$

   I) Multiply on the coinciding edge
   $|c, i\rangle\,|g\rangle_{\text{phys}} \to |c, i\rangle\,|cg\rangle_{\text{phys}}$.

   II) Generalised-conjugate by the crossed edge
   $|c, i\rangle\,|h\rangle_{\text{phys}} \to |hch^{-1}\rangle\,\Gamma^{\chi}_{c}(h)\,|i\rangle\,|h\rangle_{\text{phys}}$.

3. To complete the application of the ribbon operator project the ancilla qudits to the Bell state $\langle\Phi^+| = \frac{1}{\sqrt{d}}\sum_{\nu}\langle\nu;\nu|$. The projection is done by measurement and post-selection.

For the other variants of Step 2 (for different edge orientations etc.) consult Figure 3.15 in Appendix 3.A.

In the way presented above, we have started building up the ribbon from start-to-finish using only forward-type elementary triangles. Similarly, we could have started in the middle and extended in parallel both forward and backwards with appropriate types of elementary triangles, see Appendix 3.A. Backwards-type elementary triangles, analogously to Step **2.** stated above, act on the backwards ancilla qudit.

As we can see, the operation is sequential so at best the depth of a circuit

implementing this is $\mathcal{O}(|R|)$, with the best depth achieved by starting at the middle and growing it both ways.

We can make this constant depth by separating the main ribbon into $|R|$ smaller ribbons which however requires $|R|$ pairs of qudits. To merge these ribbons, we also need to work with $2R$ ancillas (one pair for each cut of the circuit) and $|R|$ Bell-pair projections. As these are done via measurement and post-selection this requires an exponential in $|R|$ number of repetitions for a $\mathcal{O}(1)$ number of successful projections. Note, that this procedure is independent of quantum double models and can be applied to any sequential circuit.

In the variant of the protocol we proposed, the post-selection will necessarily raise concerns about the scaling of the number of total runs needed to build up an adequate number of successful runs. In fact, the protocol for applying an open ribbon operator onto the ground state succeeds with a probability of $1/d^2$ (neglecting the effect of noise). However, if the ribbon is closed, due to the no-flux condition of the ground state, the protocol succeeds with certainty. The number of runs needed scales exponentially with the number of open ribbon operators in the braiding protocol, which, in the cases we consider, is either one or two.

To interpret what we have here, let us look at the quantum resources. We have qudits representing the matter $\mathcal{H}_{\text{matter}}$ and ancilla qubits representing the internal state of the anyons, or the fusion space, $\mathcal{H}_{\text{ancillas}} \equiv \mathcal{H}_{\text{fusion}}$ which is already embedded non-locally in $\mathcal{H}_{\text{matter}}$. The two types of triangles couple the two spaces in two different ways. For type I the $\mathcal{H}_{\text{ancillas}}$ controls an action on $\mathcal{H}_{\text{matter}}$ and for type II it is the other way around. After the measurement that disentangles the redundant copy of $\mathcal{H}_{\text{fusion}}$, $\mathcal{H}_{\text{matter}}$ is left in a state with the ribbon operator imprinted on it as signalled by the topological charge, braiding amplitude and phase.

3.1.3 Charge measurements

In this section, we will explain how we measure the topological charge, i.e., the anyon label. This is the last element of our toolkit for probing topological order.

An ideal charge measurement would differentiate any type of excitation on any site, such measurement is associated with the following set of projectors [134]

$$P_s^{(C,\chi)} = \frac{\chi(e)}{|Z(r)|} \sum_{c\in C} \sum_{z\in Z(r)} \bar{\chi}(z) B_s(c) A_s(q_c z q_c^{-1}), \tag{3.14}$$

for each irreducible representation of $D(G)$, $\bar{\chi}(z)$ is the complex conjugate of $\chi(z)$.

Since we work in a basis where projectors onto a given G-valued flux through a vertex v, $B_v(h)$, are diagonal, we can just do a full projective measurement of the gauge field degrees of freedom in that basis. The result of such a measurement is a labelling of all edges by group elements from which we can compute the flux at any vertex.

However, in order to measure the charge component on a plaquette, one needs to implement a controlled $A_s(g)$ operator which needs a controlled group multiplication applied to all edges of s's plaquette, i.e. $|g\rangle |g_i\rangle \to |g\rangle |gg_i\rangle$ for all $|g_i\rangle$ around the plaquette. This requires circuits which, in the case of non-abelian groups such as D_4 which we will study in more detail, are prohibitively expensive.

The main idea to circumvent this problem is to instead use partial charge measurements that have a substantially reduced circuit depth. Such partial measurements do not determine the charge completely. However, when we combine a set of different partial measurements we are able to deduce the full charge content from the measurement outcomes.[7]

The key idea behind the partial measurement protocol is that controlled $A_s(g)$ becomes significantly simpler to perform once we restrict ourselves to a proper subgroup of the full group, i.e. $g \in H \subset G$.

With Eq. (3.11) in mind, we propose the following algorithm for the H-partial charge measurement on a plaquette p

[7]Note, that these measurements are destructive, meaning we need to prepare the state again for the next measurement. However, if we only need to use a small number of different subgroups (in the case of $D(D_4)$ considered here at most three different subgroups are sufficient), this trade-off is acceptable.

Partial Charge Measurement Protocol

1. Prepare an ancilla qudit, a, encoding the elements of $H \subset G$, in an equal superposition over all elements, so that the joint total state of the system is
$$\frac{1}{\sqrt{|H|}} \sum_{h\in H} |h\rangle_a |\psi\rangle_{\text{phys}} ,$$
where $|\psi\rangle_{\text{phys}}$ is the physical system.

2. Apply an a-controlled A-multiplication onto the edges of the plaquette p
$$\frac{1}{\sqrt{|H|}} \sum_{h\in H} |h\rangle_a |\psi\rangle_{\text{phys}} \rightarrow$$
$$\frac{1}{\sqrt{|H|}} \sum_{h\in H} |h\rangle_a A_p(h) |\psi\rangle_{\text{phys}} .$$

3. Apply a unitary
$$U_a = \sum_{\chi_H} \sum_{i,j} \sum_{h\in H} \sqrt{\frac{d_{\chi_H}}{|H|}} \bar{\Gamma}^{\chi_H}_{ij}(h) |\chi_H; i, j\rangle_a \langle h|_a$$
onto the ancilla qudit a. Here χ_H labels the irreducible representations of $H \subset G$ and $\Gamma^{\chi_H}(h')$ are the representation matrices, with i and j being the vector indices for a given representation χ_H. The state $|\chi_H; i, j\rangle$ should be understood as one of the basis states of a $\sum_{\chi_H} d^2_{\chi_H}$-dimensional vector space which simply enumerate the irreps and their corresponding vector spaces. When H is Abelian, this reduces to a $\sum_{\chi_H} = |H|$ dimensional space, labeled by the irreps alone. A concrete qubit encoding for $H = \mathbb{Z}_4$ and $H = \mathbb{Z}_2 \times \mathbb{Z}_2$ is presented in Eqs. (3.23) and (3.24).

4. Measure the ancilla qudit a.

To see how this protocol works, let us examine the case of a gauge field with well-defined pure charge on a plaquette $|\psi\rangle_{\text{phys}} = |\chi; i\rangle$. Using Eq. (3.11) we can write the joint state after Step 2 as

$$\frac{1}{\sqrt{|H|}} \sum_{h\in H,j} |h\rangle_a \Gamma^{\chi}_{ij}(h) |\chi; j\rangle . \tag{3.15}$$

If $H = G$, the state after Step 3 becomes

$$\begin{aligned} \frac{1}{\sqrt{|G|}} \sum_{h\in G,j} U_a \left|h\right\rangle_a \Gamma^{\chi}_{ij}(h) \left|\chi; j\right\rangle = \\ \frac{1}{|G|} \sum_{h,\chi',i',j',j} \sqrt{d_\chi} \bar{\Gamma}^{\chi'}_{i'j'}(h) \Gamma^{\chi}_{ij}(h) \left|\chi'; i', j'\right\rangle_a \left|\chi; j\right\rangle = \\ \sum_j \frac{1}{\sqrt{d_\chi}} \left|\chi; i, j\right\rangle_a \left|\chi; j\right\rangle \end{aligned} \tag{3.16}$$

The decoupling we see in the last line after summing over h is guaranteed by Schur's orthogonality lemma.

In the case above, the result of the measurement in Step 4 is a label (χ, i, j), representing the charge, the internal state before the measurement and the internal state after the measurement.

If we, however, take $H \subset G$, then the charge information is partial. By partial charge information, we mean that the result of the measurement in the last step, the label (χ_H, i, j) is no longer compatible with only one charge χ but instead is compatible with a set of possible charges, i.e., the charge is not fully determined.

We may repeat the procedure using different subgroups $H \in G$ to gather further partial information on the charge in the hope that we will be able to deduce the charge fully. In the considered examples, choosing different subgroups proves to be sufficient. This relies on the partial orthogonality of character tables of a group and its subgroup, and is demonstrated for the example of the group D_4 below.

Beyond pure charges. The partial charge measurement scheme is exact, i.e., unambiguous, when the chosen subgroup coincides with the centre of the conjugacy class of an anyon (C, χ), i.e., $H = Z(r)$ for $r \in C$. The label χ_H in fact is the label of the irreducible representation of the $Z(r)$ labelling the dyon.

The full measurement protocol, in general, then consist of performing a H-partial charge measurement and then reading-off the flux f on the same site. We then compute the center of the measured flux $Z(f)$ and consider the following three cases.

If $H = Z(f)$, the protocol is complete. The measurement outcome corresponds to (C_f, χ_H).

If $H \subset Z(f)$, we need to perform partial charge measurements for other subgroups of G that are also subgroups of $Z(f)$. We then combine these results to determine the charge label uniquely. This requires partial orthogonality of the character tables, see Section 3.1.4 for an example.

If $H \not\subset Z(f)$ the measurement is discarded in post-selection and we switch to a different subgroup H.

3.1.4 Quantum double of D_4

Throughout the rest of the chapter, we will focus on the group D_4 and its lattice gauge theory. Hence in this section, we will describe the group structure of D_4, its quantum double algebra, as well as the representation theory of both.

The dihedral group of order 8 is the symmetry group of a square. It is generated by a $\pi/2$-rotation r and a reflection m along a diagonal. The group law is defined by the following identities

$$r^4 = e,\ m^2 = e,\ mr = r^3 m. \tag{3.17}$$

This group is solvable and all of its proper subgroups are abelian. It can be decomposed as $D_4 = \mathbb{Z}_2^m \ltimes \mathbb{Z}_4^r$. This decomposition is not unique, $D_4 = \mathbb{Z}_2^m \ltimes (\mathbb{Z}_2^{r^2} \times \mathbb{Z}_2^{mr})$ is also a valid decomposition.[8]

The conjugacy classes of D_4 alongside their centres are listed in Figure 3.3a. There are five conjugacy classes, which implies that there are also five irreducible representations. Their dimensions are $(1, 1, 1, 1, 2)$. The characters, i.e., the traces of the representation matrices, are given in Figure 3.3b.

When labelling the representations of the algebra $D(D_4)$, we will also need the irreducible representations of the centres of the conjugacy classes. The centres of the three non-trivial conjugacy classes are abelian and have four elements. Hence, they have four one-dimensional irreducible representations. Their character tables are shown in Figure 3.3c.

[8] The superscripts in $\mathbb{Z}_n^x$ label the group generator.

C	$Z(r),\ r \in C$
$\mathcal{C}_e = \{e\}$	D_4
$\mathcal{C}_{r^2} = \{r^2\}$	D_4
$\mathcal{C}_r = \{r, r^3\}$	$\mathbb{Z}_4^r \equiv H_r$
$\mathcal{C}_m = \{m, mr^2\}$	$\mathbb{Z}_2^m \times \mathbb{Z}_2^{r^2} \equiv H_m$
$\mathcal{C}_{mr} = \{mr, mr^3\}$	$\mathbb{Z}_2^{mr} \times \mathbb{Z}_2^{r^2} \equiv H_{mr}$

(a)

D_4	$\mathcal{C}_e$	$\mathcal{C}_{r^2}$	$\mathcal{C}_r$	$\mathcal{C}_m$	$\mathcal{C}_{mr}$
1	1	1	1	1	1
α_r	1	1	1	-1	-1
α_m	1	1	-1	1	-1
α_{mr}	1	1	-1	-1	1
ϵ	2	-2	0	0	0

(b)

H_r	e	r	r^2	r^3
1	1	1	1	1
i	1	i	-1	$-i$
-1	1	-1	1	-1
$-i$	1	$-i$	-1	i

$H_m(H_{mr})$	e	$m(mr)$	r^2	$mr^2(mr^3)$
$(1,1)$	1	1	1	1
$(1,-1)$	1	-1	1	-1
$(-1,1)$	1	1	-1	-1
$(-1,-1)$	1	-1	-1	1

(c)

$\langle \chi_{H_r}, \chi \rangle$	1	α_r	α_m	α_{mr}	α_ϵ
1	4	4	0	0	0
-1	0	0	4	4	0
i	0	0	0	0	4
$-i$	0	0	0	0	4

$\langle \chi_{H_m}, \chi \rangle$	1	α_r	α_m	α_{mr}	α_ϵ
$(1,1)$	4	0	4	0	0
$(1,-1)$	0	4	0	4	0
$(-1,1)$	0	0	0	0	4
$(-1,-1)$	0	0	0	0	4

$\langle \chi_{H_{mr}}, \chi \rangle$	1	α_r	α_m	α_{mr}	α_ϵ
$(1,1)$	4	0	0	4	0
$(1,-1)$	0	4	4	0	0
$(-1,1)$	0	0	0	0	4
$(-1,-1)$	0	0	0	0	4

(d)

Figure 3.3: (a) The conjugacy classes of D_4 alongside their centres. (b) Character table of D_4. (c) Character tables of relevant subgroups of D_4. The groups H_m and H_{mr} are isomorphic. (d) Partial orthogonality of D_4 with respect to its three four-element subgroups.

Anyon content of $D(D_4)$. The task of listing all irreducible representations of $D(D_4)$ and their dimensions from this data is straightforward. There are $2 \times 5 + 3 \times 4 = 22$ irreducible representations, i.e., types of anyons in the D_4 quantum double model (i.e. 2 conjugacy classes with 5 centraliser irrep and 3 classes with 4).

Eight of these irreps are one-dimensional, i.e. abelian, while the rest are two-dimensional. Other than the vacuum, four of them are pure charges and four are pure fluxes. For dyons with the $\mathcal{C}_{r^2}$ flux component we say that they have a trivial flux even though it is not the vacuum flux. The flux can be factored out, just like in the case of the toric code fermion. This comes from the fact that r^2 commutes with all group elements, just like the identity.

We label the vacuum and the trivial flux as $0 \equiv (\mathcal{C}_e, 1)$ and $\tilde{0} \equiv (\mathcal{C}_{r^2}, 1)$, respectively. Likewise, the pure charges and dyons with vacuum and trivial flux are labelled as $\Sigma_\chi \equiv (\mathcal{C}_e, \chi)$ and $\tilde{\Sigma}_\chi \equiv (\mathcal{C}_{r^2}, \chi)$, with χ being one of the nontrivial irreducible representations of D_4. Nontrivial pure fluxes are labelled $\Psi_x = (\mathcal{C}_x, 1)$, with C_x being one of the nontrivial conjugacy classes of D_4. The rest of the dyons have less informative labels such as $\{\tilde{\Psi}_x, \Phi_x, \tilde{\Phi}_x\}$ and can be found in Appendix 3.B, where we also provide the quantum dimensions and the topological twists together with the fusion rules.

Charge measurements reprise. Let us review the partial charge measurements for $D(D_4)$. We choose the subgroups $\{H_r, H_m, H_{mr}\}$ for the measurement protocol. All the irreducible representations of these subgroups, χ_{H_x}, are one dimensional. This means that the measurement outcome of the partial charge measurement is just the irrep label (χ_{H_x}). Looking at their character tables, we find a partial orthogonality with the characters of the irreps of G. Concretely, we compute $\langle \chi_{H_x}, \chi \rangle = \sum_{h \in H_x} \chi^*_{H_x}(h)\chi(h)$ for the five different charges and list the results in Figure 3.3d.

For example, imagine we performed a H_m-partial charge measurement on a plaquette p and obtained the measurement outcome $(1, 1)$. This label has a non-vanishing overlap with the trivial charge 1 and charge α_m. Hence, both 0 and Σ_{α_m} can be anyons present on the plaquette.

Now imagine we have performed all three measurement and obtained the set of labels $\{-1, (1, 1), (1, -1)\}$. This set is only compatible with the charge α_m and hence Σ_m must be on a plaquette p.

Beyond pure charges. The four main subgroups we consider in the partial charge measurement are also the centralisers of the respective conjugacy classes, $H_x = Z(x)$. Hence, as mentioned in the last section, if we read-off the flux whose centre is the subgroup we used in the partial charge measurement, the result uniquely determines the dyon label.

It is only for dyons of trivial flux, $\{e, r^2\}$, that we need to use the repeated partial charge measurements with different subgroups alongside partial orthogonality of

the character tables of D_4 and its four-element subgroups to uniquely determine the topological charge.

3.2 Probing non-abelian anyons

In this section, we will present a set of protocols that allow us to demonstrate the non-abelian character of the anyons of $D(D_4)$ on realistic to-date quantum hardware. The main obstacle to overcome here is the noise which limits the depth of the circuits. We will show how low circuit depths can be achieved for all protocols. A benchmark of the proposed experiments is presented in the next section showing numerical simulation results for a realistic noise model.

The main experiments showcasing the non-abelian nature of the excitations we propose are the following.

i) Anyon fusion. Here, the non-abelian nature is signalled by non-unique fusion outcomes.

ii) Non-abelian braiding. The order of the braids does not commute.

iii) S- and T-matrix measurements. This data describes the amplitudes of links and twists and almost uniquely[9] characterises the full anyon theory.

3.2.1 Achieving low circuit depth

In this section, we will discuss how to achieve low circuit depths for creating and moving the anyons of $D(D_4)$. We will present the encoding of group elements into qubits, and show how short circuits for the elementary triangles of the ribbon operators discussed in Section 3.1.2 can be obtained.

Encoding. The order of D_4 is 8, hence we need three qubits to encode a group element. We chose the following map

$$|g\rangle \equiv |a\rangle_m |b\rangle_r |c\rangle_{r^2} \iff g = m^a r^b (r^2)^c, \tag{3.18}$$

[9]There are some exceptions, where the anyon theory, i.e., the UMTC is not determined uniquely by the S-and T-matrices alone [136]. The smallest known example where this is the case has 49 particle types.

where $a, b, c \in \{0, 1\}$, r is the 90° rotation and m is the reflection.

When encoding the internal space of the anyon, which we need for the ribbon operator protocol, we note that the basis $|\nu\rangle = |c, i\rangle$, contains a group element $c \in C$ restricted to a conjugacy class. All the non-trivial conjugacy classes contain just two elements and can be encoded with only one qubit. Since the centralisers of these conjugacy classes are abelian and their representations are one-dimensional, we can encode the full internal space of the anyon with just one qubit. For anyons with m-flux, (C_m, χ), we have

$$|c, 0\rangle \equiv |a\rangle_a \iff c = m^1 r^0 (r^2)^a \in \{m, mr^2\}, \tag{3.19}$$

for anyons with mr-flux, (C_{mr}, χ), we have

$$|c, 0\rangle \equiv |a\rangle_a \iff c = m^1 r^1 (r^2)^a \in \{mr, mr^3\}, \tag{3.20}$$

and for anyons with r-flux, (C_r, χ), we have

$$|c, 0\rangle \equiv |a\rangle_a \iff c = m^0 r^1 (r^2)^a \in \{r, r^3\}. \tag{3.21}$$

Similarly the subgroups are encoded with two qubits. For example for $h \in H_r$ we use

$$|h\rangle \equiv |a\rangle_r |b\rangle_{r^2} \iff h = m^0 r^a (r^2)^b. \tag{3.22}$$

To encode the four different representations of the subgroups χ_H for H_m and H_{mr} we use

$$|(-1)^a, (-1)^b\rangle \equiv |a\rangle_a |b\rangle_b , \tag{3.23}$$

where (a, b) corresponds to the representation label used in Table 3.3c, and for H_r we use

$$|i^{2a+b}\rangle \equiv |a\rangle_a |b\rangle_b , \tag{3.24}$$

where i^{2a+b} corresponds to the representation label used in Table 3.3c.

Circuits. To implement the anyon protocols we need circuits for the following operations.

Elementary circuits

1. Controlled group multiplication $|g,h\rangle \to |g,gh\rangle$
   (a) full domain variant ($g \in G$), used for ground state preparation,
   (b) restricted domain variant ($g \in C$), used in ribbon operators,
   (c) restricted domain variant ($g \in H$), used for partial charge measurements.
2. Controlled generalised conjugation
   $|c\rangle |i\rangle |g\rangle \to |gcg^{-1}\rangle \Gamma_c^{\chi} |i\rangle |g\rangle$.
3. Decoupling unitary of the partial charge measurement

$$U_a = \sum_{\chi_H, i', j', h' \in H} \sqrt{\frac{d_{\chi_H}}{|H|}} \bar{\Gamma}^{\chi_H}_{i'j'}(h') \, |\chi_H; i', j'\rangle_a \, \langle h'|_a \, .$$

We will focus on a set of examples illustrating the expected circuit depths. The full domain group multiplication (see Fig. 3.4a) consists of three Toffoli and 2 CNOT gates. Note, that on most hardwares a 3-qubit Toffoli gate must be decomposed into 2-qubit gates. Hence, each Toffoli gate should be seen as a depth-6 circuit in itself[10]. With this in mind, the circuit depth for a single group multiplication is 22. Current noise levels limit the circuit depth to about 100 gates. Therefore, a naive protocol based on full domain group multiplication is doomed to fail.

We now contrast this with the reduced domain multiplication, where the control qubits are restricted to a certain conjugacy class. A representative example is shown in Fig. 3.4a. The circuit is reduced to a depth-1 circuit with only one CNOT gate. We can appreciate a dramatic reduction of circuit depth achieved by restricting the domain of the controlled multiplication circuit.

This is one of the main facts that allows us to greatly simplify many circuits related to ribbon operators and partial charge measurements. However, the direct ground state preparation does not benefit from these simplifications. We will discuss the ground state preparation separately in the next section.

[10] If the coupling gates are restricted to act on neighbouring qubits, additional swaps may be needed which increase the depth to up to 12.

Let us move on to the generalised conjugation. The circuit depth for this heavily depends on the type of anyon. For a pure flux the representation matrix Γ is trivial and the generalised conjugation simplifies to a conventional conjugation which can be implemented by a circuit of depth one or two (see Fig. 3.4b for an example). In contrast, for a dyon with a one-dimensional but non-trivial irrep of the center, the circuit is more involved. Since the irrep is one dimensional, it corresponds to a phase factor and does not need to be encoded in an additional vector space. I.e., we can still use $|c\rangle$ instead of $|c, i\rangle$. However, the conjugation of c has to be accompanied by appropriate phase factors implementing the action of $\Gamma_c^\chi(g)$. A circuit showing such a generalised conjugation for the m-dyon $\tilde{\Phi}_m \equiv (C_m, (-1, -1))$ is shown in Fig. 3.4b. We note, that there is still no need for Toffoli gates, however, the circuit is more complex than for pure fluxes. The full list of circuits for generalised conjugations is given in Appendix 3.B.

We note that there are adaptive constant-depth circuits (measurement-based schemes) for applying ribbon operators that have better scaling for solvable gauge groups [137] (such as D_4), but the measurement overhead makes them less preferable for small systems.

Lastly, we look at the decoupling unitaries for partial charge measurements. The unitaries for subgroups $H \subset G$ are shown in Figure 3.4c.

Geometry and ground state preparation. Our proposal for ground state preparation does not use any feed-forward protocols. Therefore, it is suitable for an experimental set-up, where measurements terminate the circuit. We also note, that so far known feed-forward protocols for ground state preparation only cover quantum double models for solvable groups excluding more complex quantum double models and the more general string-net models based on fusion categories beyond groups.

Not using a feed-forward protocol, however, comes at the cost of limiting the lattice geometry to either small two-dimensional graphs or quasi one-dimensional graphs in order to keep the circuit depth short.

For the majority of our result, we will focus on a quasi one-dimensional graph, that we call *braiding ladder*. This geometry is shown in Figure 3.5.

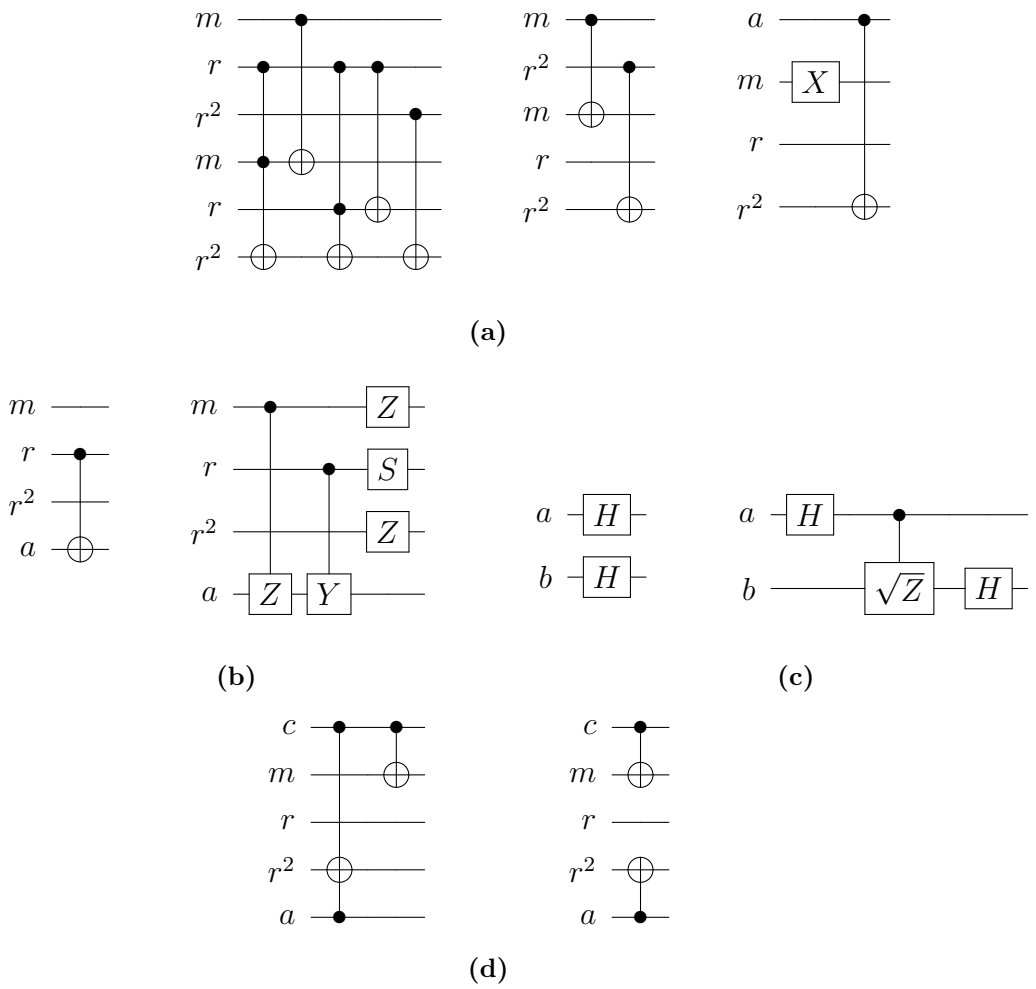

Figure 3.4: (a) Circuits for controlled group multiplication $|g, h\rangle \to |g, gh\rangle$. Left: Both g (first three qubits) and h (last three qubits) are unrestricted, i.e., $g, h \in G$. Center: $g \in H_m$ is encoded by just the first two qubits. Right: $g \in C_m$ is encoded by just the first qubit a (cf. Eq. (3.19)).
(b) Circuits for generalised conjugation. The first three qubits encode the physical, group valued, gauge field $|g\rangle$. The last qubit encodes the ancilla qubit representing the internal state of the (two-dimensional) anyon $|c\rangle$. Left: The conjugation unitary for a pure flux Ψ_m $|c\rangle\,|g\rangle \to |gcg^{-1}\rangle\,|g\rangle$. Right: The generalised conjugation unitary for the dyon $\tilde{\Phi}_m$: $|c\rangle\,|g\rangle \to \Gamma(g)\,|gcg^{-1}\rangle\,|g\rangle$, where the representation 'matrix' $\Gamma(g) \in U(1)$ and $S = \mathrm{diag}(1, i)$.
(c) The decoupling unitary map used in partial charge measurements for subgroups of D_4. Left: $H_m, H_{mr} \simeq \mathbb{Z}_2 \times \mathbb{Z}_2$. Right: $H_r \simeq \mathbb{Z}_4$. In the circuits above H denotes the Hadamard gate.
(d) Controlled multiply circuits of an elementary triangle of a ribbon operator conditioned on a control qubit c (first qubit) acting on a physical edge (middle three qubits) and a ribbon ancilla qubit (last qubit). Left: Implementing a Ψ_m-elementary triangle vs vacuum, represented as $0 \oplus 0$. Right: Implementing an Ψ_m-elementary triangle vs $0 \oplus \tilde{0}$. Used for flavour conditioning defined later in Section 3.2.3.

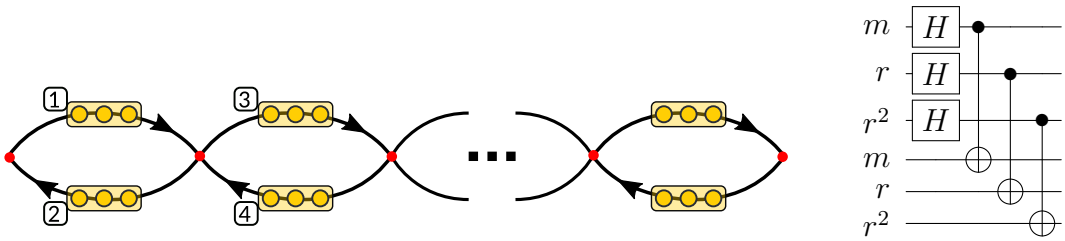

Figure 3.5: Quasi one-dimensional lattice allowing for shallow ground state preparation of the quantum double model $D(D_4)$. Left: Yellow bars denote individual spins associated to edges, which are composed of three qubits each. Edge orientations are needed to define the vertex- and plaquette operators of the corresponding Hamiltonian. The lattice is embedded into a sphere, meaning in addition to the 2-gons, there is one large 'outer' plaquette. Right: Circuit for groundstate preparation per loop.

The ground state on this geometry can be prepared with a constant-depth circuit, i.e., it does not scale with the system size. The ground state on an n-segment ladder is given by

$$|GS\rangle = \sum_{g_1,g_2,\ldots,g_n} |g_1, g_1, g_2, g_2, \ldots, g_n, g_n\rangle \ . \tag{3.25}$$

This state has no long-range entanglement and factorises into a sequence of qudit Bell-pairs. However, entanglement is built up once one introduces anyons via ribbon operators. In fact, this geometry is sufficient to correctly show the braiding statistics of the anyons. The only requirement for correctly reproducing the braiding statistics is that the ribbon paths only *touch*, but do not intersect and is fulfilled here.

The shallow circuit preparing this state is shown in Figure 3.5.

We also examine fusion on a small two-dimensional graph, as shown in Figure 3.6a.

3.2.2 Elemental protocols

Anyon fusion is the first and most basic protocol that can demonstrate non-abelianness.

After preparing the ground state, we apply two ribbon operators. One between sites s_1 and s_2, and the other between sites s_2 and s_3. This creates two pairs of anyons and fuses them on site s_2. We then perform a partial charge measurement

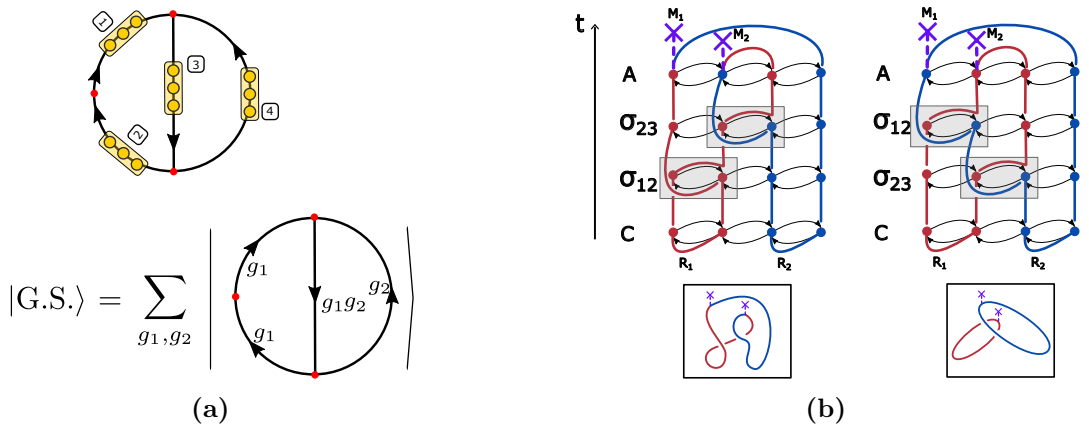

Figure 3.6: (a) A small two-dimensional graph. Top: Yellow bars denote individual spins associated to edges, which are composed of three qubits each. Edge orientations are needed to define the vertex- and plaquette operators of the corresponding Hamiltonian. Bottom: The ground state on this small two-dimensional graph. The circuit needed for its preparation is discussed in Section 3.3.1.
(b) The two braiding protocols, differing only in the order of exchanging the two anyons. C stands for creation, M for measurements. The protocol on the left will have 4 fusion outcomes, while the protocol on the right can only produce vacuum.

and flux readout for this site. This experiment can be performed on both the braiding ladder and the small two-dimensional graph.

We can do this experiment for any anyon types. Here, we will give an example for the case of fusing the pure flux Ψ_m with itself. In contrast to the abelian case, this fusion is not restricted to yield vacuum. Instead we have

$$\Psi_m \times \Psi_m = 0 + \tilde{0} + \Sigma_m + \tilde{\Sigma}_m,$$

where 0 is the vacuum, $\tilde{0}$ is the abelian flux corresponding to the other element of the centre of D_4, r^2, and the other two anyons are a pure charge associated with the α_m representation of D_4 and the dyon of this pure charge and the abelian flux.

All four of these outcomes can be differentiated by reading out the flux and performing the partial charge measurement using H_r or H_{mr}. For concreteness, we choose H_{mr} for which we expect to only observe the measurement outcomes $(1, 1)$ and $(1, -1)$, corresponding to no charge and α_m, respectively. A discussion of this protocol implemented on a realistic hardware device and a corresponding numerical simulation are shown in Section 3.3.1.

Anyon braiding. The second phenomenon that gives the non-abelian anyons their name is the fact that the image of the braid group, as represented by physically braiding these anyons, is non-abelian. This means that the order of interchanges matter, i.e. $\sigma_{12}\sigma_{23} \neq \sigma_{23}\sigma_{12}$, where $\sigma_{i(i+1)}$ is the clockwise interchange of particle i and $i+1$, the generator of the braid group.

The braiding procedures we want to implement to show this fact are shown in Figure 3.6b. We create two pairs of anyons from the vacuum, perform two interchanges $\sigma_{12}\sigma_{23}$, and then fuse pairwise. Then we repeat the same protocol with the inverted order of the interchanges, i.e., $\sigma_{23}\sigma_{12}$. For concreteness, we again consider pairs of pure fluxes Ψ_m.

In the second protocol, we annihilate the pairs that have a fixed fusion channel. Given that they are created from the vacuum they will fuse to the vacuum. In the first protocol, we annihilate the pairs whose fusion channel is not fixed, hence all four fusion outcomes are expected. We see that the two braidings indeed produce two different states.

For further discussion of a concrete implementation and numerical results, see Section 3.3.1.

3.2.3 Anyon interferometry

In order to measure the relative phase between different braiding processes, we need to devise an interference protocol. This is done by setting up a control qubit c, whose state is entangled with different braiding protocols

$$|\psi\rangle_c |\mathrm{GS}\rangle \to |0\rangle_c |\Psi_0\rangle + |1\rangle_c |\Psi_1\rangle , \tag{3.26}$$

where Ψ_i are the two wave functions of the matter degrees of freedom after two different braiding operations.

If the charge content of the two states is the same $|\Psi_0\rangle$ and $|\Psi_1\rangle$ may only differ by a constant. Hence we can write

$$|0\rangle_c |\Psi_0\rangle + |1\rangle_c |\Psi_1\rangle = (|0\rangle_c + C_{01} |1\rangle_c) |\Psi_0\rangle , \tag{3.27}$$

and by the means of tomography on the control qubit c we can extract the relative constant C_{01}.

For a suitable choice of the two braiding protocols, this constant reveals elements of the S- and T-matrix as we will see next.

S-matrix elements. To measure the S-matrix elements, we create a superposition of two states by conditioning an equal time (closed) ribbon operator shown in blue in Fig. 3.7 on the control qubit .

Note that the S-matrix appearing in Figure 3.7 is normalised

$$\tilde{S}(a,b) = \frac{\mathcal{D}}{d_a d_b} S(a,b), \tag{3.28}$$

where $\mathcal{D} = \sqrt{\sum_i d_i^2} = |G|$ is the total quantum dimension, which makes $|\tilde{S}(a,b)| \leq 1$. To see that note that [61] $S_{ab} = \frac{1}{\mathcal{D}} \sum_c N_{ab}^c \frac{\theta_c}{\theta_a \theta_b} d_c$ and $|\theta_x| = 1$. We also know that $\sum_c N_{ab}^c d_c = d_a d_b$, so it follows that $|S_{ab}| \leq \frac{1}{\mathcal{D}} d_a d_b$.

The conceptually simplest interferometry scheme is shown in Figure 3.7b. Here we apply a ribbon of flavour a, then, depending on the state of the controlling qubit, either thread a second ribbon of flavour b around the first ribbon or do nothing. This is very similar to the ideal scheme shown in Figure 3.7a.[11]

However, in this protocol every single qubit gate of the b-ribbon operator becomes a two qubit gate (since the ribbon is conditioned on the control c) and every two qubit gate becomes a three qubit gate (unitarily similar to a Toffoli gate). Hence, the number of entangling gates grows quickly with the ribbon length.

A smarter alternative is to condition the ribbon type instead (see Figure 3.7c). In this case we identify where the ribbon operators for the two anyon types differ, and condition only those operations. The circuit for this can be much shorter, see Fig. 3.4d for an example. In particular, for the case of $D(D_4)$, it turns out, that, if b has a non-trivial flux content, it is easier to compare the linking of anyons a and b to the linking of anyons a and a reducible charge $0 \oplus \tilde{0}$. (Note, that this is not a valid anyon label since the representation is reducible.) Thus, we condition whether we apply the ribbon b or the ribbon corresponding to $0 \oplus \tilde{0}$.

[11] Compared to Fig.3.7a, Fig. 3.7b is only missing a measurement checking that applying a closed ribbon b on it's own doesn't introduce any phase, which it doesn't.

The ribbon operator protocol defined for irreducible representations carries over for reducible ones. Note that the representations $0 \oplus 0$ and $0 \oplus \tilde{0}$ are two-dimensional and hence distinct from 0 and $\tilde{0}$ respectively.

However, this protocol requires additional knowledge of the theory. Concretely, if we are interested in the S-matrix element S_{ab}, we need the additional knowledge of $S(a, 0)$ and $S(a, \tilde{0})$. In fact, both can be measured easily by the protocol in Figure 3.7b since anyons 0 and $\tilde{0}$ are abelian and their ribbon operator only have single qubit gates. A similar protocol was used to measure the S-matrix in the case of the toric code [68].

If $\tilde{S}(a, 0) = \tilde{S}(a, \tilde{0}) = 1$, we can just read off $\tilde{S}(a, b)$ after tomographing the control qubit. In the case of $\tilde{S}(a, \tilde{0}) = -1$, there is a two qubit gate we need to apply between the controlling qubit and one of the ribbon ancillas before we can simply read off $\tilde{S}(a, b)$ via tomography.[12] The exact method of tomography will be presented alongside the numerical results in Section 3.3.2.

T-matrix elements. In this section, we will describe the interference protocol for measuring the matrix elements of the diagonal T-matrix, or the spin of the anyons. Here we note that ribbon operators are in-fact ribbons in space-time, hence they can acquire a twist. Each twist of anyon a contributes a phase factor to the wave function, $T_{aa} = e^{i\theta_a}$.

The protocol is illustrated in Figure 3.8a. We identify where the twisted and untwisted paths of a ribbon operator associated with some anyon a differ and apply a controlled circuit of the form illustrated in Figure 3.8b accordingly. If for the untwisted (twisted) version, we need to apply the unitary U (V), the circuit implementing is straight-forward and shown in Figure 3.8b.

The endpoint of the two ribbons are on the same site, hence the charge content is the same and we can factor out the gauge field wave function. The control qubit is in a pure state (assuming there is no noise) so we can tomograph and read off the twisting phase.

[12] See Appendix 3.C.

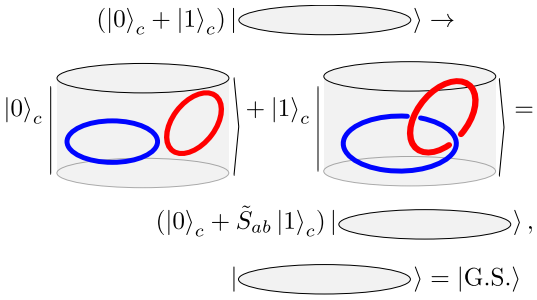

(a) The ideal interferometry scheme for measuring the S-matrix elements. The two different braids are entangled with the controlling qubit c.

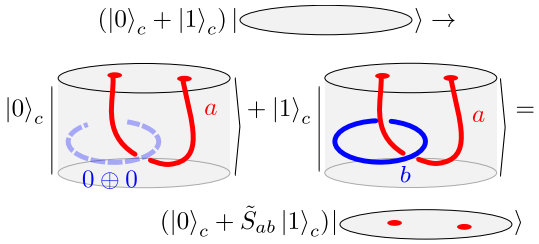

(b) Conditioning the existence of the b-ribbon. The b-ribbon is only applied, if the state of the control qubit is $|1\rangle_c$. Equivalently, we say that we condition whether to apply b or the reducible representation $0 \oplus 0$.

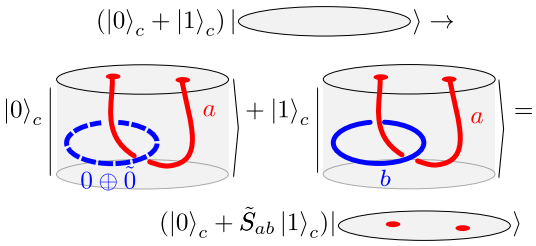

(c) Conditioning the type of the b-ribbon. If the state of the control qubit is $|1\rangle_c$, apply ribbon b. If it is $|0\rangle_c$, apply the ribbon for the reducible representation $0 \oplus \tilde{0}$.

Figure 3.7: The interference protocols used for phase sensitive measurement of the (normalised) S-matrix elements $\tilde{S}(a,b) = \frac{|D_4|}{d_a d_b} S(a,b)$.

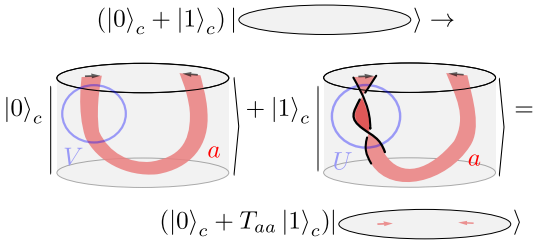

(a) Interference protocol for measuring the phase of the T-matrix elements. Note: $|T_{aa}| = 1$ for all anyons a. The inference is done between two paths that differ by only one twist. We have restored the two-dimensionality of the ribbons in our representation in order to showcase the extra twist.

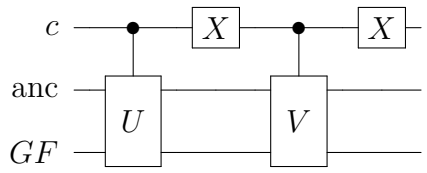

(b) A circuit that, depending on the state of the control qubit c, either applies a unitary U or V onto the joint gauge field (GF) and ancilla (anc) degrees of freedom.

Figure 3.8: The interferometry scheme to measure the phase difference between two paths alongside with a circuit diagram implementing the difference of the two paths.

3.3 Numerical experiments

In this section, we provide numerical evidence for the feasibility of our proposal on state of the art NISQ devices. We performed simulations using Google's `cirq_google` python package on Google's cloud computing platform `Google Colab`. This package executes the quantum trajectory simulation of the circuit using the Kraus operators obtained from the direct Pauli transfer matrix tomography on various single and two qubit gates on the Sycamore chip [138]. This is a conjecture, given that the details of the package are Google's trade secrets, but we assume each shot performs a pure state evolution (trajectory) with gates sampled from ensembles corresponding to the ideal gates of a circuit we want to simulate; these ensembles would be obtained by the gate tomography of the target gates on the actual device. This chip comes with two principal constraints. First, we can only perform two-qubit gates between adjacent qubits. Second, there is a limited set of elementary gates that can be implemented.

Knowing the characteristics of the single and two-qubit gates, and single- and multi-qubit readout performances of the chip [138] we have chosen a suitable part of the chip for our simulations. A similar setup would be suitable for an actual experiment on the Sycamore chip. However, the optimal allocation of resources will be chip-dependent. The layout we used is shown in Figure 3.9a.

The number of qubits we could simulate classically using this software is limited to 30, which is less than the number of qubits currently available on an actual machine. To see how this comes about, let us note that even though in our protocols there are only a few non-Clifford gates, we can not exploit the advantage of Clifford simulators because we simulate *noisy circuits*.

3.3.1 Elemental protocols

In this section, we present the simulation results for the fusion and braiding experiments.

Circuit characteristics. Before we present the results, we report on the qubit layout used for the fusion and braiding experiments, as well as circuit depths achieved, in order to put the noise observed in a useful context.

Ground state. As mentioned, we prepare the ground state directly. On the braiding ladder that procedure is depth 2 (see Fig. 3.5). We prepare the qubits on all the bottom edges in an equal superposition via Hadamard gates and then CNOT the qubits above controlled by the one below.

On the planar graph in Figure 3.6a this process is more complicated. Repeating the process as for the braiding ladder gives us the following state

$$|\Psi\rangle = \sum_{g_{12},g_{34}} |g_{12}, g_{12}, g_{34}, g_{34}\rangle \,.$$

We then apply the full controlled multiply circuit from qubits of the second edge onto the qubits of the third edge. This procedure gives us the state defined in Figure 3.6a.

Fusion. The exact ribbon operators and the layout of the qubits on the Sycamore chip used in the fusion experiment are shown in Fig. 3.9a.

Using the circuits listed in Sec. 3.2.1 to implement the ribbon operators defined in Sec. 3.1.2 generates a circuit that is not directly implementable on the Sycamore chip due to the constraints mentioned above. We first need to implement swap gates such that all the multi-qubit gates appearing in the original circuit are acting on adjacent qubits. In addition, we need to compile multi-qubit gates into native single- and two-qubit coupler gates. In our case we chose the CZ gate as the coupler (two-qubit) gate. The single qubit gates are unrestricted.

The additional swaps make up a considerable portion of all coupling gates used in the numerical experiments and hence the positioning of qubits is one of the key factors in minimising the circuit depth.

It is also worth noting that not all anyons are equal in complexity. The r-dyon ribbon operator require considerably deeper circuits since the group multiplication controlled by the elements of the $\mathcal{C}_r$ conjugacy class always involves at least one Toffoli gate. Let us recall that the Toffoli gate needs to be compiled into a circuit of at least depth 6 using the CZ as the two qubit coupler, however this neglects any swaps

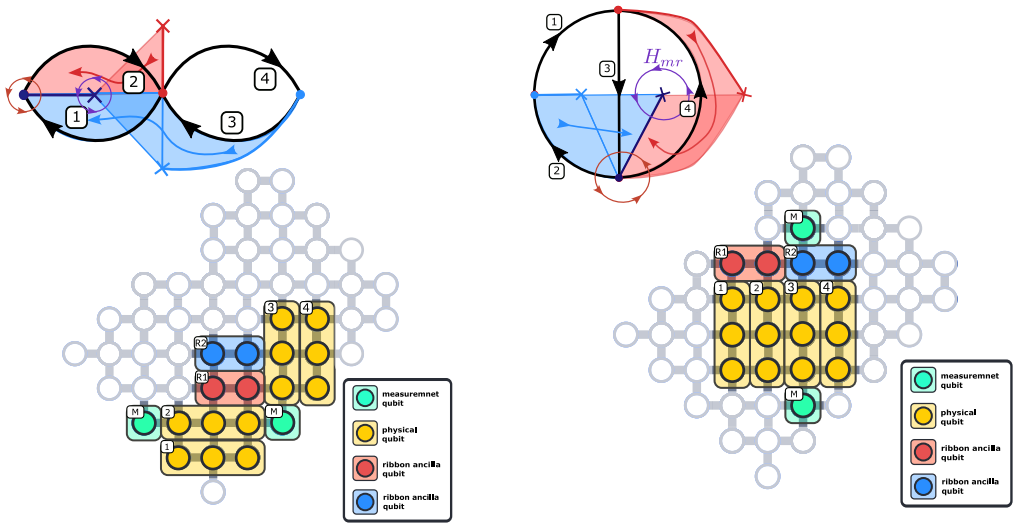

(a)

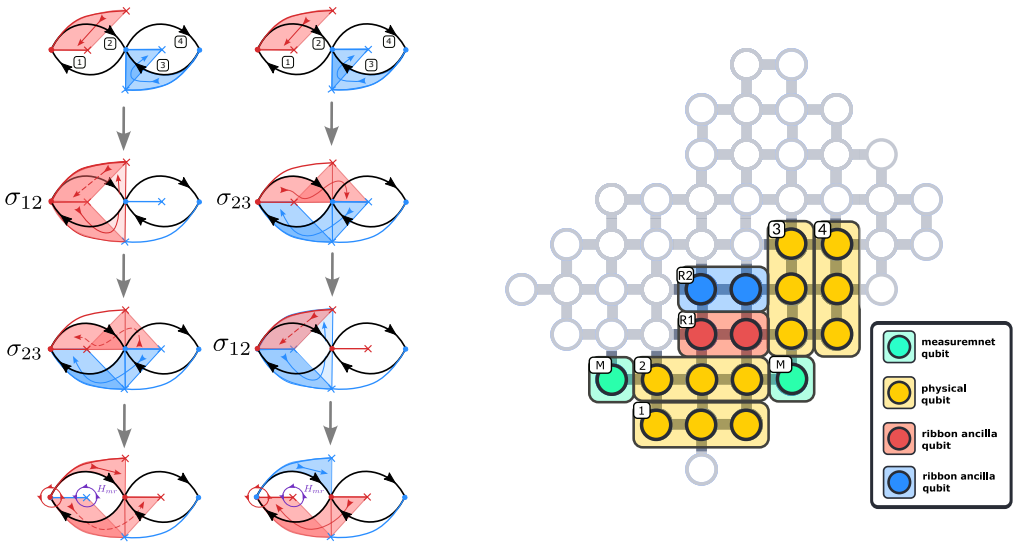

(b)

Figure 3.9: (a) Ribbon operators and qubit layout for the fusion of two Ψ_m anyons on the braiding ladder (left) and a small planar graph (right). Note, that the lattice is embedded into a sphere, so the outside plaquette that we labelled twice in the braiding ladder diagram should be identified. Red and blue shadings denote the two ribbon operators, respectively. Purple circles mark the plaquette on which we perform the H_{mr}-partial charge measurement. Red circles mark the vertex on which we measure the flux.
(b) Ribbon operators for the two braiding experiments. On the last step we also draw a circle around the plaquette where we perform the H_{mr}-partial charge measurement. Note, that the lattice is embedded into a sphere, so the outside plaquette that we labelled twice for clarity should be identified.

needed to place the qubits acted on by the CZ gates adjacent to one another. Hence, reducing the number of Toffoli gates is the main goal when designing the experiments.

For the fusion of Ψ_m-fluxes on the small planar graph, we obtained a device-ready circuit of depth 70. This circuit prepares the ground state, implements the ribbon operators and performs a partial charge measurement. On the braiding ladder the same protocol leads to a much shorter circuit of depth 37. This is due to a significantly simpler ground state preparation.

Braiding. The ribbon operators for the two braiding protocols are shown in Fig. 3.9b. The qubit layout on the Sycamore chip is the same as for the fusion protocol on the ladder geometry (see Fig. 3.9a).

The circuit depths achieved for braiding the Ψ_m fluxes are 60 and 68 for the cases of $\sigma_{23}\sigma_{12}$ and $\sigma_{12}\sigma_{23}$, respectively. We performed these experiments on the double braiding ladder. This is due to constraints of the simulation. Adding 6 extra qubits needed for a triple-ladder, dramatically slows down the classical simulation run times to the point of impracticality. On a real quantum device this problem would not occur.

Results. The results of the fusion experiments on the ladder and the planar graph, as well as the braiding on the ladder are shown in Figure 3.10.

Fusion. On both lattices we measure the charge after fusion via a partial H_{mr}-measurement and see the signatures of four fusion outcomes

$$\Psi_m \otimes \Psi_m = 0 \oplus \tilde{0} \oplus \Sigma_m \oplus \tilde{\Sigma}_m,$$

corresponding to measuring no flux or r^2 flux combined with no charge ($(1,1)$-outcome) or a non-trivial charge ($(1,-1)$-outcome) identified as α_m. In the case of the small planar graph we see a significantly increased background noise due the deeper circuit used in the ground state preparation.

The number of runs for the fusion on the braiding ladder was 16000. The expected post-selection probability for the projection of the two ribbon ancilla pairs is $1/4^2 = 0.0625$, while the actual rate of success was 0.113, due to the circuit noise and measurement readout bias. The four main bins corresponding to the

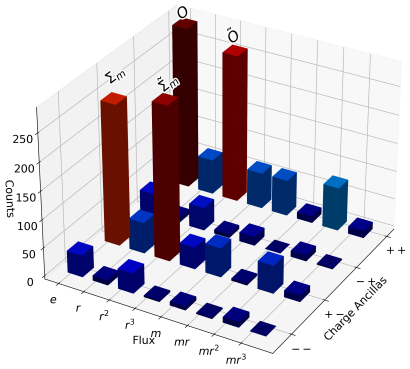

(a) The partial charge-flux measurement after fusing two Ψ_m pure fluxes on the site of fusion. The partial charge measurement was done with H_{mr} subgroup, and the geometry was that of the braiding ladder, Figure 3.5. The theoretical prediction is that the four measurement outcomes $O, \tilde{O}, \Sigma_m\tilde{\Sigma}_m$ are the only possible outcomes and occur with equal probability.

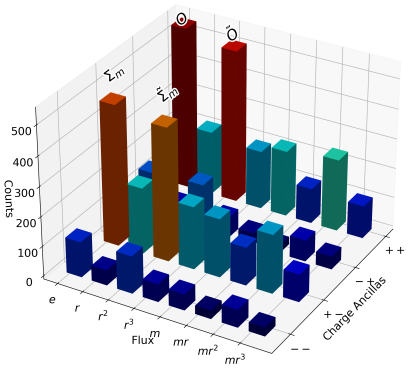

(b) The partial charge-flux measurement after fusing two Ψ_m pure fluxes on the site of fusion. The partial charge was done with H_{mr} subgroup, and the geometry was that of the small two-dimensional graph, Figure 3.6a. The theoretical prediction is that the four measurement outcomes $O, \tilde{O}, \Sigma_m\tilde{\Sigma}_m$ are the only possible outcomes and occur with equal probability.

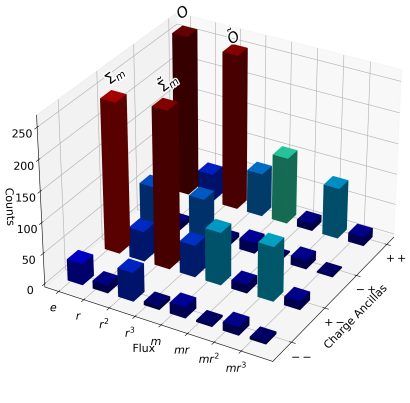

(c) The braiding on a braiding ladder: the partial charge-flux measurement after performing the braiding protocol in $\sigma_{12}\sigma_{23}$ order, Figure 3.6b (left), where σ_{ii+1} is a braid group generator. The anyons used are the pure fluxes Ψ_m. The partial charge measurement was done with respect to H_{mr} subgroup. The theoretical prediction is that the four measurement outcomes $O, \tilde{O}, \Sigma_m\tilde{\Sigma}_m$ are the only possible outcomes and occur with equal probability.

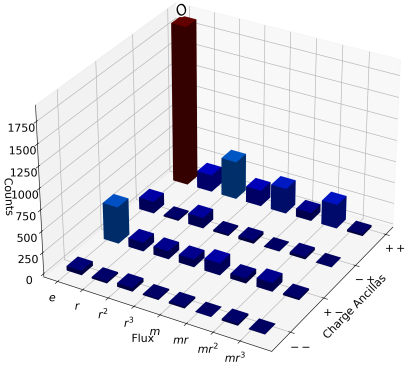

(d) The braiding on a braiding ladder: the partial charge-flux measurement after performing the braiding protocol in $\sigma_{23}\sigma_{12}$ order, Figure 3.6b (right), where σ_{ii+1} is a braid group generator. The anyons used are the pure fluxes Ψ_m. The partial charge measurement was done with respect to H_{mr} subgroup. The theoretical prediction is that the measurement outcome O is the only possible outcome.

Figure 3.10: The partial topological charge measurements for the fusion and braiding protocols.

expected topological charges count 270 ± 5 while the largest noise peak is 77 leaving us with a signal to noise ratio of approximately 3.5.

The number of runs for the fusion on the small planar graph was 64000. The expected post-selection probability for projection of the two ribbon ancilla pairs is again 0.0625, while the actual number of successes was 0.0826. The four main bins count 450 ± 7 with the biggest noise peak being 242 leaving us with a signal to noise ratio of approximately 1.9.

Braiding. Looking at the results of the charge measurement for the two braiding protocols we clearly see what we expected. The first braiding protocol results in multiple fusion outcomes while for the second braiding protocol the resulting fusion outcome is only vacuum.

The number of runs for both protocols was 16000. The expected post-selection probabilities for the two protocols are 0.0625 for $\sigma_{12}\sigma_{23}$ and 0.25 for $\sigma_{23}\sigma_{12}$, while the actual rates of successes were 0.123 for $\sigma_{12}\sigma_{23}$ and 0.315 for $\sigma_{23}\sigma_{12}$, respectively.

In the case of the first braiding we see the four main peaks corresponding to the expected topological charges counting 255 ± 5 with the biggest peak coming from the noise counting 109 and resulting in a signal to noise ratio of about 2.3. In the second case the peak corresponding to the vacuum counts 1890. The largest peak coming from the noise counts 450 giving a signal to noise ratio of about 4.2.

Supplementary measurements. In the analysis above we relied on the knowledge of the fusion outcomes to match the observed measurement outcomes of the H_{mr}-partial charge measurement with the corresponding charges.

However, we can still determine what charges the outcomes correspond to even if we do not rely on the knowledge of the fusion rules. This is done by repeating the partial charge measurements for another subgroup, as explained in Section 3.1.3.

Repeating the protocol with a H_m-partial charge measurement we see only two peaks corresponding to the charge measurement outcome $(1, 1)$ combined with no or r^2 flux. This is due to the fact that all anyons that emerge from the fusion carry either no charge or α_m charge, which both correspond to the measurement outcome $(1, 1)$ for the H_m subgroup. Given that we observed the outcomes $(1, 1)$

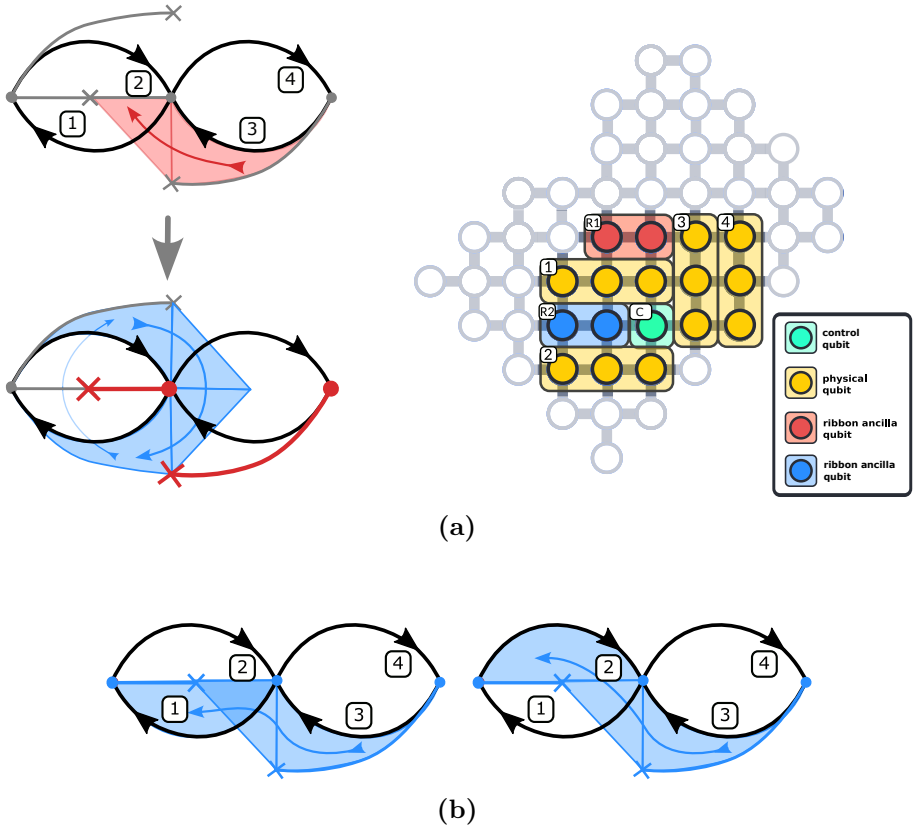

(a)

(b)

Figure 3.11: (a) (Left) The ribbon operators applied in the simulation of the S-matrix protocol. The existence or the type of the blue (equal-time) ribbon is conditioned on the state of the control qubit. (Right) The qubit layout for the interference protocols.
(b) The two ribbon paths between same sites that differ by one twist used in our path interference protocol.

and $(1, -1)$ for H_{mr}, we can conclude that the charges present are the trivial and the α_m charge (data shown in Appendix D of our Paper [2]).

3.3.2 Linking and twist matrices

In this section, we present the results of simulating the interference protocols for measuring the magnitude and the phase of the S- and T-matrix elements.

Circuit characteristics. Figure 3.11a depicts the qubit layout and the exact ribbon operators used for the S-matrix protocol.

The application or the flavour of the blue (equal-time) ribbon is conditioned on the state of the control qubit. The layout on the chip is chosen such as to reduce the number of two-qubit gates acting on the control qubit, avoiding an

accumulation of errors. This turned out to be more relevant for obtaining reliable estimates than the overall circuit depth.

For the T-matrix experiment we chose the same layout as for the S-matrix experiment and the concrete form of the ribbon is shown in Fig. 3.11b.

The depths of the circuits for the S-matrix protocol heavily depend on the anyons involved. In the following, we present in detail the circuits and results for the exemplary S-matrix elements $\tilde{S}(\Psi_m, \Psi_m) = 1$, $\tilde{S}(\Psi_m, \tilde{\Psi}_m) = -1$ and $\tilde{S}(\Psi_m, \Psi_r)$ which are of intermediate depth. For conditioning the ribbon type we have 58 for $S(\Psi_m, \Psi_m)$ and $S(\Psi_m, \tilde{\Psi}_m)$ and 64 for $S(\Psi_m, \Psi_r)$, while for conditioning the existence of the ribbon we find 84 and 90, respectively. We will return to a more detailed discussion of the circuit depths and results for all other S-matrix elements at the end of this section.

For the T-matrix elements we chose to measure $T(\Phi_r, \Phi_r) = i$, which together with $T(\tilde{\Phi}_r, \tilde{\Phi}_r) = -i$ is the most non-trivial entry corresponding to the two semions (all other anyons have topological spin ± 1). The circuit depth of 89 for this protocol is larger than for all other T-matrix elements and leads to reasonable results. Hence, we did not investigate the other T-matrix entries as they seem to be less challenging to measure.

Interference and tomography. In Section 3.2.3, we proposed an interference scheme that entangles an ancilla qubit with the space-time history of the gauge field excitations in such a way that by the end of the protocol the qubit and the field are disentangled and the qubit is left in a state that depends only on the topological properties of the spacetime history of the anyons – the S- and T-matrix elements.

The fact that the qubit is meant to be disentangled from the gauge field and any additional ancillas implies that the qubit is ideally left in a pure state. Hence, it is easy to tomograph and to extract the aforementioned topological properties. The noise in the system alters the situation. For conceptual clarity, we will thus first discuss the ideal case and subsequently comment on the effect of the noise.

The final pure state of the ancilla qubit after the ideal protocol is

$$\begin{aligned} |\psi\rangle_c &= \frac{1}{\sqrt{1+|\tilde{S}_{ab}|^2}}(|0\rangle_c + \tilde{S}_{ab}\,|1\rangle_c), \\ \rho_c &= \frac{1}{1+|\tilde{S}_{ab}|^2}\begin{pmatrix} 1 & \tilde{S}_{ab}^* \\ \tilde{S}_{ab} & |\tilde{S}_{ab}|^2 \end{pmatrix}. \end{aligned} \tag{3.29}$$

We write this density matrix in its Pauli basis

$$\rho_c = \frac{\mathbb{I} + \vec{r}\cdot\vec{\sigma}}{2}, \tag{3.30}$$

where $r_i = \mathrm{Tr}(\sigma_i \rho_c)$ is the Bloch vector and $\vec{\sigma} = (\sigma_x, \sigma_y, \sigma_z)$ is the vector of Pauli matrices and find

$$\vec{r} = \left(\frac{2\mathrm{Re}\tilde{S}_{ab}}{1+|\tilde{S}_{ab}|^2}, \frac{2\mathrm{Im}\tilde{S}_{ab}}{1+|\tilde{S}_{ab}|^2}, \frac{1-|\tilde{S}_{ab}|^2}{1+|\tilde{S}_{ab}|^2}\right). \tag{3.31}$$

Note that $|\vec{r}| = 1$ as expected for a pure state. The phase and the magnitude of $\tilde{S}_{ab}$ can be read off from the orientation of the Bloch vector only and the magnitude of $\vec{r}$ is not needed to determine $\tilde{S}_{ab}$. The magnitude is strongly affected by the noise in the system as we explain in the following.

The noise in the gates will cause entanglement between the control ancilla qubit c and the gauge field. Hence, when we tomograph the control qubit, we probe a mixed state whose Bloch vector is $|\vec{r}| < 1$. We will assume, that the noise only shortens this Bloch vector, i.e. it acts uniformly across all channels. Under this assumption, we can still read off the S-matrix elements as they only depend on the direction of the Bloch vector. Note, that this assumption is rather strong given that the generic dephasing process usually pulls the Bloch vector towards the z-axis. Nevertheless, the assumption is used in order to make the problem tractable without additional machine specific information. In an actual experiment, more elaborate error mitigation techniques and data about the noise bias could be used to replace this simple model.

Tomography. In order to determine the orientation of the Bloch vector we measure in a set of different bases. Each basis is parametrised by a vector $\vec{s}_i$ with $\sigma_{s_i} = \vec{s}_i \cdot \vec{\sigma}$ being the associated Hermitian operator.

Given a basis $\vec{s}_i$ and a Bloch vector of a mixed state $\vec{r}$, the quantum mechanical probabilities for the two measurement outcomes are

$$\begin{aligned} p_{QM}(1|\vec{s}_i,\vec{r}) &= \frac{1}{2}(1+\vec{r}\cdot\vec{s}_i)\,, \\ p_{QM}(0|\vec{s}_i,\vec{r}) &= \frac{1}{2}(1-\vec{r}\cdot\vec{s}_i)\,. \end{aligned} \tag{3.32}$$

This probability is, however, modulate by the readout bias

$$p(b|\vec{s}_i,\vec{r}) = (1-\epsilon_b)p_{QM}(b|\vec{s}_i,\vec{r}) + \epsilon_{\bar{b}}p_{QM}(\bar{b}|\vec{s}_i,\vec{r}), \tag{3.33}$$

where ϵ_b is the probability to measure the qubit in state $\bar{b}$ ($\equiv 1-b$) even though it is in the state b.

We perform the measurement $N = n_0 + n_1$ times and record the measurement outcomes (n_0, n_1) and define the estimator

$$P(\vec{s}_i) = \frac{n_1 - n_0}{N}, \tag{3.34}$$

which we call *polarisation*. Introducing $\bar{\epsilon} = (\epsilon_1 + \epsilon_0)/2, \Delta\epsilon = \epsilon_1 - \epsilon_0$ and using that

$$p(b|\vec{s}_i,\vec{r}) = \lim_{N\to\infty}\frac{n_b}{N},$$

we find

$$\lim_{N\to\infty} P(\vec{s}_i) = (1-2\bar{\epsilon})\vec{s}_i\cdot\vec{r} + \Delta\epsilon. \tag{3.35}$$

Performing a sequence of measurements for different bases $\vec{s}_i$ allows us to extract $\vec{r}$, up to a multiplicative constant, i.e., we determine its direction.

For the sake of concreteness we chose the following sets of measurements bases

1. *Equatorial Scan.* Fixing the value of the polar angle to $\theta = \pi/2$, we vary the azimuthal angle $\phi \in [0, 2\pi)$. From this scan we extract $\phi_{\max}$ which has the largest polarisation.

2. *Meridian Scan.* Fixing the value of the azimuthal angle to $\phi = \phi_{\max}$, we scan the polar angle $\theta \in [0, 2\pi)$[13] From this scan we extract $\theta_{\max}$ which has the largest polarisation.

[13]The domain is extended on purpose.

The extraction of the relevant angles is done by fitting Eq. (3.35). The two angles then fix the value of $\tilde{S}_{ab}$ via

$$\tilde{S}_{ab} = \sqrt{\frac{1-\cos\theta_{\max}}{1+\cos\theta_{\max}}} e^{i\phi_{\max}}.$$

The other two parameters, the amplitude and the offset of the polarisation, do not convey any physical information. The offset determines the difference of the effective readout biases, $\Delta\epsilon$, and the amplitude determines the product of the mean readout bias and the length of the Bloch vector, $(1-2\bar{\epsilon})|\vec{r}|$.

In the discussion above, we have neglected the fact that in addition to the measurement of the control qubit, we measure the ribbon ancillas and post-select on their biased measurement outcomes. This causes an increased observed effective readout bias $\Delta\epsilon$, obtained from the fitting procedure described in the last section, which exceeds the $\Delta\epsilon$ estimate from calibration data. A more detailed discussion of this issue is given in Appendix E of our Paper [2].

For the T-matrix protocol the Bloch vector of the control qubit after performing the ideal circuit reads

$$\vec{r} = (\mathrm{Re}T_{aa}, \mathrm{Im}T_{aa}, 0)\,. \tag{3.36}$$

We perform the same type of tomography to estimate $\vec{r}$ and calculate the magnitude and phase of T_{aa} via the equation above.

Results. The numerical results for the interference protocols determining S_{ab} with $a = \Psi_m$ and $b = \Psi_m, \tilde{\Psi}_m, \Psi_r$ are shown in Fig. 3.12. The first three panels show the results of the protocol in which the type of the second ribbon is conditioned to be Ψ_b or $0 \oplus \tilde{0}$ (cf. Fig. 3.7c), while the last one shows the results for conditioning the existence of the ribbon (cf. Fig. 3.7b). In both cases we note a systematic drift of the Bloch vector towards the z-axis. The magnitude of the S-matrix element is dictated by the angle of the Bloch vector with the z-axis and hence this drift leads to an underestimation of $|\tilde{S}_{ab}|$. The systematic drift is significantly less dramatic in the case of the first protocol, i.e., conditioning on Ψ_b or $0 \oplus \tilde{0}$. Hence, the estimate of the magnitudes of the S-matrix elements is much closer to the theoretical value.

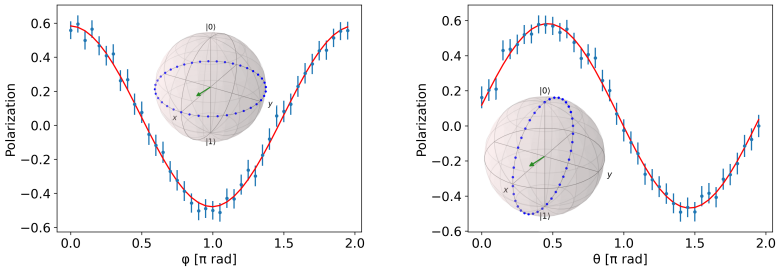

(a) $\tilde{S}(\Psi_m, \Psi_m) = 0.89(1)e^{i\pi 0.004(4)}$ measured, $\tilde{S}(\Psi_m, \Psi_m) = 1$ predicted.

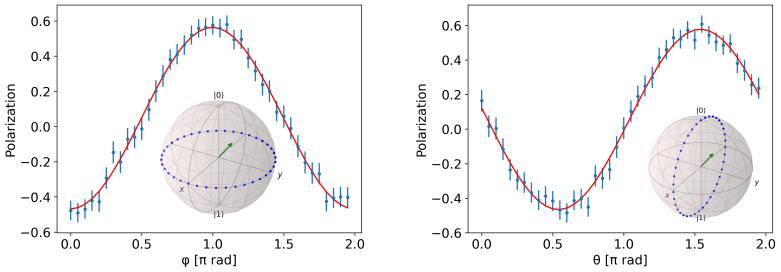

(b) $\tilde{S}(\Psi_m, \tilde{\Psi}_m) = 0.88(1)e^{i\pi 0.998(5)}$ measured, $\tilde{S}(\Psi_m, \tilde{\Psi}_m) = -1$ predicted.

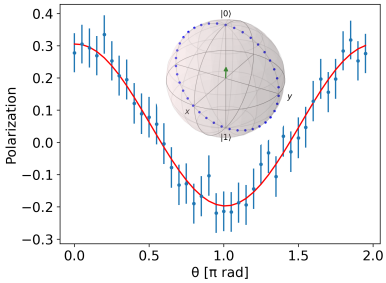

(c) $\tilde{S}(\Psi_m, \Psi_r) = 0.02(2)$ measured, $\tilde{S}(\Psi_m, \Psi_r) = 0$ predicted. ϕ-scan omitted, since $\theta = \pi$.

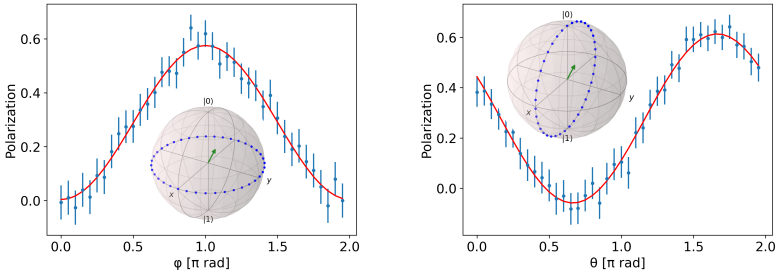

(d) $\tilde{S}(\Psi_m, \tilde{\Psi}_m) = 0.58(1)e^{i\pi 1.002(8)}$ measured, $\tilde{S}(\Psi_m, \tilde{\Psi}_m) = 1$ predicted.

Figure 3.12: Numerical results of the control qubit tomography for the S-matrix interference protocol (a)-(c) conditioning the type of the equal time ribbon (cf. Figure 3.7c) and (d) conditioning its existence (cf. Figure 3.7b). The measurement basis was scanned across two planes, see the Bloch sphere diagram (blue dotted circles). The polarisation P was estimated from these measurements by fitting Eq. (3.35). It yields the Bloch vector of ρ_c (green arrow) and $\tilde{S}_{ab}$.

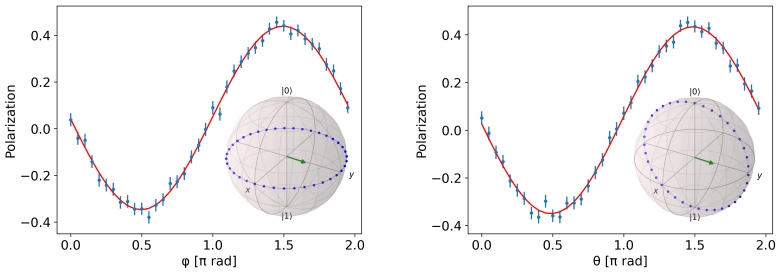

Figure 3.13: Numerical results of the control qubit tomography for the T-matrix interference protocol where the paths of the ribbon was conditioned (cf. Figure 3.8a). Tomography performed as for the S-matrix (cf. Fig.3.12). $T(\tilde{\Phi}_r, \tilde{\Phi}_r) = 1.04(1)e^{i\pi 1.496(4)}$ measured, $T(\tilde{\Phi}_r, \tilde{\Phi}_r) = -i$ predicted.

This is due to the fact that the circuit implementing this protocol is much shallower due to the simpler forms of the conditional ribbon operators, one Toffoli gate less in the conditional multiplication circuit, cf. Figure 3.4d. The phases of all measured $\tilde{S}_{ab}$ are estimated well and agree with the theoretically predicted values.

The result for the T-matrix element $T(\tilde{\phi}_r, \tilde{\phi}_r)$ determined by the path conditioning protocol in Figure 3.8a is shown in Figure 3.13 and agrees with the theoretical value.

Uncertainty. In the experiment we used 1000 shots per measurement basis for the S-matrix measurements and 5000 for the T-matrix measurements. See Appendix E of our Paper [2], to see how we estimated the final uncertainties in the measured braiding amplitudes, i.e., S- and T-matrix elements, as well as for each datapoint in our plots.

We expected a post selection probability of 1/4 for all T-matrix protocols and S-matrix protocols with measured $|S| \neq 0$. For the case of measured $|S| = 0$ the probability drops to 1/8. These probabilities were observed in the numerical experiment.

Other S-Matrix elements. As stated above some anyon ribbons are harder to compile than others. The bottleneck of this anyon interference protocol is the difficulty of the conditioned ribbon.

We can divide the S-matrix protocols into six different difficulty classes measured by the depth of the required circuits. The biggest factor determining those is whether for the anyon in question, (C, χ) obeys $\chi(r^2) = \chi(e)$. If this is not the case, the representation $A(g)$ is faithful. This means that all group elements

must be included in the circuit which requires many SWAP gates and increases the circuit depth significantly.

The second factor to consider is the number of Toffoli gates in the controlled multiplication and generalised conjugation circuits. The semions $\Phi_r, \tilde{\Phi}_r$ are difficult in both regards.

In Fig. 3.14 we show the S-matrix with all its entries color coded according to the difficulty class. In the list below we present the circuit depths and numerical simulation results for the diagonal S-matrix elements for representative cases of all six difficulty classes. For all protocols, except for 1. and 4., we chose to condition the ribbon b vs $0 \oplus \tilde{0}$ rather than ribbon b vs $0 \oplus 0$.

Summary of the S-matrix results

1. Conditioning an abelian anyon: $\tilde{S}(\Sigma_m, \Sigma_m) = 0.969(6)e^{i\pi 0.004(2)}$, theoretical prediction $\tilde{S}(\Sigma_m, \Sigma_m) = 1$. The total compiled circuit depth is 23 with 0 Toffoli gates corresponding to the difficulty class shaded in green in Fig. 3.14.

2. Conditioning a m- or mr-dyon with $\chi(r^2) = 1$: $\tilde{S}(\Psi_m, \Psi_m) = 0.89(1)e^{i\pi 0.004(4)}$, theoretical prediction $\tilde{S}(\Psi_m, \Psi_m) = 1$. The total compiled circuit depth is 58 with 2 Toffoli gates corresponding to the difficulty class shaded in light green in Fig. 3.14.

3. Conditioning a r-dyon with $\chi(r^2) = 1$: $\tilde{S}(\Psi_r, \Psi_r) = 0.82(1)e^{i\pi 0.001(4)}$, theoretical prediction $\tilde{S}(\Psi_r, \Psi_r) = 1$. The total compiled circuit depth is 77 with 4 Toffoli gates corresponding to the difficulty class shaded in yellow in Fig. 3.14.

4. Conditioning a non-abelian charge: $\tilde{S}(\Sigma_\epsilon, \Sigma_\epsilon) = 0.123(8)e^{i\pi 0.01(2)}$, theoretical prediction $\tilde{S}(\Sigma_\epsilon, \Sigma_\epsilon) = 1$. The total compiled circuit depth is 125 with 4 Toffoli gates corresponding to the difficulty class shaded in light orange in Fig. 3.14.

5. Conditioning a m- or mr-dyon with $\chi(r^2) = -1$: $\tilde{S}(\Phi_m, \Phi_m) = 0.19(2)e^{i\pi 0.04(4)}$, theoretical prediction $\tilde{S}(\Phi_m, \Phi_m) = 1$. The total compiled circuit depth is 133 with 4 Toffoli gates corresponding to the difficulty class shaded in orange in Fig. 3.14.

6. Conditioning a r-dyon with $\chi(r^2) = -1$ (semions): $\tilde{S}(\Phi_r, \Phi_r) = 0.06(1)e^{i\pi 1.0(3)}$, theoretical prediction $\tilde{S}(\Phi_r, \Phi_r) = -1$. The total compiled circuit depth is 171 with 6 Toffoli gates corresponding to the difficulty class shaded in red in Fig. 3.14.

$$S = \frac{1}{8}$$

	0	$\tilde{0}$	Σ_m	$\tilde{\Sigma}_m$	Σ_r	$\tilde{\Sigma}_r$	Σ_{mr}	$\tilde{\Sigma}_{mr}$	Ψ_m	$\tilde{\Psi}_m$	Ψ_{mr}	$\tilde{\Psi}_{mr}$	Ψ_r	$\tilde{\Psi}_r$	Σ_ϵ	$\tilde{\Sigma}_\epsilon$	Φ_m	$\tilde{\Phi}_m$	Φ_{mr}	$\tilde{\Phi}_{mr}$	Φ_r	$\tilde{\Phi}_r$
0	1	1	1	1	1	1	1	1	2	2	2	2	2	2	2	2	2	2	2	2	2	2
$\tilde{0}$	1	1	1	1	1	1	1	1	2	2	2	2	2	2	−2	−2	−2	−2	−2	−2	−2	−2
Σ_m	1	1	**1**	1	1	1	1	1	−2	−2	−2	−2	2	2	2	2	−2	−2	−2	−2	2	2
$\tilde{\Sigma}_m$	1	1	1	1	1	1	1	1	−2	−2	2	2	−2	−2	2	2	−2	−2	2	2	−2	−2
Σ_r	1	1	1	1	1	1	1	1	2	2	−2	−2	−2	−2	2	2	2	2	−2	−2	−2	−2
$\tilde{\Sigma}_r$	1	1	1	1	1	1	1	1	−2	−2	−2	−2	2	2	−2	−2	2	2	2	2	−2	−2
Σ_{mr}	1	1	1	1	1	1	1	1	−2	−2	2	2	−2	−2	−2	−2	2	2	−2	−2	2	2
$\tilde{\Sigma}_{mr}$	1	1	1	1	1	1	1	1	2	2	−2	−2	−2	−2	−2	−2	−2	−2	2	2	2	2
Ψ_m	2	2	−2	−2	2	−2	−2	2	**4**	**−4**	0	0	**0**	0	0	0	0	0	0	0	0	0
$\tilde{\Psi}_m$	2	2	−2	−2	2	−2	−2	2	**−4**	4	0	0	0	0	0	0	0	0	0	0	0	0
Ψ_{mr}	2	2	−2	2	−2	−2	2	−2	0	0	4	−4	0	0	0	0	0	0	0	0	0	0
$\tilde{\Psi}_{mr}$	2	2	−2	2	−2	−2	2	−2	0	0	−4	4	0	0	0	0	0	0	0	0	0	0
Ψ_r	2	2	2	−2	−2	2	−2	−2	**0**	0	0	0	**4**	−4	0	0	0	0	0	0	0	0
$\tilde{\Psi}_r$	2	2	2	−2	−2	2	−2	−2	0	0	0	0	−4	4	0	0	0	0	0	0	0	0
Σ_ϵ	2	−2	2	2	2	−2	−2	−2	0	0	0	0	0	0	**4**	−4	0	0	0	0	0	0
$\tilde{\Sigma}_\epsilon$	2	−2	2	2	2	−2	−2	−2	0	0	0	0	0	0	−4	4	0	0	0	0	0	0
Φ_m	2	−2	−2	−2	2	2	2	−2	0	0	0	0	0	0	0	0	**4**	−4	0	0	0	0
$\tilde{\Phi}_m$	2	−2	−2	−2	2	2	2	−2	0	0	0	0	0	0	0	0	−4	4	0	0	0	0
Φ_{mr}	2	−2	−2	2	−2	2	−2	2	0	0	0	0	0	0	0	0	0	0	4	−4	0	0
$\tilde{\Phi}_{mr}$	2	−2	−2	2	−2	2	−2	2	0	0	0	0	0	0	0	0	0	0	−4	4	0	0
Φ_r	2	−2	2	−2	−2	−2	2	2	0	0	0	0	0	0	0	0	0	0	0	0	**−4**	4
$\tilde{\Phi}_r$	2	−2	2	−2	−2	−2	2	2	0	0	0	0	0	0	0	0	0	0	0	0	4	−4

Figure 3.14: The S-matrix of the $D(D_4)$ theory. The color shading represents the difficulty to observe the values experimentally, where green to red denotes increasing difficulty. For the entries highlighted in bold face and blue we numerically obtained the values by simulating the phase-sentitive measurement protocols.

We assume that the first element is conditioned and largely determines the circuit depth while the specific choice of the other, unconditioned ribbon operator only mildly influences the depth. This means that the difficulty is set by the row of the S-matrix and one can use the symmetry of the S-matrix to pick the better of the two interference procedures. For example for measuring $S(\Phi_r, \Sigma_m)$ one would condition the Σ_m ribbon and not the semion Φ_r.

We observe that the magnitude of the S-matrix in the simulation results decays strongly with the circuit depth. This is due to accumulating errors on the control qubit. We speculate that the main error channel responsible for the drift of the estimated angle $\theta_{\max}$, and hence the braiding amplitude, is dephasing. Dephasing reduces the r_x and r_y components of the Bloch vector, while keeping r_z fixed, so any error in estimating this angle due to any small offset $\delta r_z \neq 0$ will be amplified. On the upside, this error channel does not change the ratio between r_x and r_y and hence the braiding phase estimates are well within the theoretical values.

3.4 Chapter Summary

In this chapter, I have presented the work I have done on the topic of quantum simulation of non-abelian anyon braiding. In particular, I would emphasise the two main technical developments; protocols for anyon braiding and charge measurement. These protocols do not require feedforward techniques, something that most NISQ devices at the time of writing did not have, one of the first examples being `Quantinuum`'s trapped ion device[71]. Nevertheless, even as new devices are introduced with the feedforward capability, not relying on them extensively is good for the performance, given the general overhead of the qubit read-out. Of course, our reliance on the limited amount of post-selection can be alleviated by feedforward techniques, and hence we are positioned complementary and not antagonistically to these new developments. This is especially true for ground state preparation, preparing the ground state via measure-feedforward methods[76] and then performing experiments using our protocols is a natural way to synergise.

We also propose anyon interference experiments that are more advance than the current state of the literature, with our numerics demonstrating that we have access to much of the anyon theory modular data. In general, our numerics makes us optimistic about observing non-abelian anyon phenomenology on NISQ simulators; and this is without any type of error mitigation and gate optimisation techniques that are readily used in experiments such as these[14–16, 68–70].

What I call further attention to is the topological charge measurement. We presented a feasible (according to our numerics) protocol for the first direct measurement of the topological charge, not to be confused with ground state checks of Ref. [71]. This is an important ingredient for making quantum computation with quantum double excitations universal[74][14]. I believe that this positions our work well in the exciting and thriving field of realising topological quantum orders on NISQ devices[68–71, 73, 139].

[14]However, not in our exemplar case of $G = D_4$, but $G = S_3$ would be universal.

3.A Ribbon types

In this appendix, we present all variants of the elementary triangles that constitute the ribbon operators introduced in Section 3.1.2. Apart from the main distinction into type I and type II triangles which correspond to controlled group multiplication and controlled generalised conjugation, respectively, there are different variants of the concrete operation which depend on how exactly we couple the ancilla qudit with the gauge field degrees of freedom.

In the main text we have chose one particular case to keep the description of the algorithm readable. In this section, we provide an exhaustive list of all sixteen variants (8 per type). All triangles can be freely rotated and we chose to rotate them such that the lattice edge of type I triangles is the bottom edge, and such that type II triangles stand on their tip. The triangles are then further distinguished by whether the triangle is appended to the front end or the back end of the ribbon, i.e., involving the ancilla qubit a_f or a_b, by the orientation of the lattice edge and by the direction of extension (being aligned or anti-aligned with the lattice edge orientation). All operators are shown explicitly in Figure 3.15.

The controlled group multiplication U_{CM} of type I triangles is given by – depending on these specifications – right or left multiplication with the group element c encoded by the forward or backward ancilla a_f or a_b or its inverse c^{-1}.

For type II triangles we need to apply different variants of generalised conjugation U_{GC}. In the main text in Section 3.1.2 we defined the generalised conjugation as $U_{GC}^{(C,\chi)} : |c,i\rangle\,|h\rangle_{\text{phys}} \to |hch^{-1}\rangle\,\Gamma_c^\chi(h)\,|i\rangle\,|h\rangle_{\text{phys}}$, where $\Gamma_c^\chi(g)$ are matrices defined by the representation of the algebra (C,χ) spanned by basis vectors $|c,i\rangle$. In this form it is obvious why we call this operation generalised conjugation, however, this operator is more conveniently defined by the (C,χ)-representation matrices $A(h)$ defined in Section 3.1.1. To make the connection between the two, we unify the two indices of the (C,χ)-representation into one multi index $|c,i\rangle \equiv |\mu\rangle$ and identify $|c,i\rangle \to |hch^{-1}\rangle\,\Gamma_c^\chi(h)\,|i\rangle$ with $|\mu\rangle \to A^{(C,\chi)}(h)\,|\mu\rangle$. The superscript (C,χ) is dropped, if no confusion arises. The different type II triangle variants then implement $A(h)$ or $A(h^{-1})$ or their transpose to the ancilla qubits a_f or a_b.

$$U_{CM} \left|c', i'\right\rangle_{a_b} \left|c, i\right\rangle_{a_f} \left|g_i\right\rangle_{\text{phys}} =$$

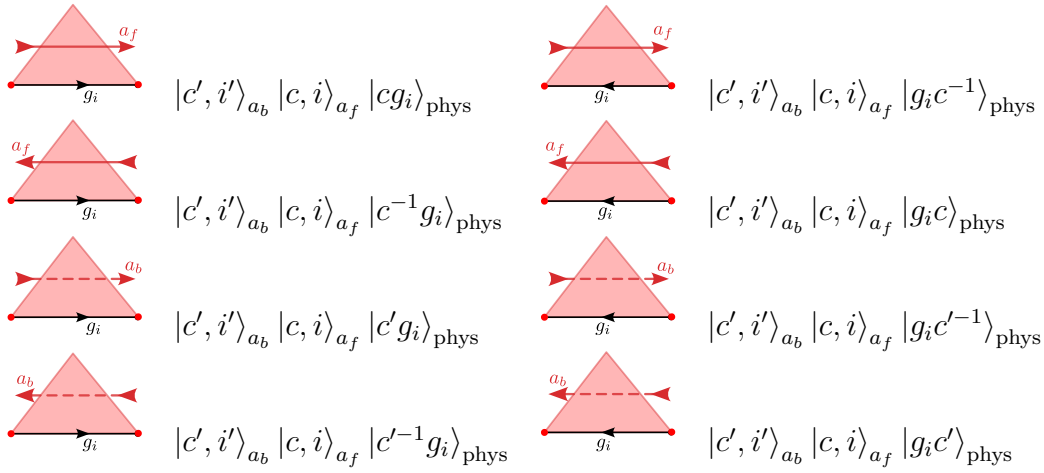

$$U_{GC} \left|\alpha'\right\rangle_{a_b} \left|\alpha\right\rangle_{a_f} \left|h_i\right\rangle_{\text{phys}} =$$

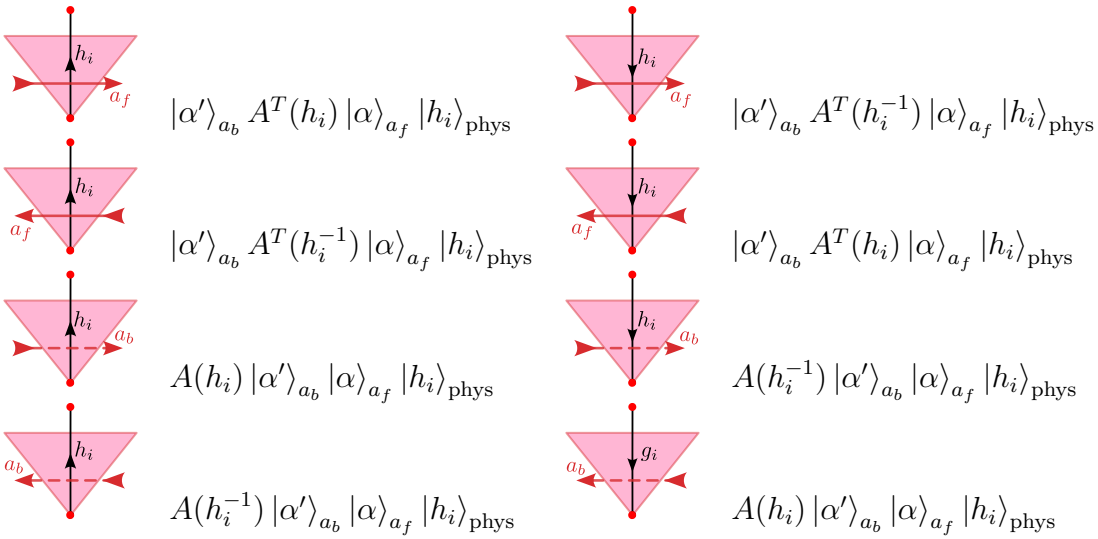

Figure 3.15: The 16 variants of the elementary triangles of type I (top) and type II (bottom).

3.B Representation theory of $D(D_4)$

In this appendix, we cover the representation theory, viz. the anyon content, of the quantum double algebra of D_4. Figure 3.16a below shows the naming convention of the anyons and Figure 3.16b lists the corresponding representation matrices used for the generalised conjugation.

The (abelian) fusion algebra of the excitations of this theory is highly symmetrical and can be broken down into a set of rules listed below. For writing down these rules we introduce the function $\lfloor\rfloor : G \to \{e, m, r, mr\} \equiv G/Z(G)$ that divides out r^2 and use the notation $\Sigma_e \equiv 0$.

Fusion rules of $D(D_4)$

1. Fusion with the vacuum: $0 \otimes a = a$.
2. Fusion with the trivial flux $\tilde{0}$:
   (a) $\tilde{0} \otimes \tilde{0} = 0$,
   (b) $\tilde{0} \otimes \Sigma_x = \tilde{\Sigma}_x$, $x \in \{m, r, mr, \epsilon\}$,
   (c) $\tilde{0} \otimes \Psi_x = \Psi_x$ and $\tilde{0} \otimes \Phi_x = \tilde{\Phi}_x$, $x \in \{m, r, mr\}$.
3. Fusion with abelian charges Σ_x, $x \in \{m, r, mr\}$:
   (a) $\Sigma_x \otimes \Sigma_y = \Sigma_{\lfloor xy \rfloor}$, $y \in \{m, r, mr\}$,
   (b) $\Sigma_x \otimes \Sigma_\epsilon = \Sigma_\epsilon$,
   (c) $\Sigma_x \otimes \Psi_y = \delta_{xy}\Psi_y \oplus (1 - \delta_{xy})\tilde{\Psi}_y$,
   (d) $\Sigma_x \otimes \Phi_y = \delta_{xy}\Phi_y \oplus (1 - \delta_{xy})\tilde{\Phi}_y$,
4. Fusion with non-abelian charge Σ_ϵ:
   (a) $\Sigma_\epsilon \otimes \Sigma_\epsilon = 0 \oplus \Sigma_m \oplus \Sigma_r \oplus \Sigma_{mr}$,
   (b) $\Sigma_\epsilon \otimes \Psi_x = \Phi_x \oplus \tilde{\Phi}_x$ and $\Sigma_\epsilon \otimes \Phi_x = \Psi_x \oplus \tilde{\Psi}_x$, for $x \in \{m, r, mr\}$.
5. Fusion with dyons of nontrivial flux $x \in \{m, r, mr\}$:
   (a) $\Psi_x \otimes \Psi_x = \tilde{\Psi}_x \otimes \tilde{\Psi}_x = 0 \oplus \tilde{0} \oplus \Sigma_x \oplus \tilde{\Sigma}_x$ and $\Psi_x \otimes \tilde{\Psi}_x = \bigoplus_{y \in \{m,r,mr\}} (1 - \delta_{xy})\Sigma_y \oplus \tilde{\Sigma}_y$,
   (b) $\Psi_x \otimes \Phi_x = \Sigma_\epsilon \oplus \tilde{\Sigma}_\epsilon$,
   (c) $\Phi_x \otimes \Phi_x = 0 \oplus \Sigma_x \oplus (\bigoplus_{y \in \{m,r,mr\}} (1 - \delta_{xy})\tilde{\Sigma}_y)$,

(d) $\Psi_x \otimes \Psi_y = \Psi_{\lfloor xy \rfloor} \oplus \tilde{\Psi}_{\lfloor xy \rfloor}$ and $\Psi_x \otimes \Phi_y = \Phi_{\lfloor xy \rfloor} \oplus \tilde{\Phi}_{\lfloor xy \rfloor}$, for $x \neq y$ and $y \in \{m, r, mr\}$,

(e) $\Phi_x \otimes \Phi_y = \Psi_{\lfloor xy \rfloor} \oplus \tilde{\Psi}_{\lfloor xy \rfloor}$, for $x \neq y$ and $y \in \{m, r, mr\}$.

In the fusion rules stated so far, we have omitted several rules where one or both of the anyons carry a tilde symbol. Note, that while for the pure charges, the tilde symbol is meaningful and distinguishes between the two conjugacy classes defined for the two elements of the centralizer C_e and C_{r^2}, the convention of naming the four dyons for the other conjugacy classes as $\Psi, \tilde{\Psi}, \Phi, \tilde{\Phi}$ is somewhat arbitrary (cf. Figure 3.16a). Nevertheless, the additional fusion rules involving the tilde anyons can be derived from the ones above by (multiple) application of a simple rule. To state this rule, we note that for any anyon X the anyon $\tilde{X}$ can be read off from Figure 3.16a. For convenience, we also define $\tilde{\tilde{X}} = X$. The rule can then be given as follows. Pick one anyon X on the LHS ($\otimes$-side) and replace X by $\tilde{X}$. For all elements X_i in the direct sum $\oplus_i X_i$ on the RHS, replace X_i by $\tilde{X}_i$.

Note that this prescription is only suitable to derive the rules not explicitly stated above. In particular, it is *not* a symmetry (or a $\mathbb{Z}_2$-grading) of the algebra and is not true for pairs involving Ψ_x and $\tilde{\Psi}_x$, for $x \in \{m, r, mr\}$, as can be seen from 5(a) above.

3.C Elementary circuits for the case of $D(D_4)$

In Appendix 3.A, we have presented all the elementary operations associated with the application of the ribbon operators and in Section 3.1, the other elementary operations used for charge measurements and ground state preparation. In Section 3.1.4 we have spelled out some of the above mentioned operations for the actual group element-to-qubit encoding used in our simulations of the protocols. In this Appendix, we present the concrete circuit elements for all relevant operations.

$D(D_4)$	O	Σ_r	Σ_{mr}	Σ_m	Σ_ϵ	$\tilde{O}$	$\tilde{\Sigma}_r$	$\tilde{\Sigma}_{mr}$	$\tilde{\Sigma}_m$	$\tilde{\Sigma}_\epsilon$
$\mathcal{C}$	$\mathcal{C}_e$					$\mathcal{C}_{r^2}$				
χ	1	α_r	α_{mr}	α_m	ϵ	1	α_r	α_{mr}	α_m	ϵ
T	1	1	1	1	1	1	1	1	1	-1
dim d	1	1	1	1	2	1	1	1	1	2

$D(D_4)$	Ψ_m	$\tilde{\Psi}_m$	Φ_m	$\tilde{\Phi}_m$	Ψ_{mr}	$\tilde{\Psi}_{mr}$	Φ_{mr}	$\tilde{\Phi}_{mr}$
$\mathcal{C}$	$\mathcal{C}_m$				$\mathcal{C}_{mr}$			
χ	$(1,1)$	$(1,-1)$	$(-1,1)$	$(-1,-1)$	$(1,1)$	$(1,-1)$	$(-1,1)$	$(-1,-1)$
T	1	-1	1	-1	1	-1	1	-1
dim d	2	2	2	2	2	2	2	2

$D(D_4)$	Ψ_r	Φ_r	$\tilde{\Psi}_r$	$\tilde{\Phi}_r$
$\mathcal{C}$	$\mathcal{C}_r$			
χ	1	i	-1	$-i$
T	1	i	-1	$-i$
dim d	2	2	2	2

(a)

$A(g)$	e	r	r^2	r^3	m	mr	mr^2	mr^3
O	1	1	1	1	1	1	1	1
$\tilde{O}$	1	1	1	1	1	1	1	1
Σ_r	1	1	1	1	-1	-1	-1	-1
Σ_{mr}	1	-1	1	-1	-1	1	-1	1
Σ_m	1	-1	1	-1	1	-1	1	-1
$\tilde{\Sigma}_r$	1	1	1	1	-1	-1	-1	-1
$\tilde{\Sigma}_{mr}$	1	-1	1	-1	-1	1	-1	1
$\tilde{\Sigma}_m$	1	-1	1	-1	1	-1	1	-1
Σ_ϵ	$\mathbb{1}$	$-i\sigma_y$	$-\mathbb{1}$	$i\sigma_y$	σ_z	$-\sigma_x$	$-\sigma_z$	σ_x
$\tilde{\Sigma}_\epsilon$	$\mathbb{1}$	$-i\sigma_y$	$-\mathbb{1}$	$i\sigma_y$	σ_z	$-\sigma_x$	$-\sigma_z$	σ_x
Ψ_r	$\mathbb{1}$	$\mathbb{1}$	$\mathbb{1}$	$\mathbb{1}$	σ_x	σ_x	σ_x	σ_x
Φ_r	$\mathbb{1}$	$i\sigma_z$	$-\mathbb{1}$	$-i\sigma_z$	σ_x	σ_y	$-\sigma_x$	$-\sigma_y$
$\tilde{\Psi}_r$	$\mathbb{1}$	$-\mathbb{1}$	$\mathbb{1}$	$-\mathbb{1}$	σ_x	$-\sigma_x$	σ_x	$-\sigma_x$
$\tilde{\Phi}_r$	$\mathbb{1}$	$-i\sigma_z$	$-\mathbb{1}$	$i\sigma_z$	σ_x	$-\sigma_y$	$-\sigma_x$	σ_y
Ψ_m	$\mathbb{1}$	σ_x	$\mathbb{1}$	σ_x	$\mathbb{1}$	σ_x	$\mathbb{1}$	σ_x
$\tilde{\Psi}_m$	$\mathbb{1}$	σ_x	$\mathbb{1}$	σ_x	$-\mathbb{1}$	$-\sigma_x$	$-\mathbb{1}$	$-\sigma_x$
Φ_m	$\mathbb{1}$	$i\sigma_y$	$-\mathbb{1}$	$-i\sigma_y$	σ_z	σ_x	$-\sigma_z$	$-\sigma_x$
$\tilde{\Phi}_m$	$\mathbb{1}$	$i\sigma_y$	$-\mathbb{1}$	$-i\sigma_y$	$-\sigma_z$	$-\sigma_x$	σ_z	σ_x
Ψ_{mr}	$\mathbb{1}$	σ_x	$\mathbb{1}$	σ_x	σ_x	$\mathbb{1}$	σ_x	$\mathbb{1}$
$\tilde{\Psi}_{mr}$	$\mathbb{1}$	σ_x	$\mathbb{1}$	σ_x	$-\sigma_x$	$-\mathbb{1}$	$-\sigma_x$	$-\mathbb{1}$
Φ_{mr}	$\mathbb{1}$	$i\sigma_y$	$-\mathbb{1}$	$-i\sigma_y$	$-\sigma_x$	σ_z	σ_x	$-\sigma_z$
$\tilde{\Phi}_{mr}$	$\mathbb{1}$	$i\sigma_y$	$-\mathbb{1}$	$-i\sigma_y$	σ_x	$-\sigma_z$	$-\sigma_x$	σ_z

(b)

Figure 3.16: (a) Anyon content of $D(D_4)$ defined by flux-charge pairs $(\mathcal{C}, \chi)$, listing the topological spin as given by the (diagonal) T-matrix entry and the quantum dimension d. (b) A_g matrices for every representation of $D(D_4)$.

Controlled multiplication. There are four kinds of controlled multiplications that appear in all of our elementary protocols

$$U_{CM}^{(1)} : |g,h\rangle \to |g,gh\rangle\,, \quad U_{CM}^{(2)} : |g,h\rangle \to |g,hg\rangle\,,$$
$$U_{CM}^{(3)} : |g,h\rangle \to |g,g^{-1}h\rangle\,, \quad U_{CM}^{(4)} : |g,h\rangle \to |g,hg^{-1}\rangle\,. \quad (3.37)$$

Depending on the context in which it appears, i.e., weather the controlled multiplication is a part of the ground state preparation, the partial charge measurement or the ribbon operator application, the controlling group element g is unrestricted $g \in G$ or is restricted to one of the subgroups $\{H_m, H_r, H_{mr}\}$ or one of the conjugacy classes $\{C_m, C_r, C_{mr}\}$. As mentioned in the main text, the circuits for the latter two cases are drastically simplified compared to the unrestricted case. The circuits for all cases above are shown in Figure 3.17.

Generalised conjugation. Another building block of our circuits is the generalised conjugation, $U_{GC}\,|g\rangle\,|\alpha\rangle_{a_i} = |g\rangle\,A^T(g)\,|\alpha\rangle_{a_i}$. The A-matrices for $D(D_4)$, are shown in Appendix 3.B. In Appendix 3.A we see that we need four variants of the map: $A(g)$, $A(g^{-1})$, $A^T(g)$, $A^T(g^{-1})$. Figure 3.18 shows the corresponding circuits which are to be supplemented by the appropriate unitaries from Figure 3.16b.

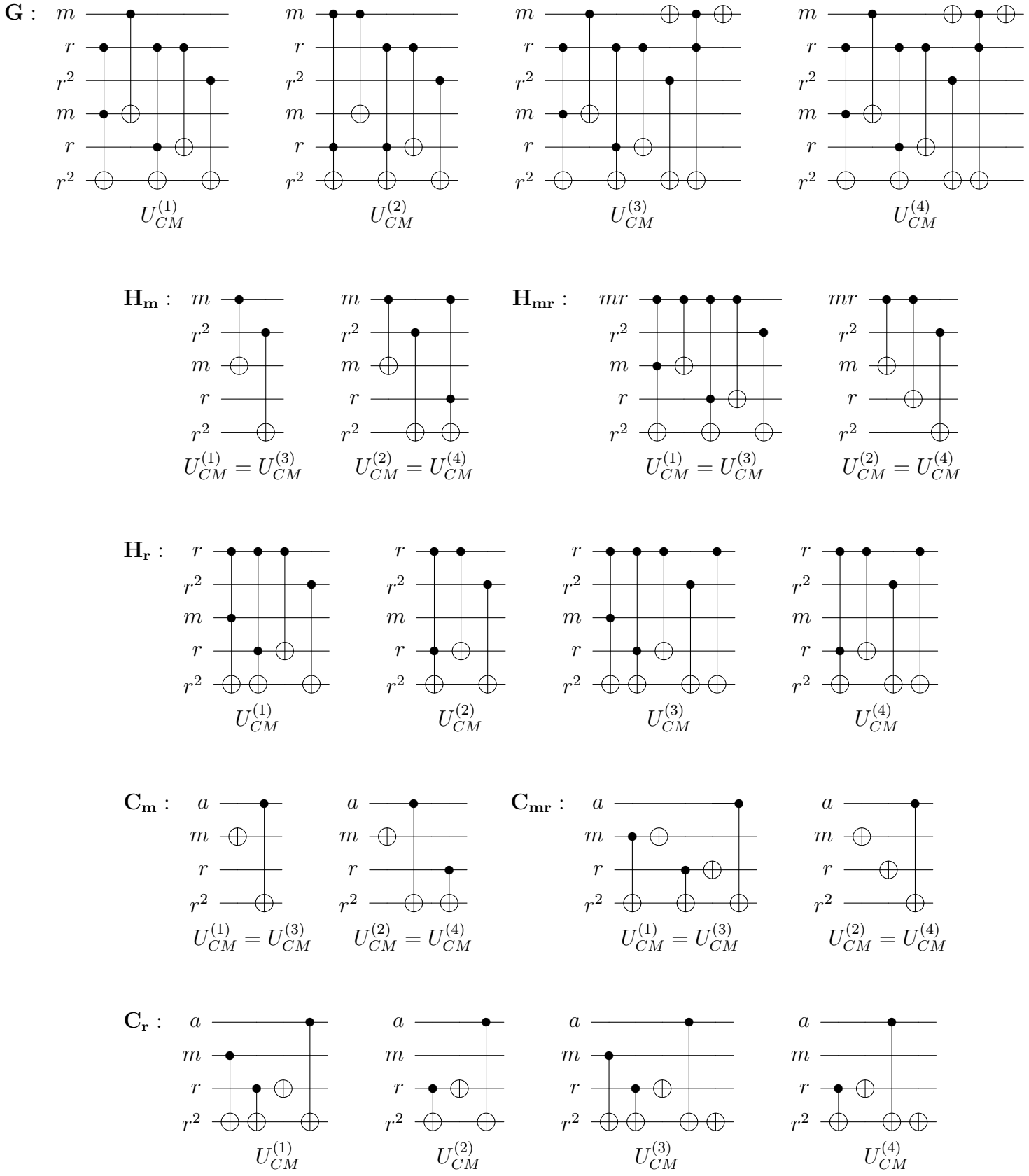

Figure 3.17: The circuits implementing the controlled group multiplications U_{CM} defined in Eq. (3.37) for $g \in G$ (unrestricted), g restricted to subgroups H and g restricted to conjugacy classes C.

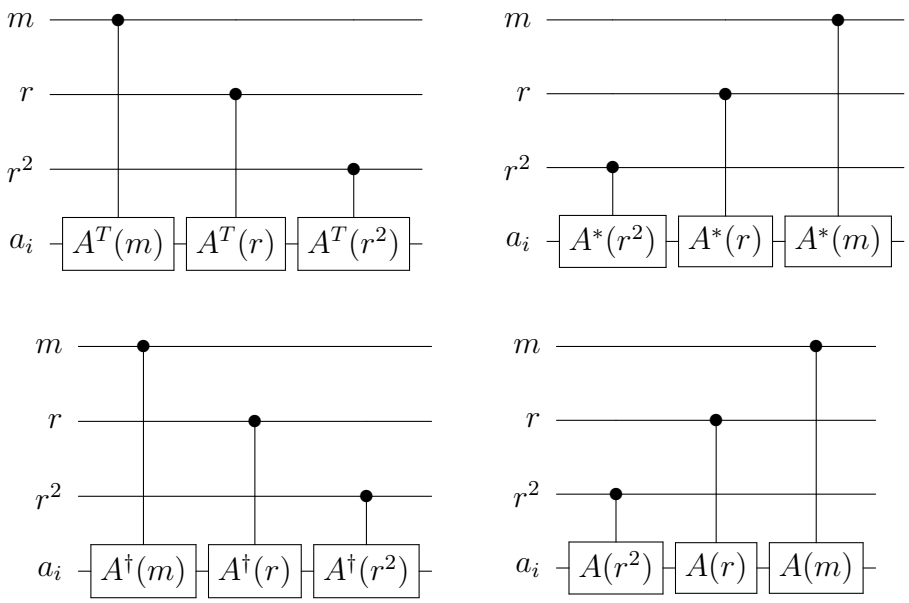

Figure 3.18: The four variants ($A^T(g)$, $A^T(g^{-1})$, $A(g^{-1})$ and $A(g)$, left to right top to bottom, respectively) of the generalised conjugation circuits. Depending on the label (C, χ) of the ribbon operator the appropriate single qubit unitaries from Table 3.16b are inserted.

3.D $F-$ and $R-$Symbols in Quantum Double Models

In this appendix, I aim to supplement the literature on the quantum double algebras by providing my explicit calculations of the F- and R-symbols for the representations of quantum double algebras, since I have not found any complete account in 'my time of need'.

To remind the reader of the definitions introduced in Section 3.1.1, irreducible representations of the quantum double algebra of a finite group G, $D(G)$, are labelled by pairs $\{(C, \chi)\}$, where C is a conjugacy class of G and χ is an irreducible representation of the centraliser of an arbitrary representative element r of C, $Z(r)$. Once the representatives are fixed, another set of useful group elements are q_c for each $c \in C$ defined by $q_c r \bar{q}_c = c$, where $\bar{g}$ is the shorthand[15] for the inverse (g^{-1}). One basis for the (C, χ)-representation is given by the vectors $\{|\mu\rangle = |c, i\rangle\}$,

[15] A bar over a C-number represents complex conjugation.

where $c \in C$ and i are the vector index of the representation χ, $i = 1, \ldots, \chi(e)$, the dimension of the representation is hence $|C|\chi(e)$. In terms of this basis, the representation matrices of the quantum double algebra are given by:

$$\begin{aligned} B_{\mu\mu'}(h) &= \langle c, i| B(h) |c', i'\rangle = \delta_{c,h}\delta_{c,c'}\delta_{i,i'}, \\ A_{\mu\mu'}(g) &= \langle c, i| A(g) |c', i'\rangle = \delta_{c,gc'\bar{g}}\Gamma^{\chi}(\bar{q}_c g q_{c'}), \end{aligned} \tag{3.38}$$

where $B(h)$ and $A(g)$ are the generators of the quantum double algebra, and Γ^{χ} are the χ-representation matrices.

The results often mentioned are [134]:

1. The S-matrix elements given by

$$S_{ab} = \frac{1}{|G|} \sum_{\substack{c_a \in C_a, c_b \in C_a \\ c_a c_b = c_b c_a}} \chi_a(\bar{q}_a c_b q_a)\chi_b(\bar{q}_b c_a q_b),$$

   where $a = (C_a, \chi_a)$ and $b = (C_b, \chi_b)$ are two irreducible representations of the quantum double algebra.

2. The fusion rules (Verlinde formula) given by

$$N_{ab}^{c} = \sum_{l} \frac{S_{al} S_{bl} S_{cl}^{*}}{d_l},$$

   where $d_l = \chi_l(e)|C_l| = \dim_{\chi_l}|C_l|$ is the dimension of the l-representation.

However, exact expressions for the $F-$ and $R-$symbols are not as readily available. In the following, I will derive these expressions.

Tensor Product. We start with the expression for the projector $P_s^{(C,\chi)}$ onto the irreducible (C, χ)-representation of the quantum double algebra from some other representation s [134]:

$$P_s^{(C,\chi)} = \frac{\chi(e)}{|Z(r)|} \sum_{c \in C} \sum_{z \in Z(r)} \bar{\chi}(z) B_s(c) A_s(q_c z \bar{q}_c). \tag{3.39}$$

The representation s is a tensor product of two representations a and b, $s = a \otimes b \equiv ab$. Using the co-multiplication function of the quantum double algebra[134]

$$\Delta(B(h)A(g)) = \sum_{k \in G} B(k)A(g) \otimes B(\bar{k}h)A(g),$$

we can rewrite the projector in terms of the representations a and b:

$$P^x_{ab} = \frac{\chi(e)}{|Z(r)|} \sum_{c\in C} \sum_{z\in Z(r)} \sum_{h\in G} \bar{\chi}(z) B_a(h) A_a(q_c z \bar{q}_c) \otimes B_b(\bar{h}c) A_b(q_c z \bar{q}_c), \tag{3.40}$$

with $x = (C, \chi)$. Note that the rank of this projector is related to the fusion multiplicity by $d_x N^x_{ab}$. The reason why co-multiplication is included in the definition of the quantum double algebras is precisely to allow for tensor multiplication of representations.

Vertex Map. We now reduce the projection domain to one basis vector, $|c, i\rangle$, of the c-representation:

$$P^x_{ab}(c,i) = \frac{\chi(e)}{|Z(r)|} \sum_{z\in Z(r)} \sum_{h\in G} \bar{\Gamma}_{ii}(z) B_a(h) A_a(q_c z \bar{q}_c) \otimes B_b(\bar{h}c) A_b(q_c z \bar{q}_c). \tag{3.41}$$

$$P^x_{ab}(c,i) \equiv |c,i\rangle_{ab} \langle c,i|_{ab} \tag{3.42}$$

Note that these reduced projectors are indeed projectors of rank one and that summing over them recovers the full projector. This allows us to define a new *linear* map:

$$\phi^{ab}_x : \mathcal{H}_x \to \mathcal{H}_a \otimes \mathcal{H}_b$$

by its action on the basis vectors $|c, i\rangle \in \mathcal{H}_x$:

$$\phi^{ab}_x(|c,i\rangle) = |c,i\rangle_{ab} \in \mathrm{Im} P^x_{ab}(c,i).$$

It returns the (normalised) non-degenerate eigenvector of the matrix on the RHS of eq. (3.41). I will refer to this object as the vertex map.

This definition has a local gauge freedom: $|c,i\rangle_{ab} \to e^{i\psi^{ab}_x(c,i)} |c,i\rangle_{ab}$ which needs to be fixed by requiring

$$A_{ab}(g) \circ \phi^{ab}_x \circ A_x(\bar{g}) = \phi^{ab}_x$$

for all $g \in G$, i.e. the group action must commute with the vertex map. The phases, $\psi^{ab}_x(c,i)$, must be chosen such that this system of equations is fulfilled for all $g \in G$:

$$\langle c', i'|_{ab} A_a(g) \otimes A_b(g) |c,i\rangle_{ab} = [A_x(g)]^{(c',i')}_{(c,i)},$$

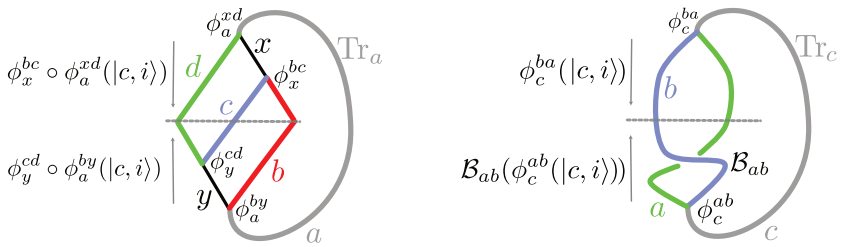

Figure 3.19: The diagrammatic representation of the (Left) $F-$symbol and (Right) $R-$symbol, with their corresponding expressions. The dashed gray line represents the vector space in which the main calculation, $\mathrm{Tr}_{a/c}$, is done, $\mathcal{H}_b \otimes \mathcal{H}_c \otimes \mathcal{H}_d$ for the $F-$symbol and $\mathcal{H}_a \otimes \mathcal{H}_b$ for the $R-$symbol.

for all (c,i) and (c',i') spanning $\mathcal{H}_x$. The possibility of this tast is, I conjecture, guaranteed by the structure of the algebra.

This operation removes the local gauge freedom, uniquely defining the vertex map up to a global gauge freedom, $\phi_x^{ab} \to e^{i\psi_x^{ab}} \phi_x^{ab}$, which is the usual gauge freedom of the $F-$ and $R-$ symbols themselves.

Results. With this map, we can now evaluate the diagrams in Figure 3.19 for the $F-$ and $R-$symbols, respectively. The results of these calculations are

$$(F_a^{bcd})_{xy} = \sum_{c,i} (\phi_y^{cd} \circ \phi_a^{by}(|c,i\rangle))^\dagger \phi_x^{bc} \circ \phi_a^{xd}(|c,i\rangle), \tag{3.43}$$

$$R_c^{ab} = \sum_{c,i} (\phi_c^{ba}(|c,i\rangle))^\dagger \mathcal{B}_{ab}(\phi_c^{ab}(|c,i\rangle)). \tag{3.44}$$

Comments. The latter expression being supplemented by the defining action of the braiding operator $\mathcal{B}_{ab} : \mathcal{H}_a \otimes \mathcal{H}_b \to \mathcal{H}_b \otimes \mathcal{H}_a$[134]:

$$\mathcal{B}_{ab} = Flip \circ (\sum_g A_g^a \otimes B_g^b), \tag{3.45}$$

where *Flip* just flips the two tensor factors. The way that nested vertex maps act is as follows:

$$\phi_y^{cd} \circ \phi_a^{by}(|\alpha\rangle_a) = \phi_y^{cd}(\sum_{\beta\gamma} |\beta\rangle_b |\gamma\rangle_y) = \sum_{\beta\gamma} |\beta\rangle_b \phi_y^{cd}(|\gamma\rangle_y). \tag{3.46}$$

The braided tensor category data for the irreducible representations of the quantum double algebra is now complete, for examples of these calculations see our repository [5].

I shall be telling this with a sigh
Somewhere ages and ages hence:
Two roads diverged in a wood, and I—
I took the one less traveled by,
And that has made all the difference.

— from *"The Road Not Taken"* by Robert Frost

4

Steady States in Monitored Toric Code

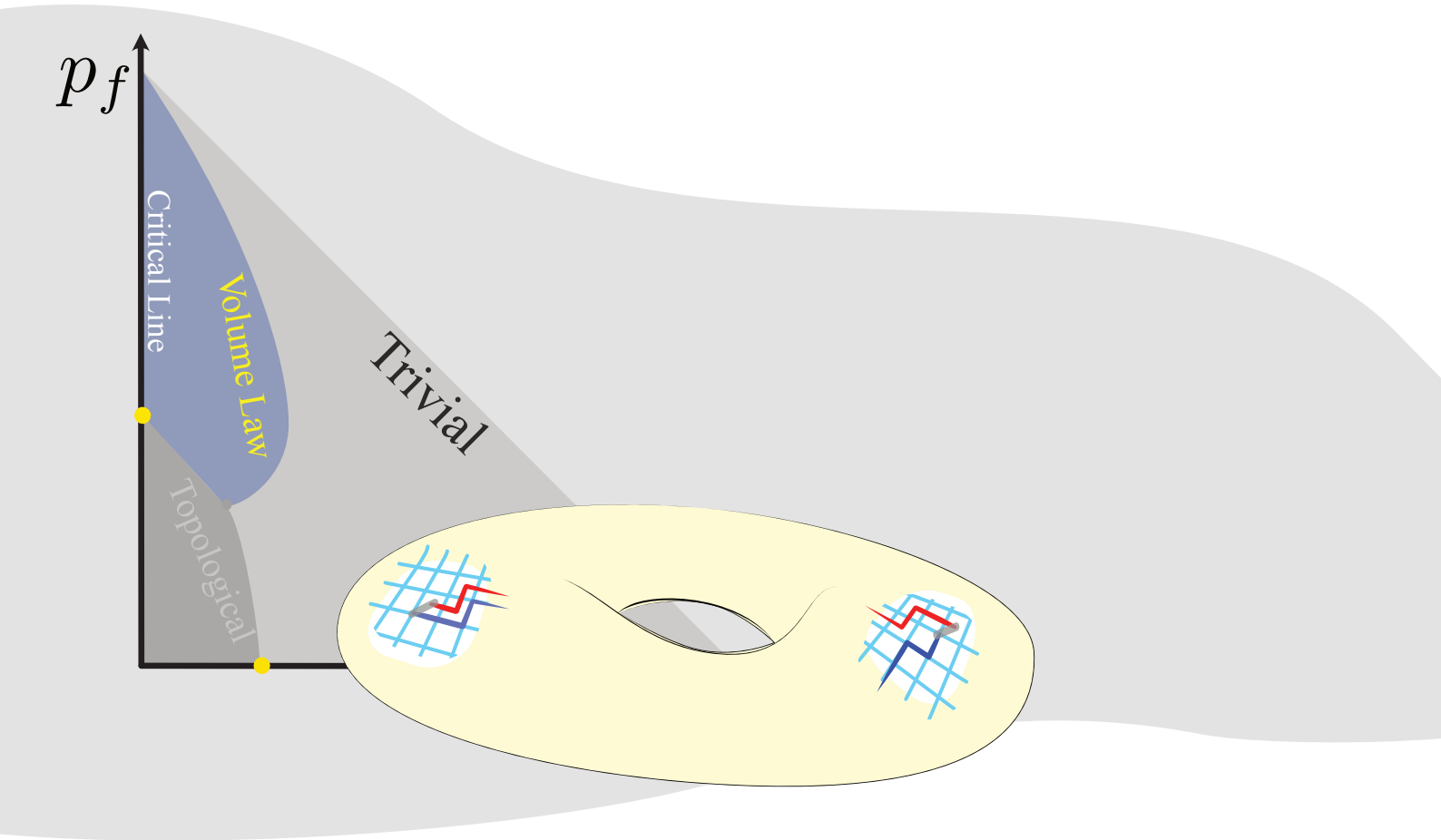

Building on the motivation laid out in the last part of the *Thesis Introduction*, I will now present our work on the measurement induced phases in the monitored toric code, as an exemplar topological stabiliser code. The background of our study are the recent results on intrinsically mixed-state topological order (imTO)[85, 86] and topological subsystem codes [84]. An imTO state can be obtained by letting anyonic errors proliferate in a decoherent manner by passing a topologically ordered state through a decoherence channel whose jump operators, once acted on this state, create anyonic excitations. We ask a complementary question: What if we proliferate the errors by measurement instead?

This chapter is based on our unpublished work:

> Jovanović, J., Placke, B., Parameswaran, S. and Simon, S.H., 2024. *Fermionic String-Glass Order in a Monitored Toric Code.* To Be Submitted.

In this work, our aim is to demonstrate a rich phase diagram of the steady states of stochastic processes composed of only measurements. In the next section, I will present a short primer on stabiliser methods[10] before defining the model. Afterwards, I will present the usual entanglement entropy data that one may expect in a study such as this[140–143], with the following section describing our main innovation: an (Edwards-Anderson-like) string-glass order parameter; how we define it, calculate it, and the results. Lastly, a brief summary of our findings will conclude this chapter.

4.1 The Model

Stabiliser Techniques. The $N-$qubit Pauli strings, e.g. operators of the form $e^{i\phi}X_1 \otimes Y_2 \otimes \mathbb{I}_3$ for $N = 3$, form a group $\mathcal{P}_2^N$ known as the $N-$qubit Pauli group; the subscript denotes the dimension of local dofs and X, Y and Z are the Pauli matrices. The stabiliser group S_ρ that defines a pure or mixed state, ρ, in the $N-$qubit Hilbert space $\mathcal{H}_2^N$, is the Abelian subgroup of the Pauli group which leaves the state invariant

$$g\rho = \rho g = \rho, \text{ for all } g \in S_\rho. \tag{4.1}$$

Note that this implies that $e^{i\phi}\mathbb{I} \in S_\rho$ iff $e^{i\phi} = 1$

The dimension of the stabiliser group is the number of generators or in terms of the size of the group $\dim S_\rho = \log_2 |S_\rho|$, since each generator may either be included or not. Each generator represents an independent binary constraint on the state, and if the number of independent constraints is equal to the number of qubits, the state is uniquely defined, and hence pure. If the state is not uniquely defined, then the stabiliser group represents an equal mixture of states made up of all states that satisfy given constraints; this implies a formula for the von Neumann entropy of a stabiliser state

$$S_{vN}(\rho) = N - \dim S_\rho.$$

In both pure and mixed states, given a stabiliser group, we can derive the density matrix and vice versa

$$\rho = \frac{1}{2^N} \sum_{g \in S} g. \tag{4.2}$$

This density matrix represents a uniform ensemble of some orthogonal basis states that span the code space of the stabiliser group, a maximally mixed state within the code space. To remind the reader of eq. (1.1), the code space is defined as:

$$\mathcal{H}_{S_\rho} = \text{span}\{|\psi\rangle \in \mathcal{H}_2^N \mid g|\psi\rangle = |\psi\rangle \text{ for all } g \in S_\rho\}.$$

The effects of partial traces follow directly from eq. (4.2), the partial trace over a region $\bar{A}$ removes all operators that act non-trivially on $\bar{A}$ from the stabiliser group to generate the stabiliser group of the reduced density matrix ρ_A, S_{ρ_A}.

Lastly, I describe the effects of Pauli measurements[1]. Performing a full projective measurement of a Pauli operator $g \in \mathcal{P}^N$ will project the state to one that is stabilised by sg, depending on the outcome of the measurement $s \in \{-1, +1\}$. If the operator sg is already in the stabiliser group, the result is always the same s and the state/stabiliser group is unchanged. Otherwise, the effect of this projection on the stabiliser group generated by a set $\{g_1, g_2, g_3, \ldots, g_m\}$ is to add this new

[1]A reader may check Ref. [10] for the classical simulations of Clifford circuits (unitary maps that take Pauli strings to Pauli strings), which is the main use of stabiliser techniques.

generator, sg, while removing those which do not commute with it, if there are any. Measurement can either increase the dimension of the stabiliser group or leave it unchanged. This is because the generators can always be chosen such that only one does not commute with the new generator, since Pauli operators either commute or anti-commute. For example, say $\{g_1, g_2, g_3\}$ all anti-commute with sg, the new set of generators is simply $\{sg, g_1g_2, g_1g_3\}$. Measurements cannot increase the von Neumann entropy, and if the state is pure, it remains pure with an altered stabiliser group.

Monitored Toric Code. The toric code (TC) is *the* paradigmatic toy model of topological order, it is defined on a graph, a square lattice in this case, with the degrees of freedom located on the edges. Its ground state in the stabiliser formalism is defined by a stabiliser group, S_{TC}, generated by the star and plaquette operators, shown in Figure 4.1 (a)[2].

Concretely, the star and plaquette operators are respectively:

$$g_n^s = \prod_{i \in n^s} X_i \text{ and } g_n^p = \prod_{i \in n^p} Z_i. \tag{4.3}$$

The index n refers to the sites/vertices in the square lattice, while the index i refers to edges hosting the qubit dofs; the set n^s is the set of edges that meet at a site/vertex n and the set n^p is the set of edges that form a plaquette that touches the site/vertex n to the northeast of it. I will refer to these generators collectively as $g_i^{\text{TC}} \in S_{\text{TC}}$, unless I need to specify the type. The state defined by this stabiliser group is a uniform mixture of the four degenerate ground states of this model on a torus; square lattice of size $L \times L$ with periodic boundary condition.

The logical operators acting non-trivially in this four-dimensional code/logical space are defined on the non-contractible loops of the torus. They can be defined as:

$$\tilde{Z}_1 = \prod_{i \in l^v} Z_i,\ \tilde{Z}_2 = \prod_{i \in l^h} Z_i,\ \tilde{X}_2 = \prod_{i \in \bar{l}^v} X_i \text{ and } \tilde{X}_1 = \prod_{i \in \bar{l}^h} X_i. \tag{4.4}$$

The sets $l^{(v/h)}$ are sets of edges along an arbitrary path on a direct lattice (from vertex to vertex) looping vertically/horizontally around the torus/lattice; while

[2]Same as the terms in the $\mathbb{Z}_2$ quantum double model Hamiltonian from the last chapter.

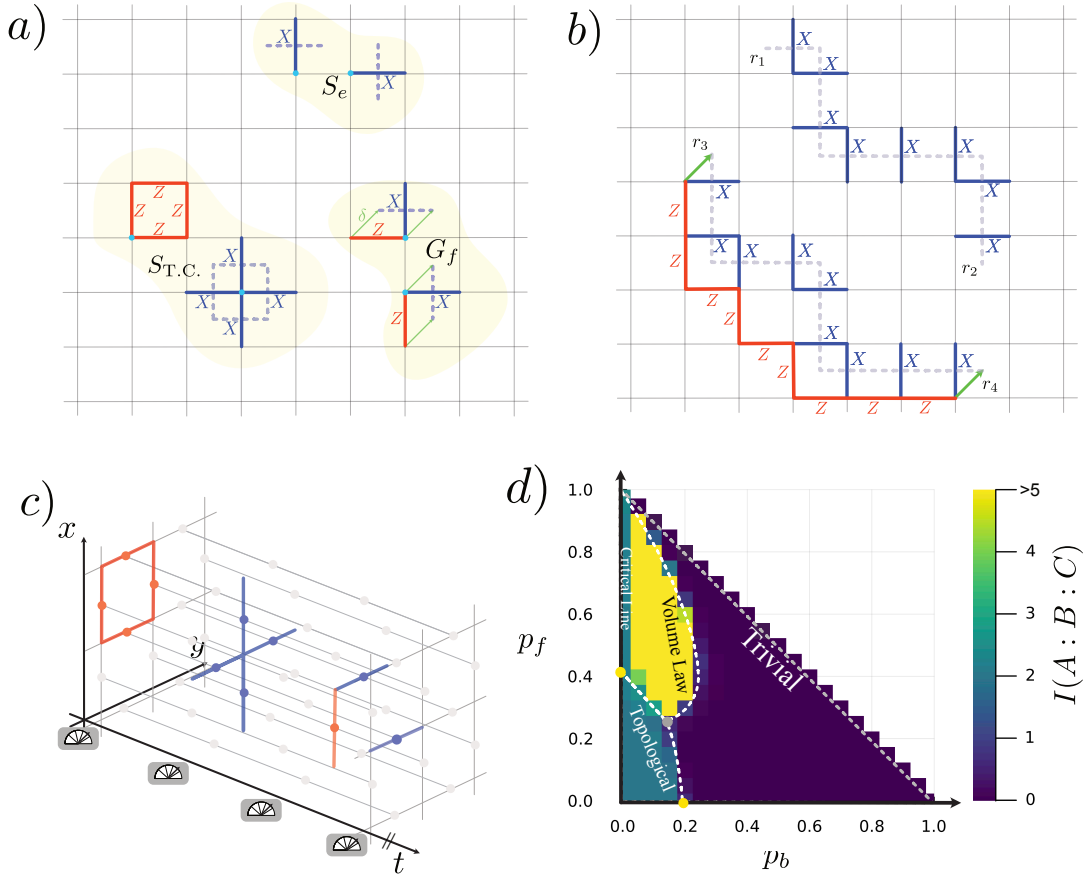

Figure 4.1: a) Generators of the toric code stabiliser group S_{TC}, the plaquette defect stabiliser group S_e and the fermion defect gauge group G_f. In the case of S_e, dashed line connects two plaquettes violated by the action of the generator; and in the case of G_f arrows show two fermion defects created by the generator.
b) Examples of long string operators that may proliferate in the steady state, (top) bosonic and (bottom) fermionic.
c) An example of a time-step of the measurement-only dynamics. Four layers of measurements are performed, in each layer a single generator is measured. In this example, the 3$^{\text{rd}}$and the 4$^{\text{th}}$measurements do not commute with one another, and nor do the 1$^{\text{st}}$and 4$^{\text{th}}$. Blue circles are Pauli-X operators, while the red are Pauli-Z.The measurements are chosen randomly, and the (pure) states are sampled from the steady state ensemble of these stochastic circuits.
d) A proposed phase diagram of the steady states. In each time step, we perform a number of measurements equal to the number of qubits (edges)N, with on average $p_b N$ and $p_f N$ of them being measurement of short bosonic and fermionic strings, respectively; all other being toric code stabilisers. The phase diagram is overlaid over observed values of tripartite mutual information, for the regions defined in Ref. [144], which are topological (2 in the case of toric code) if the states are area law entangled.

$\bar{l}^{(v/h)}$ are sets of edges crossed by an arbitrary path on a dual lattice (from plaquette to plaquette) looping vertically/horizontally around the torus/lattice. The logical space is that of two logical qubits, and including any two mutually commuting products of the four operators above into the stabiliser group results in a stabiliser group of a pure state. These are closed ribbon operators in the language of the previous chapter, closed over the non-contractible loops. They are labelled by the excitations they leave at their endpoints, if they are open, once they act on the ground state; see Figure 4.1(b) for examples of long open ribbon operators in the cases of plaquette violations (m anyons, above) and combined plaquette-vertex violation (toric code fermions, below).

The long anyon strings are generated by short anyon strings, shown in Figure 4.1 (a), which span the S_e and G_f groups. The generators of S_e, $g_i^e = X_i$ for any edge i, create plaquette violations at the plaquettes on each side of the edge i; that is, the state $g\,|G.S.\rangle$ for some $|G.S.\rangle \in \mathcal{H}_{S^{TC}}$ has these two plaquettes violated, and measuring g_n^p on the two plaquettes gives the result -1 instead of $+1$. Similarly, generators of G_f, $g_i^f = Z_i X_{i^{\uparrow}_{\rightarrow}}$ for any edge i and the edge northeast of it $i^{\uparrow}_{\rightarrow}$, create neighbouring TC fermion excitations (touching-vertex-plaquette violations).

The short anyon strings model the local errors in our devices; if they are allowed to proliferate and generate a long-string that loops around the torus then they can corrupt the information encoded in the logical space; however, that takes at least $\mathcal{O}(L)$ local errors; up until that point we can correct their effects via measurement and error correction.

The effect of measuring the short anyon strings also violates the vertex and plaquette operators, but in a different way. Instead of applying the error operator, we project onto it, $((\mathbb{I} + sg)/2)\,|G.S.\rangle$ and not just $g\,|G.S.\rangle$. The resulting state is a superposition of a state with no violations and a state with two violations on neighbouring plaquettes; *anyon pairing between sites*. In this framework, errors can still proliferate, giving us states that in some sense have long-range anyon-anyon correlations. Later I will specify how we quantify this, but first I describe the process that generates such states, our stochastic monitored circuit.

Stochastic monitored circuit. We start from the ground state of the toric code, and at each time step we pick a random Pauli string to measure; see Figure 4.1(c). The measurements are picked from three different sets, shown in Figure 4.1(a):

1. Plaquette defect generators g_i^e, creating a pair of plaquette violations.
2. Fermionic defect generators g_i^f, creating a pair of fermionic violations.
3. Toric code stabilisers g_i^{TC}, correcting these errors.

The operators are chosen from these sets with probabilities $(p_b, p_f, 1-p_b-p_f)$, respectively, while within the set the probability of picking any operator is uniform, $p_i = 1/2L^2$. Each long-time realisation of these stochastic circuits, Figure 4.1(c), samples some steady-state ensemble of pure states (stabiliser groups) defined by probabilities (p_b, p_f)[3].

These short anyonic errors may proliferate, resulting in long anyonic strings appearing readily in our steady-state ensembles of stabiliser groups; see Figure 4.1(b) for an example of a bosonic and a fermionic long string. Figure 4.1(d) shows the proposed (p_b, p_f) phase diagram for these steady-state ensembles, with four distinct regions: volume law phase, where long fermion strings proliferate; trivial area law phase, where long bosonic string proliferate; topologically ordered phase, where no strings proliferate; and a critical line characterised by its entanglement scaling. More detail will follow in the next two sections.

4.2 Entanglement measures

In studies of measurement-induced phases and transitions, entanglement entropy is often a very useful tool in diagnosing different regimes[16, 140–143, 145–147]. It is no different in our case, the entanglement entropy is a good tool for telling apart our three phases. We focus on two main entanglement entropy measures;

[3]Given that the circuits are observed to be ergodic, one can also sample in-time, taking the first sample after the initial relaxation and making sure subsequent samples are spaced further than the autocorrelation time. Relaxation and autocorrelation times can be inferred by looking at, for example, the half-system entropy as a function of time.

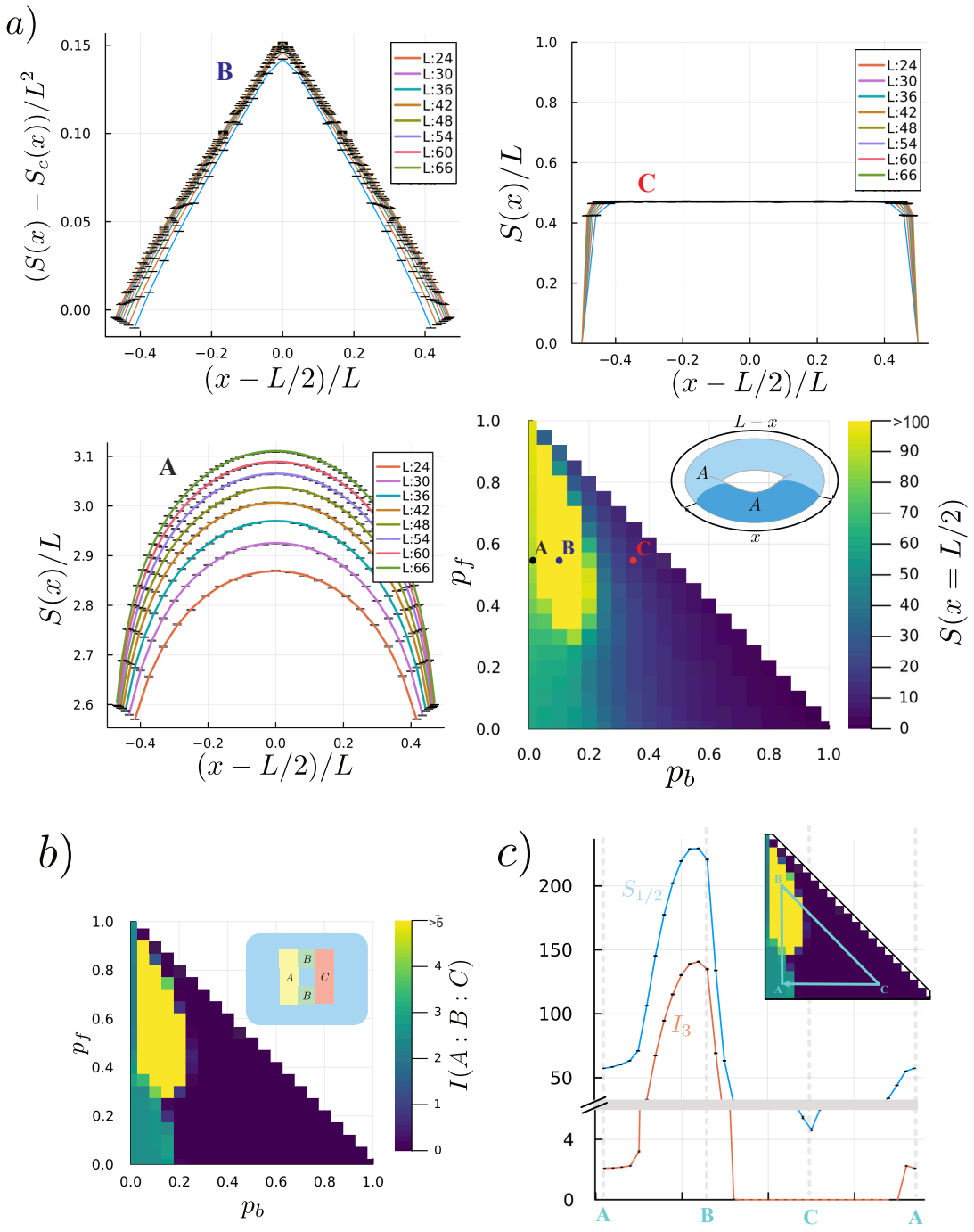

Figure 4.2: Entanglement characteristics of states on a torus:
a) Scaling collapses for the entanglement entropy for an annular region of length x on the torus of linear size L. Data is averages over states in steady state ensembles on the critical line (A), in the volume law phase (B) and in the trivial phase (C). Critical contribution was subtracted from the volume law data before doing the collapse. The critical data was fitted by the scaling function form found in Ref. [140].
b) Tripartite mutual information, topological entanglement entropy, averaged over the steady-state ensembles. The main data used to infer the proposed phase diagram. Linear size of the torus is $L = 30$.
c) Half system entropy ($S(x = L/2) = S_{1/2}$) and the tripartite (topological) mutual information ($I(A : B : C) = I_3$) for a path taken around the parameter space. Path passes through all the transitions. Linear size of the torus is $L = 30$.

the finite-size entanglement entropy scaling, see Figure 4.2(a), and the topological entanglement entropy, Figure 4.2(b).

The entanglement scaling data clearly suggest three regimes:

1. the trivial area law, characteristic of the topologically ordered and trivial phases,
2. the critical line, whose entanglement scaling is well-fitted by the 2d Conformal Field Theory[112] or 2d Fermi Surface[148] functional forms, and
3. the structured volume law, similar to the one found recently in the monitored Kitaev honeycomb model[140]. The "structured" refers to the sub-leading critical contribution.

It is important to note that the critical entanglement scaling on the critical line does not necessarily suggest that the states on the line are captured by Conformal Field Theories (CFTs), given that the fit parameters vary along the line and, in particular, the one corresponding to what would be the central charge of a CFT does not necessarily match those of any known CFT along the line.

The topological entanglement entropy further splits the area law phases into topological ($I(A:B:C)=2$)[4] and trivial ($I(A:B:C)=0$). This measure diagnoses long-range entanglement; hence, it diverges in the volume law phase. On the critical line ($p_b=0, p_f \geq p_f^c \approx 0.4$), the topological entanglement entropy fluctuates (within the ensemble) around its value in the topological phase, with the onset of large fluctuations a sign that we have entered this regime.

Figure 4.2(c) shows the main two entanglement measures, the entanglement entropy of the half system and the topological entanglement entropy, for a path taken in the parameter space that passes through all transitions.

4.3 String-Glass Order Parameter

In order to go beyond the entanglement measures, we define order parameters for these phases. We call them string-glass order parameters, due to the way

[4]To remind the reader, $I(A:B:C) = S_A + S_B + S_C - S_{AB} - S_{BC} - S_{AC} + S_{ABC}$. The regions A,B and C are shown in Figure 4.2(b).

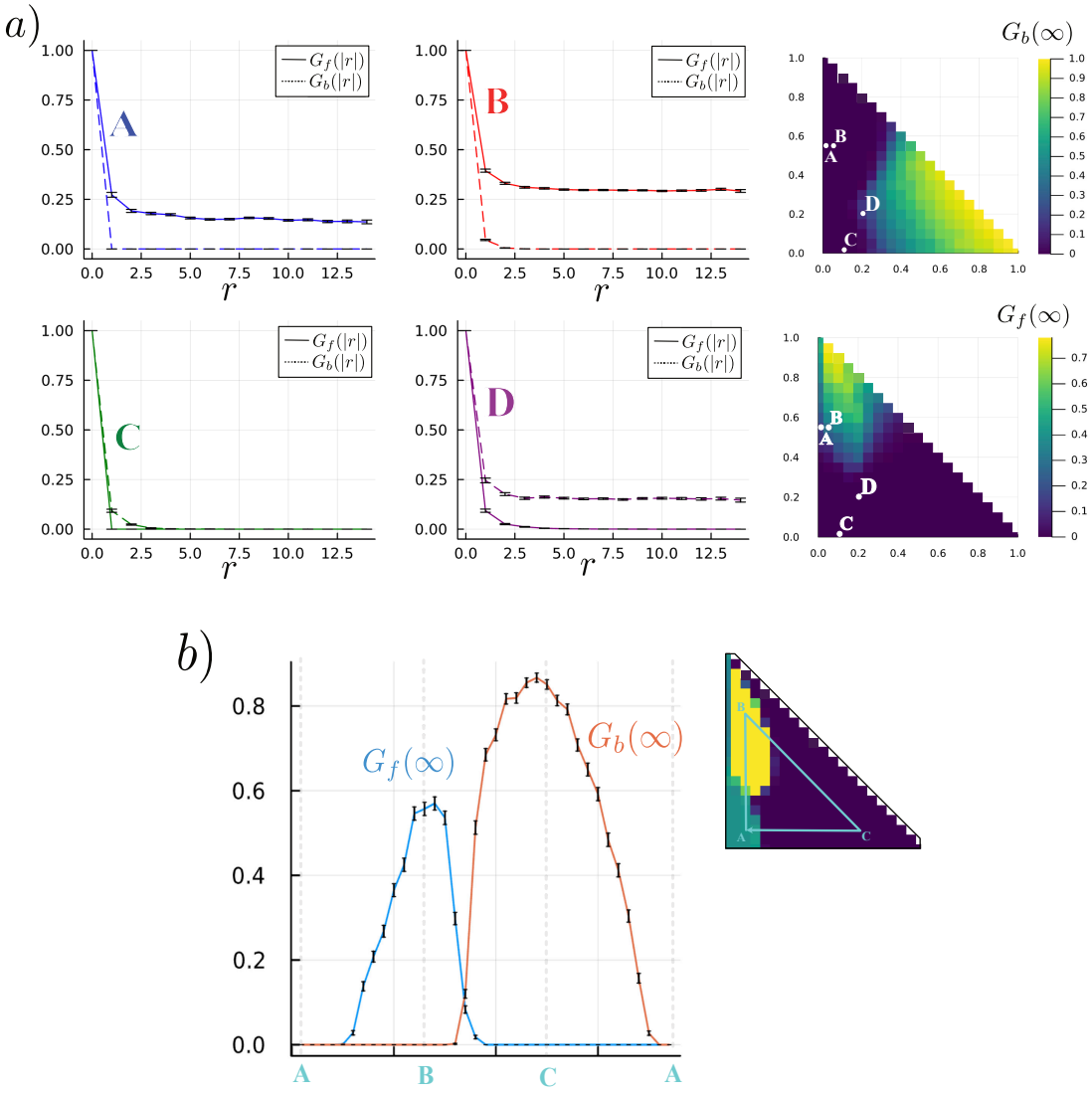

Figure 4.3: String-glass order parameter (SGOP), on a torus of linear size $L = 30$:
a) Bosonic and fermionic two-point function versus the taxi-cab separation of the two points. The data is averaged over states in steady state ensembles on the critical line (A), in the volume law phase (B), topologically ordered phase (C) and the trivial phase (D). All phases have a finite correlation length, with only difference being the long-distance asymptotic value $G_{b(f)}(\infty)$, which we call the bosonic(fermionic) SGOP. Volume law phase and the critical line acquire a non-zero fermionic SGOP, while the trivial acquire a non-zero bosonic SGOP. The topologically ordered phase correspond to the symmetry unbroken phase.
b) Two SGOPs for a path taken around the parameter space. Path passes through all the transitions. The peak in the fermionic SGOP correspond to the peak in the half-system entanglement entropy in Figure 4.2 (b), while the peak in the bosonic SGOP correspond to the minima in the half-system entanglement entropy.

in which they acquire values upon phase transition being comparable to spin-glass transitions[149, 150].

The definition is as follows. We identify two sites, r_1 and r_2, and ask if there is a string (fermionic or bosonic) in the stabiliser group that connects them. If there is such a string operator[5], it has a definite expectation value of ± 1 or 1 when squared.

$$G_{b(f)}(r_1, r_2) = \overline{\max_{O \in \mathcal{S}_{b(f)}(r_1, r_2)} \langle \psi | O | \psi \rangle^2}, \tag{4.5}$$

where the overline means the ensemble average over states $|\psi\rangle$ and $\mathcal{S}_{b(f)}(r_1, r_2)$ is the set of all Pauli operators that create a pair of bosonic (fermionic) defects between sites r_1 and r_2.

Operationally, how this is calculated is:

$$G_{b(f)}(r_1, r_2) = \overline{\dim \left[\langle R_{b(f)}(r_1, r_2), G_d \rangle \cap S_\psi \right] - \dim \left[G_d \cap S_\psi \right]}, \tag{4.6}$$

where $\cap$ represents the intersection of two Pauli subroups, $R_{b(f)}(r_1, r_2)$ is any string operator that creates bosonic(fermionic) defects between two sites, and lastly G_d is the group of all closed loops; all the ways in which $R_{b(f)}$ can be deformed while still having the same effect on the ground state of the toric code.

Angle brackets represent a group generated by all elements between brackets. The exact form for G_d is $\langle S_{\mathrm{TC}}, \tilde{X}_1, \tilde{X}_2, \tilde{Z}_1, \tilde{Z}_2 \rangle$, where the last four are the logical operators of the toric code, defined on the noncontractable loops around the torus. The RHS of the eq. (4.6) under the overline is 1 or 0 depending on whether there is an appropriate ribbon operator in the stabiliser group S_ψ or not, respectively.

We call this string-glass order parameter (SGOP) or the Zassenhaus correlator, since the dimensions of the group overlaps were calculated via the Zassenhaus algorithm[151].

The results are shown in Figure 4.3. The order parameter characterises the phases remarkably well, the volume law phase (critical line included) is diagnosed by a non-zero fermionic SGOP and the trivial phase by a non-zero bosonic SGOP; in the topological phase both are zero.

[5]Ribbon operator in the language of the previous chapter.

	fSGOP	bSGOP	TEE	EE
Topological	0	0	2	Area Law
Trivial	0	non-zero	0	Area Law
Volume Law	non-zero	0	undefined	Volume Law
Critical Line	non-zero	0	≈ 2	Critical

Figure 4.4: Characteristics of the various phases observed in the numerical experiments.

4.4 Chapter Summary

The summary of our findings is shown in Table 4.4. In the monitored toric code, where we perform competing measurements of toric code stabilisers, short bosonic and short fermionic strings; we have uncovered a complex phase diagram of steady-state ensembles of such stochastic circuits. The main parameters of the phase diagram are the relative rates of bosonic and fermionic measurements. In addition to the usual entanglement measures, which diagnose different phases well, we have constructed string-glass order parameter that correspond to long-range anyon-anyon correlations in the steady-state ensembles. The string-glass-order parameter data agrees with the entropy data when considering categorisation of phases.

As we bring the work closer to publication, we hope to offer a deeper conceptual description of the volume law phase (critical line included)[6]; what we call the fermionic string-glass order, possibly relating it more closely to anyon condensation and other theoretical frameworks.

[6]Topological and trivial (paramagnet) phase are already well understood.

Je n'ai fait celle-ci plus longue que parce que je n'ai pas eu le loisir de la faire plus courte.

— from *"Lettres Provinciales"* by Blaise Pascal

5 Conclusions and Outlooks

Given the independent nature of the three pieces of work presented, I will offer three separte comments before my closding remarks.

Entanglement dynamics. We have introduced a number of Operator Entanglement Entropy (OpEE) measures that characterise the entanglement development and information transport capabilities of a quantum time evolution operator/channel. Two in particular have been singled out, the tripartite OpEE (tOpEE) which has been related to the scrambling properties of time evolution by connecting it to the fidelity of many-body teleportation[38]; and the bipartite OpEE (bOpEE) which has been related to the transport of conserved densities.

The tOpEE is a noise-resistant probe of scrambling, unlike out-of-time order correlators (OTOCs) whose decay is not a consequence unique to scrambling, but also noise and mismatch in the device implementation of forward and backward time evolution[152, 153].

In addition to defining these quantities and their relation to features of quantum dynamics, we proposed a modified classical shadows protocol[37] that can be used to tomograph quantum channels and estimate these OpEE quantities, among others; in a manner that is quantum recourse efficient, requires no additional ancilla qubits and no deep circuits apart from the time evolution channel itself. The only downside,

in the case of tOpEE only, is the exponential scaling (in the system size) of the number of shots required for a fixed precision.

In the case of tOpEE and a predefined time evolution that we wish to characterise, we could distill the entanglement from the large region B into a smaller region B' and tomograph the smaller combined region $AB'C$; hence, reducing the number of shots required[1]. The extreme case of this procedure is a full decoder for many-body teleportation (for example, Ref. [154]), $|B'C| = |A|$. However, for large systems, the decoders are extensively deep circuits, and therefore in a noisy setting, careful consideration needs to be made.

Bipartite OpEE does not suffer from this scaling, but, like OTOCs [2] it decays in the presence of noise and scrambling. However, unlike OTOCs, they are easy to measure in NISQ devices via our protocol. Their relation to the transport of conserved charges, i.e. the lower bound on their decay being determined by the slowly decaying modes, makes them an ideal probe of transport in the case where the form of the transported charge is unknown or hard to access (measure); since in addition to the probe being initial state independent, it is also charge agnostic.

To demonstrate the practicality of our proposal, we have run an experiment on the IBM's cloud device, demonstrating that we have achieved scrambling in our sampled circuit; and in order to show the descriptive power of the bOpEE I have presented a series of calculations in various systems exhibiting a myriad of transport regimes, with each of them contributing distinct features to the bOpEE.

It is worth mentioning previous works that use measures similar to bOpEE to quantify various features of quantum dynamics, e.g. in Refs. [155, 156], and how our work differs. Namely, they look at the entanglement structures of the state dual to a Heisenberg-time-evolved local operator $|O_x(t)\rangle$, in order to probe the growth of the operator, without relating it back to transport.

A natural way to extend this research is to perform bOpEE measurement experiments in long qubit arrays to demonstrate the feasibility of this protocol. In

[1] This, however, is not possible if we want to characterise an unknown or a random time evolution channel.

[2] They are closely related, see Figure 2.7c

addition, the question of remarkable convergence of the MPS based numerics in the case of free-fermion systems[3] is also an interesting direction for future work. Beyond quantum chaos and (one-dimensional) transport, it would be of interest to explore the use of these techniques in other setting such as; entanglement phase transitions in monitored circuits[157], quantised chiral information propagation in anomalous Floquet topological phases[158], etc[4].

Non-Abelian anyon braiding. In this work, we have examined the feasibility of probing non-Abelian anyon signatures in the quantum double $D(D_4)$ model, which included deriving simplified circuits for anyon manipulation and topological charge measurement protocols, partly by utilising the group structure of D_4 and partly by the depth versus repetition and post-selection tradeoff (reduced charge measurement needs to be repeated with different subgroups for full diagnosis). Our protocols would need to be supplemented with the measure and feedforward ground state preparation protocols in order to be run on larger systems.

In the case of quasi-one-dimensional and small two-dimensional systems, where we can afford a direct ground state preparation, we have demonstrated via realistic noisy classical simulations that even without any error mitigation or noise reduction (e.g. dynamical decoupling) we can observe non-Abelian anyon fusion and braiding, as well as measure much of the modular data for $D(D_4)$ with our anyon interferometry protocols.

Our work contributes to the currently thriving research on this topic, especially with our topological charge measurement protocol, which is a necessary tool to make certain quantum double model, e.g. $D(S_3)$ computationally universal.

In terms of future work, while writing this thesis, an experimental group is working on implementing this proposal. On the theoretical side, it is an interesting question to try and adapt the classical shadow (another example of depth versus repetition tradeoff) tomography to measure topological charge by

[3]With an observation that the TEBD truncation error itself seems to be spreading no faster than transport, see Figure 2.9c.

[4]As of completion of our paper[1] Refs. [114, 115] appeared with similar channel tomography proposals.

designing appropriate randomising unitaries in order to extract that information in a short efficient manner; perhaps inspired by our group-theory-based reduced charge measurement protocol. This is in addition to systematically eliminating the need for ancillas in the ribbon operator protocol.

Fermionic string-glass order. The data from the numerical experiments suggest that in our monitored toric code we have a setting that realises a rich assortment of phases. We characterise these different regimes not only by their entanglement structure, a place where many studies of this kind end, but by also providing a good order parameter that uncovers complicated stabiliser structures in the states themselves that may be responsible for the observed entanglement structure.

Much of our theoretical understanding of these results is incomplete, especially our understanding of the observed phase, which we call fermionic string-glass order. In particular, we need to relate the onset of this phase to the established mechanism of phase transitions in similar models, such as anyon condensation in Hamiltonian systems and decoherent anyon proliferation in imTO. Afterwards, we can generalise our search for steady-state phases of monitored Pauli codes on qudits ($S \subset \mathcal{P}_d^N$), where the imTO classification is significantly richer than in the case of qubit Pauli codes[84]. In addition, it is worth devising experimental protocols to probe this phase diagram.

Closing Remarks. The three studies may appear unrelated, but it would be unwise to ignore the links between them: the LOCC's role in distilling entanglement and decoding quantum information, and its power to prepare topologically entangled states; the classical shadows tomography and the reduced charge measurement, both being examples of depth versus repetition tradeoff often needed to be considered in designing NISQ experiment; and finally, the monitored toric code itself being a perturbation of the simplest quantum double model, where the entanglement entropy played a crucial role in uncovering its phase diagram. However, what I hope these three studies have left the reader with is an appreciation of what NISQ is capable of in the context of quantum many-body physics and maybe a little bit of cautiously realistic optimism for the field of quantum simulation as a whole.

References

[1] Max McGinley et al. “Quantifying information scrambling via classical shadow tomography on programmable quantum simulators”. In: *Physical Review A* 106.1 (2022), p. 012441. eprint: 2202.05132.

[2] Jovan Jovanović et al. “A proposal to demonstrate non-abelian anyons on a NISQ device”. In: *Quantum* 8 (2024), p. 1408.

[3] Jovan Jovanović et al. “Fermionic String-Glass Order in a Monitored Toric Code”. 2024.

[4] Jovan Jovanović and Max McGinley. *GitHub repository: OpEE_Redone_2023-2024*. https://github.com/jovanov5/OpEE_Redone_2023-2024.git. 2023.

[5] Jovan Jovanović, Daan Timmers, and Carolin Wille. *GitHub repository: kitaevsim*. https://github.com/DaanTimmers/kitaevsim. 2022.

[6] Jovan Jovanović and Carolin Wille. *Google Drive repository: Compiled circuits for external collaborators*. https://drive.google.com/drive/folders/1bPn1ezCVAowkMWX3Pf2Iyu_kSI81uDz5?usp=sharing. 2023.

[7] Jovan Jovanović. *GitHub repository: Subsystem-Code-Physics*. https://github.com/jovanov5/Subsystem-Code-Physics.git. 2023.

[8] Jovan Jovanović. *GitHub repository: dphil_thesis_text*. https://github.com/jovanov5/dphil_thesis_text.git. 2024.

[9] John Preskill. “Quantum computing 40 years later”. In: *arXiv* (2021). eprint: 2106.10522.

[10] Michael A Nielsen and Isaac L Chuang. *Quantum computation and quantum information*. Vol. 2. Cambridge university press Cambridge, 2001.

[11] Eric Chitambar et al. “Everything You Always Wanted to Know About LOCC (But Were Afraid to Ask)”. In: *arXiv* (2012). eprint: 1210.4583.

[12] Charles H. Bennett et al. “Teleporting an unknown quantum state via dual classical and Einstein-Podolsky-Rosen channels”. In: *Physical Review Letters* 70.13 (1992), pp. 1895–1899.

[13] Frank Arute et al. “Quantum supremacy using a programmable superconducting processor”. In: *Nature* 574.7779 (2019), pp. 505–510. eprint: 1910.11333.

[14] Xiao Mi et al. “Time-crystalline eigenstate order on a quantum processor”. In: *Nature* 601.7894 (2022), pp. 531–536. eprint: 2107.13571.

[15] X. Mi et al. “Noise-resilient edge modes on a chain of superconducting qubits”. In: *Science* 378.6621 (2022), pp. 785–790. eprint: 2204.11372.

[16] Collaborators, Google Quantum AI and et al. "Measurement-induced entanglement and teleportation on a noisy quantum processor". In: *Nature* 622.7983 (2023), pp. 481–486. eprint: 2303.04792.

[17] Werner Krauth. *Statistical mechanics: algorithms and computations*. Vol. 13. OUP Oxford, 2006.

[18] Gabriele Tartero and Werner Krauth. "Concepts in Monte Carlo sampling". In: *arXiv* (2023). eprint: 2309.03136.

[19] Dmitry A Abanin et al. "Colloquium: Many-body localization, thermalization, and entanglement". In: *Reviews of Modern Physics* 91.2 (2019), p. 021001. eprint: 1804.11065.

[20] Pasquale Calabrese and John Cardy. "Entanglement entropy and conformal field theory". In: *Journal of Physics A: Mathematical and Theoretical* 42.50 (2009), p. 504005. eprint: 0905.4013.

[21] Vincenzo Alba and Pasquale Calabrese. "Entanglement and thermodynamics after a quantum quench in integrable systems". In: *Proceedings of the National Academy of Sciences* 114.30 (2017), pp. 7947–7951. eprint: 1608.00614.

[22] Adam Nahum et al. "Quantum Entanglement Growth under Random Unitary Dynamics". In: *Phys. Rev. X* 7 (3 July 2017), p. 031016. URL: https://link.aps.org/doi/10.1103/PhysRevX.7.031016.

[23] Alessandro Foligno and Bruno Bertini. "Growth of entanglement of generic states under dual-unitary dynamics". In: *Physical Review B* 107.17 (2023), p. 174311. eprint: 2208.00030.

[24] Kai Klocke, Joel E Moore, and Michael Buchhold. "Power-law entanglement and Hilbert space fragmentation in non-reciprocal quantum circuits". In: *arXiv* (2024). eprint: 2405.06021.

[25] Hong Liu and S. Josephine Suh. "Entanglement growth during thermalization in holographic systems". In: *Physical Review D* 89.6 (2013), p. 066012. eprint: 1311.1200.

[26] Paolo Zanardi, Christof Zalka, and Lara Faoro. "Entangling power of quantum evolutions". In: *Phys. Rev. A* 62 (3 Aug. 2000), p. 030301. URL: https://link.aps.org/doi/10.1103/PhysRevA.62.030301.

[27] Paolo Zanardi. "Entanglement of quantum evolutions". In: *Phys. Rev. A* 63 (4 Mar. 2001), p. 040304. URL: https://link.aps.org/doi/10.1103/PhysRevA.63.040304.

[28] Pavan Hosur et al. "Chaos in quantum channels". In: *Journal of High Energy Physics* 2016.2 (2016), pp. 1–49.

[29] Yuri D Lensky and Xiao-Liang Qi. "Chaos and high temperature pure state thermalization". In: *Journal of High Energy Physics* 2019.6 (2019), pp. 1–19.

[30] Artur K. Ekert et al. "Direct Estimations of Linear and Nonlinear Functionals of a Quantum State". In: *Phys. Rev. Lett.* 88 (21 May 2002), p. 217901. URL: https://link.aps.org/doi/10.1103/PhysRevLett.88.217901.

[31] C. Moura Alves and D. Jaksch. "Multipartite Entanglement Detection in Bosons". In: *Phys. Rev. Lett.* 93 (11 Sept. 2004), p. 110501. URL: https://link.aps.org/doi/10.1103/PhysRevLett.93.110501.

[32] A. J. Daley et al. "Measuring Entanglement Growth in Quench Dynamics of Bosons in an Optical Lattice". In: *Phys. Rev. Lett.* 109 (2 July 2012), p. 020505. URL: https://link.aps.org/doi/10.1103/PhysRevLett.109.020505.

[33] Hannes Pichler et al. "Thermal versus entanglement entropy: a measurement protocol for fermionic atoms with a quantum gas microscope". In: *New Journal of Physics* 15.6 (June 2013), p. 063003. URL: https://doi.org/10.1088/1367-2630/15/6/063003.

[34] Rajibul Islam et al. "Measuring entanglement entropy in a quantum many-body system". In: *Nature* 528.7580 (2015), pp. 77–83.

[35] A. Elben et al. "Rényi Entropies from Random Quenches in Atomic Hubbard and Spin Models". In: *Phys. Rev. Lett.* 120 (5 Feb. 2018), p. 050406. URL: https://link.aps.org/doi/10.1103/PhysRevLett.120.050406.

[36] Tiff Brydges et al. "Probing Rényi entanglement entropy via randomized measurements". In: *Science* 364.6437 (2019), pp. 260–263. URL: https://science.sciencemag.org/content/364/6437/260.

[37] Hsin-Yuan Huang, Richard Kueng, and John Preskill. "Predicting many properties of a quantum system from very few measurements". In: *Nature Physics* 16.10 (2020), pp. 1050–1057.

[38] Patrick Hayden and John Preskill. "Black holes as mirrors: quantum information in random subsystems". In: *Journal of High Energy Physics* 2007.09 (Sept. 2007), pp. 120–120. URL: https://doi.org/10.1088/1126-6708/2007/09/120.

[39] Yasuhiro Sekino and L Susskind. "Fast scramblers". In: *Journal of High Energy Physics* 2008.10 (Oct. 2008), pp. 065–065. URL: https://doi.org/10.1088/1126-6708/2008/10/065.

[40] Stephen H Shenker and Douglas Stanford. "Black holes and the butterfly effect". In: *Journal of High Energy Physics* 2014.3 (2014), pp. 1–25.

[41] S. W. Hawking. "Breakdown of predictability in gravitational collapse". In: *Phys. Rev. D* 14 (10 Nov. 1976), pp. 2460–2473. URL: https://link.aps.org/doi/10.1103/PhysRevD.14.2460.

[42] J. M. Deutsch. "Quantum statistical mechanics in a closed system". In: *Physical Review A* 43.4 (1991), pp. 2046–2049.

[43] Mark Srednicki. "Chaos and quantum thermalization". In: *Physical Review E* 50.2 (1994), pp. 888–901. eprint: cond-mat/9403051.

[44] Hal Tasaki. "From Quantum Dynamics to the Canonical Distribution: General Picture and a Rigorous Example". In: *Physical Review Letters* 80.7 (1998), pp. 1373–1376. eprint: cond-mat/9707253.

[45] Marcos Rigol, Vanja Dunjko, and Maxim Olshanii. "Thermalization and its mechanism for generic isolated quantum systems". In: *Nature* 452.7189 (2008), pp. 854–858. eprint: 0708.1324.

[46] A. I. Larkin and Yu. N. Ovchinnikov. "Quasiclassical Method in the Theory of Superconductivity". In: *Soviet Journal of Experimental and Theoretical Physics* 28 (June 1969), p. 1200.

[47] A Kitaev. *Hidden correlations in the Hawking radiation and thermal noise*. talk at Fundamental Physics Prize Symposium. 2014.

[48] Daniel A. Roberts and Douglas Stanford. "Diagnosing Chaos Using Four-Point Functions in Two-Dimensional Conformal Field Theory". In: *Phys. Rev. Lett.* 115 (13 Sept. 2015), p. 131603. URL: https://link.aps.org/doi/10.1103/PhysRevLett.115.131603.

[49] Kevin A Landsman et al. "Verified quantum information scrambling". In: *Nature* 567.7746 (2019), pp. 61–65.

[50] Paolo Glorioso and Hong Liu. "Lectures on non-equilibrium effective field theories and fluctuating hydrodynamics". In: *arXiv* (2018). eprint: 1805.09331.

[51] Thomas Hartman, Sean A. Hartnoll, and Raghu Mahajan. "Upper Bound on Diffusivity". In: *Physical Review Letters* 119.14 (2017), p. 141601. eprint: 1706.00019.

[52] Luca Delacrétaz et al. "Thermalization and hydrodynamics of two-dimensional quantum field theories". In: *SciPost Physics* 12.4 (2022), p. 119. eprint: 2105.02229.

[53] Luca V Delacretaz. "Bound on Thermalization from Diffusive Fluctuations". In: *arXiv* (2023). eprint: 2310.16948.

[54] A.Yu. Kitaev. "Fault-tolerant quantum computation by anyons". In: *Annals of Physics* 303.1 (Jan. 2003), pp. 2–30. URL: https://doi.org/10.1016%2Fs0003-4916%2802%2900018-0.

[55] Robert Oeckl. *Discrete gauge theory: From lattices to TQFT*. Imperial College Press, 2005.

[56] Frank Wilczek. "Quantum Mechanics of Fractional-Spin Particles". In: *Phys. Rev. Lett.* 49 (14 Oct. 1982), pp. 957–959. URL: https://link.aps.org/doi/10.1103/PhysRevLett.49.957.

[57] Jon Magne Leinaas and Jan Myrheim. "On the theory of identical particles". In: *Il Nuovo Cimento B (1971-1996)* 37 (1977), pp. 1–23.

[58] D. C. Tsui, H. L. Stormer, and A. C. Gossard. "Two-Dimensional Magnetotransport in the Extreme Quantum Limit". In: *Phys. Rev. Lett.* 48 (22 May 1982), pp. 1559–1562. URL: https://link.aps.org/doi/10.1103/PhysRevLett.48.1559.

[59] B. I. Halperin. "Statistics of Quasiparticles and the Hierarchy of Fractional Quantized Hall States". In: *Phys. Rev. Lett.* 52 (18 Apr. 1984), pp. 1583–1586. URL: https://link.aps.org/doi/10.1103/PhysRevLett.52.1583.

[60] Daniel Arovas, J. R. Schrieffer, and Frank Wilczek. "Fractional Statistics and the Quantum Hall Effect". In: *Phys. Rev. Lett.* 53 (7 Aug. 1984), pp. 722–723. URL: https://link.aps.org/doi/10.1103/PhysRevLett.53.722.

[61] Alexei Kitaev. "Anyons in an exactly solved model and beyond". In: *Annals of Physics* 321.1 (Jan. 2006), pp. 2–11.

[62] Michael A. Levin and Xiao-Gang Wen. "String-net condensation: A physical mechanism for topological phases". In: *Physical Review B* 71.4 (Jan. 2005). URL: https://doi.org/10.1103%2Fphysrevb.71.045110.

[63] Kerstin Beer et al. "From categories to anyons: a travelogue". In: *arXiv* (2018). eprint: 1811.06670.

[64] J. Nakamura et al. “Direct observation of anyonic braiding statistics”. In: *Nature Physics* 16.9 (Sept. 2020), pp. 931–936. URL: https://doi.org/10.1038%2Fs41567-020-1019-1.

[65] Noah L Samuelson et al. “Anyonic statistics and slow quasiparticle dynamics in a graphene fractional quantum Hall interferometer”. In: *arXiv* (2024). eprint: 2403.19628.

[66] Thomas Werkmeister et al. “Anyon braiding and telegraph noise in a graphene interferometer”. In: *arXiv* (2024). eprint: 2403.18983.

[67] R. L. Willett et al. “Interference Measurements of Non-Abelian e/4 & Abelian e/2 Quasiparticle Braiding”. In: *Physical Review X* 13.1 (2023), p. 011028. eprint: 1905.10248.

[68] K. J. Satzinger et al. “Realizing topologically ordered states on a quantum processor”. In: *Science* 374.6572 (Dec. 2021), pp. 1237–1241. URL: https://doi.org/10.1126%2Fscience.abi8378.

[69] T. I. Andersen et al. “Non-Abelian braiding of graph vertices in a superconducting processor”. In: *Nature* (May 2023).

[70] Shibo Xu et al. *Digital simulation of non-Abelian anyons with 68 programmable superconducting qubits*. 2022. arXiv: 2211.09802 [quant-ph].

[71] Mohsin Iqbal et al. *Creation of Non-Abelian Topological Order and Anyons on a Trapped-Ion Processor*. 2023. arXiv: 2305.03766.

[72] Chetan Nayak et al. “Non-Abelian anyons and topological quantum computation”. In: *Rev. Mod. Phys.* 80 (3 Sept. 2008), pp. 1083–1159. URL: https://link.aps.org/doi/10.1103/RevModPhys.80.1083.

[73] Shibo Xu et al. “Non-Abelian braiding of Fibonacci anyons with a superconducting processor”. In: *arXiv* (2024). eprint: 2404.00091.

[74] Carlos Mochon. “Anyon computers with smaller groups”. In: *Physical Review A* 69.3 (Mar. 2004).

[75] M. Aguado et al. “Creation, Manipulation, and Detection of Abelian and Non-Abelian Anyons in Optical Lattices”. In: *Phys. Rev. Lett.* 101 (26 Dec. 2008), p. 260501. URL: https://link.aps.org/doi/10.1103/PhysRevLett.101.260501.

[76] Nathanan Tantivasadakarn, Ashvin Vishwanath, and Ruben Verresen. “Hierarchy of Topological Order From Finite-Depth Unitaries, Measurement, and Feedforward”. In: *PRX Quantum* 4.2 (2023), p. 020339. eprint: 2209.06202.

[77] Google Quantum AI. “Quantum Computer Datasheet”. In: *URL* (2021). URL: https://quantumai.google/hardware/datasheet/weber.pdf.

[78] A. M. Steane. “Error Correcting Codes in Quantum Theory”. In: *Physical Review Letters* 77.5 (1995), pp. 793–797.

[79] A. R. Calderbank et al. “Quantum Error Correction and Orthogonal Geometry”. In: *Physical Review Letters* 78.3 (1996), pp. 405–408. eprint: quant-ph/9605005.

[80] Daniel Gottesman. “Stabilizer Codes and Quantum Error Correction”. In: *arXiv* (1997). eprint: quant-ph/9705052.

[81] D W Kribs et al. “Operator quantum error correction”. In: *Quantum Information and Computation* 6.4&5 (2006), pp. 382–399.

[82] H. Bombin. “Topological subsystem codes”. In: *Physical Review A* 81.3 (2010), p. 032301. eprint: 0908.4246.

[83] Tyler D. Ellison et al. “Pauli Stabilizer Models of Twisted Quantum Doubles”. In: *PRX Quantum* 3.1 (2022), p. 010353. eprint: 2112.11394.

[84] Tyler D. Ellison et al. “Pauli topological subsystem codes from Abelian anyon theories”. In: *Quantum* 7 (2023), p. 1137. eprint: 2211.03798.

[85] Tyler Ellison and Meng Cheng. “Towards a classification of mixed-state topological orders in two dimensions”. In: *arXiv* (2024). eprint: 2405.02390.

[86] Zijian Wang, Zhengzhi Wu, and Zhong Wang. “Intrinsic Mixed-state Topological Order Without Quantum Memory”. In: *arXiv* (2023). eprint: 2307.13758.

[87] Ramanjit Sohal and Abhinav Prem. “A Noisy Approach to Intrinsically Mixed-State Topological Order”. In: *arXiv* (2024). eprint: 2403.13879.

[88] Yimu Bao et al. “Mixed-state topological order and the errorfield double formulation of decoherence-induced transitions”. In: *arXiv* (2023). eprint: 2301.05687.

[89] Daniel Jafferis et al. “Traversable wormhole dynamics on a quantum processor”. In: *Nature* 612.7938 (2022), pp. 51–55.

[90] Thomas Schuster et al. “Many-Body Quantum Teleportation via Operator Spreading in the Traversable Wormhole Protocol”. In: *Physical Review X* 12.3 (2022), p. 031013. eprint: 2102.00010.

[91] Michał Horodecki, Paweł Horodecki, and Ryszard Horodecki. “Inseparable Two Spin- $\frac{1}{2}$ Density Matrices Can Be Distilled to a Singlet Form”. In: *Phys. Rev. Lett.* 78 (4 Jan. 1997), pp. 574–577. URL: https://link.aps.org/doi/10.1103/PhysRevLett.78.574.

[92] Michał Horodecki and Paweł Horodecki. “Reduction criterion of separability and limits for a class of distillation protocols”. In: *Phys. Rev. A* 59 (6 June 1999), pp. 4206–4216. URL: https://link.aps.org/doi/10.1103/PhysRevA.59.4206.

[93] Curt von Keyserlingk, Frank Pollmann, and Tibor Rakovszky. “Operator backflow and the classical simulation of quantum transport”. In: *Physical Review B* 105.24 (2022), p. 245101. eprint: 2111.09904.

[94] Tibor Rakovszky, C. W. von Keyserlingk, and Frank Pollmann. “Dissipation-assisted operator evolution method for capturing hydrodynamic transport”. In: *Physical Review B* 105.7 (2022), p. 075131.

[95] Antonio Anna Mele. “Introduction to Haar Measure Tools in Quantum Information: A Beginner’s Tutorial”. In: *Quantum* 8 (2024), p. 1340. eprint: 2307.08956.

[96] Alexander M Dalzell, Nicholas Hunter-Jones, and Fernando G S L Brandão. “Random quantum circuits anti-concentrate in log depth”. In: *arXiv* (2020). eprint: 2011.12277.

[97] Thomas Schuster, Jonas Haferkamp, and Hsin-Yuan Huang. “Random unitaries in extremely low depth”. In: *arXiv* (2024). eprint: 2407.07754.

[98] Jan Benhelm et al. “Towards fault-tolerant quantum computing with trapped ions”. In: *Nature Physics* 4.6 (2008), pp. 463–466. eprint: 0803.2798.

[99] D. Nigg et al. “Quantum computations on a topologically encoded qubit”. In: *Science* 345.6194 (2014), pp. 302–305. eprint: 1403.5426.

[100] Jiehang Zhang et al. “Observation of a many-body dynamical phase transition with a 53-qubit quantum simulator”. In: *Nature* 551.7682 (2017), pp. 601–604.

[101] Nicolai Friis et al. “Observation of Entangled States of a Fully Controlled 20-Qubit System”. In: *Phys. Rev. X* 8 (2 Apr. 2018), p. 021012. URL: https://link.aps.org/doi/10.1103/PhysRevX.8.021012.

[102] R. Barends et al. “Superconducting quantum circuits at the surface code threshold for fault tolerance”. In: *Nature* 508.7497 (2014), pp. 500–503. eprint: 1402.4848.

[103] J. Kelly et al. “State preservation by repetitive error detection in a superconducting quantum circuit”. In: *Nature* 519.7541 (2015), pp. 66–69. eprint: 1411.7403.

[104] Nissim Ofek et al. “Extending the lifetime of a quantum bit with error correction in superconducting circuits”. In: *Nature* 536.7617 (2016), pp. 441–445.

[105] G Wendin. “Quantum information processing with superconducting circuits: a review”. In: *Reports on Progress in Physics* 80.10 (2017), p. 106001. eprint: 1610.02208.

[106] Hendrik Weimer et al. “A Rydberg quantum simulator”. In: *Nature Physics* 6.5 (2010), pp. 382–388.

[107] Julio T. Barreiro et al. “An open-system quantum simulator with trapped ions”. In: *Nature* 470.7335 (2011), pp. 486–491. eprint: 1104.1146.

[108] Daniel Barredo et al. “An atom-by-atom assembler of defect-free arbitrary two-dimensional atomic arrays”. In: *Science* 354.6315 (2016), pp. 1021–1023. URL: https://www.science.org/doi/abs/10.1126/science.aah3778.

[109] Manuel Endres et al. “Atom-by-atom assembly of defect-free one-dimensional cold atom arrays”. In: *Science* 354.6315 (2016), pp. 1024–1027. URL: https://www.science.org/doi/abs/10.1126/science.aah3752.

[110] Hannes Bernien et al. “Probing many-body dynamics on a 51-atom quantum simulator”. In: *Nature* 551.7682 (2017), pp. 579–584.

[111] Sepehr Ebadi et al. “Quantum phases of matter on a 256-atom programmable quantum simulator”. In: *Nature* 595.7866 (2021), pp. 227–232. eprint: 2012.12281.

[112] Pasquale Calabrese and John Cardy. “Entanglement entropy and quantum field theory”. In: *Journal of Statistical Mechanics: Theory and Experiment* 2004.06 (2004), P06002. eprint: hep-th/0405152.

[113] N. M. Linke et al. “Measuring the Rényi entropy of a two-site Fermi-Hubbard model on a trapped ion quantum computer”. In: *Physical Review A* 98.5 (2018), p. 052334. eprint: 1712.08581.

[114] Ryan Levy, Di Luo, and Bryan K. Clark. *Classical Shadows for Quantum Process Tomography on Near-term Quantum Computers*. 2021. arXiv: 2110.02965.

[115] Jonathan Kunjummen et al. "Shadow process tomography of quantum channels". In: *Physical Review A* 107.4 (2023), p. 042403. eprint: 2110.03629.

[116] *IBM Quantum*. https://quantum-computing.ibm.com/. 2021.

[117] *Qiskit textbook, Section 5.2*. https://qiskit.org/textbook/ch-quantum-hardware/measurement-error-mitigation.html.

[118] Senrui Chen et al. "Robust Shadow Estimation". In: *PRX Quantum* 2 (3 Sept. 2021), p. 030348. URL: https://link.aps.org/doi/10.1103/PRXQuantum.2.030348.

[119] G. Vidal and R. F. Werner. "Computable measure of entanglement". In: *Phys. Rev. A* 65 (3 Feb. 2002), p. 032314. URL: https://link.aps.org/doi/10.1103/PhysRevA.65.032314.

[120] Andreas Elben et al. "Mixed-State Entanglement from Local Randomized Measurements". In: *Phys. Rev. Lett.* 125 (20 Nov. 2020), p. 200501. URL: https://link.aps.org/doi/10.1103/PhysRevLett.125.200501.

[121] Asher Peres. "Separability Criterion for Density Matrices". In: *Phys. Rev. Lett.* 77 (8 Aug. 1996), pp. 1413–1415. URL: https://link.aps.org/doi/10.1103/PhysRevLett.77.1413.

[122] Benjamin Schumacher and Michael D. Westmoreland. "Sending classical information via noisy quantum channels". In: *Phys. Rev. A* 56 (1 July 1997), pp. 131–138. URL: https://link.aps.org/doi/10.1103/PhysRevA.56.131.

[123] A.S. Holevo. "The capacity of the quantum channel with general signal states". In: *IEEE Transactions on Information Theory* 44.1 (1998), pp. 269–273.

[124] E. Rosenberg et al. "Dynamics of magnetization at infinite temperature in a Heisenberg spin chain". In: *Science* 384.6691 (2024), pp. 48–53. eprint: 2306.09333.

[125] Bingtian Ye et al. "Universal Kardar-Parisi-Zhang Dynamics in Integrable Quantum Systems". In: *Physical Review Letters* 129.23 (2022), p. 230602. eprint: 2205.02853.

[126] Nathan Keenan et al. "Evidence of Kardar-Parisi-Zhang scaling on a digital quantum simulator". In: *arXiv* (2022). eprint: 2208.12243.

[127] Johannes Hauschild and Frank Pollmann. "Efficient numerical simulations with Tensor Networks: Tensor Network Python (TeNPy)". In: *SciPost Physics Lecture Notes* (2018), p. 005. eprint: 1805.00055.

[128] Shenglong Xu and Brian Swingle. "Accessing scrambling using matrix product operators". In: *Nature Physics* 16.2 (2020), pp. 199–204. eprint: 1802.00801.

[129] Elliott H. Lieb and Derek W. Robinson. "The finite group velocity of quantum spin systems". In: *Communications in Mathematical Physics* 28.3 (1972), pp. 251–257.

[130] C Karrasch, J H Bardarson, and J E Moore. "Reducing the numerical effort of finite-temperature density matrix renormalization group calculations". In: *New Journal of Physics* 15.8 (2013), p. 083031. eprint: 1303.3942.

[131] Maurizio Fagotti and Pasquale Calabrese. "Entanglement entropy of two disjoint blocks in XY chains". In: *Journal of Statistical Mechanics: Theory and Experiment* 2010.04 (2010), P04016. eprint: 1003.1110.

[132] Yu-Jie Liu et al. "Methods for Simulating String-Net States and Anyons on a Digital Quantum Computer". In: *PRX Quantum* 3 (4 Nov. 2022), p. 040315. URL: https://link.aps.org/doi/10.1103/PRXQuantum.3.040315.

[133] G K Brennen, M Aguado, and J I Cirac. "Simulations of quantum double models". In: *New Journal of Physics* 11.5 (May 2009), p. 053009. URL: http://dx.doi.org/10.1088/1367-2630/11/5/053009.

[134] Shawn X Cui. "Topological Quantum Computation". In: *Lecture Notes* (2018). URL: https://www.math.purdue.edu/~cui177/Lecture_Combined.pdf.

[135] Shawn X. Cui, Seung-Moon Hong, and Zhenghan Wang. "Universal quantum computation with weakly integral anyons". In: *Quantum Information Processing* 14.8 (May 2015), pp. 2687–2727. URL: https://doi.org/10.1007%2Fs11128-015-1016-y.

[136] Michaël Mignard and Peter Schauenburg. "Modular categories are not determined by their modular data". In: *Letters in Mathematical Physics* 111.3 (Apr. 2021). URL: http://dx.doi.org/10.1007/s11005-021-01395-0.

[137] Sergey Bravyi et al. *Adaptive constant-depth circuits for manipulating non-abelian anyons*. 2022. arXiv: 2205.01933.

[138] Google Quantum AI. "Quantum Computer Datasheet". In: *URL* (May 2021). URL: https://quantumai.google/hardware/datasheet/weber.pdf.

[139] Shibo Xu et al. "Digital simulation of projective non-Abelian anyons with 68 superconducting qubits". In: *Chinese Physics Letters* (2023). URL: http://iopscience.iop.org/article/10.1088/0256-307X/40/6/060301.

[140] Guo-Yi Zhu, Nathanan Tantivasadakarn, and Simon Trebst. "Structured volume-law entanglement in an interacting, monitored Majorana spin liquid". In: *arXiv* (2023). eprint: 2303.17627.

[141] Adithya Sriram et al. "Topology, criticality, and dynamically generated qubits in a stochastic measurement-only Kitaev model". In: *Physical Review B* 108.9 (2023), p. 094304. eprint: 2207.07096.

[142] Ali Lavasani, Zhu-Xi Luo, and Sagar Vijay. "Monitored quantum dynamics and the Kitaev spin liquid". In: *Physical Review B* 108.11 (2023), p. 115135.

[143] Amir-Reza Negari, Subhayan Sahu, and Timothy H. Hsieh. "Measurement-induced phase transitions in the toric code". In: *Physical Review B* 109.12 (2024), p. 125148. eprint: 2307.02292.

[144] Alexei Kitaev and John Preskill. "Topological Entanglement Entropy". In: *Physical Review Letters* 96.11 (2006), p. 110404. eprint: hep-th/0510092.

[145] Yaodong Li, Xiao Chen, and Matthew P. A. Fisher. "Quantum Zeno effect and the many-body entanglement transition". In: *Physical Review B* 98.20 (2018), p. 205136. eprint: 1808.06134.

[146] Ali Lavasani, Yahya Alavirad, and Maissam Barkeshli. "Topological Order and Criticality in (2+1)D Monitored Random Quantum Circuits". In: *Physical Review Letters* 127.23 (2021), p. 235701. eprint: 2011.06595.

[147] Benedikt Placke and S A Parameswaran. "Slow measurement-only dynamics of entanglement in Pauli subsystem codes". In: *arXiv* (2024). eprint: 2405.14927.

[148] Brian Swingle. "Conformal field theory approach to Fermi liquids and other highly entangled states". In: *Physical Review B* 86.3 (2012), p. 035116. eprint: 1002.4635.

[149] S F Edwards and P W Anderson. "Theory of spin glasses. II". In: *Journal of Physics F: Metal Physics* 6.10 (2001), p. 1927.

[150] Giorgio Parisi. "Nobel Lecture: Multiple equilibria*". In: *Reviews of Modern Physics* 95.3 (2023), p. 030501.

[151] Eugene M. Luks, Ferenc Rákóczi, and Charles R.B. Wright. "Some Algorithms for Nilpotent Permutation Groups". In: *Journal of Symbolic Computation* 23.4 (1997), pp. 335–354. URL: https://www.sciencedirect.com/science/article/pii/S0747717196900929.

[152] Beni Yoshida and Norman Y. Yao. "Disentangling Scrambling and Decoherence via Quantum Teleportation". In: *Phys. Rev. X* 9 (1 Jan. 2019), p. 011006. URL: https://link.aps.org/doi/10.1103/PhysRevX.9.011006.

[153] Yong-Liang Zhang, Yichen Huang, and Xie Chen. "Information scrambling in chaotic systems with dissipation". In: *Phys. Rev. B* 99 (1 Jan. 2019), p. 014303. URL: https://link.aps.org/doi/10.1103/PhysRevB.99.014303.

[154] Beni Yoshida and Alexei Kitaev. *Efficient decoding for the Hayden-Preskill protocol*. 2017. arXiv: 1710.03363.

[155] Bruno Bertini, Pavel Kos, and Tomaz Prosen. "Operator Entanglement in Local Quantum Circuits I: Chaotic Dual-Unitary Circuits". In: *SciPost Physics* 8.4 (2020), p. 067. eprint: 1909.07407.

[156] Bruno Bertini, Pavel Kos, and Tomaz Prosen. "Operator Entanglement in Local Quantum Circuits II: Solitons in Chains of Qubits". In: *SciPost Physics* 8.4 (2020), p. 068. eprint: 1909.07410.

[157] Michael J. Gullans and David A. Huse. "Dynamical Purification Phase Transition Induced by Quantum Measurements". In: *Phys. Rev. X* 10 (4 Oct. 2020), p. 041020. URL: https://link.aps.org/doi/10.1103/PhysRevX.10.041020.

[158] Zongping Gong, Lorenzo Piroli, and J. Ignacio Cirac. "Topological Lower Bound on Quantum Chaos by Entanglement Growth". In: *Phys. Rev. Lett.* 126 (16 Apr. 2021), p. 160601. URL: https://link.aps.org/doi/10.1103/PhysRevLett.126.160601.